



Università di Pisa

Facoltà di Ingegneria

Corso di laurea Magistrale in Ingegneria Aerospaziale

Robotic Hooking System for Floating Lander

Relatore:

Ing. Mario Rosario Chiarelli

Candidati:

Lorenzo Bizzi

Giacomo Dinuzzi

Anno accademico 2014/2015

Abstract

Exploration of planets' satellites and other celestial bodies such as comets and asteroids is lately becoming of interest either for scientific purpose or for commercial exploitation. This thesis work propose a possible robotic hooking system in order to stabilize a floating lander which should make some samples acquisition on outer planet's satellite.

Analysis begin from some already existing mission proposals which involve exploration of Titan, Saturn's largest moon. Since Titan surface is widely covered by liquid methane lakes, all mission proposals include floating lander which should be capable of travelling on lakes' surface. Because of scientific interest either in liquid samples analysis or solid shoreline analysis, one can think about a possible hooking system to be deployed close to shoreline rocks, in order to make possible solid samples acquisition from cost line. Then Titan environment has been analysed, taking into account wind and waves to design a proper hooking system. At the beginning two possible hooking mechanism candidates have been considered, harpoon mechanism and robotic arms, identifying pros and cons for both configurations. Various considerations have led to the choice of robotic arms system for hooking realization. Once more suited hooking system has been chosen for this purpose, some computational analysis has been carried out in order to find a proper arm cross section capable of resisting under loading conditions. Hooking problem has been analysed from a displacement point of view, thinking of not being capable of lowering vertical displacement imposed by waves motion. A simplified two dimensional model has been used at first and once cross section candidates have been identified, two dimensional results have been validated with a three dimensional model. Later on, hooking mechanism choice have been taken into account more in detail. Even for hooking mechanism itself, two different possible hooking mechanisms have been considered first, suction cups-based mechanism and microspines-based one. From dimension and adaptability considerations microspines-based mechanism has been chosen. Then, hooking mechanism dimension and mechanical parts design have been produced. Effects of arms' motion on lander stability have been analyse too, leading to proposed deployment pattern which maintains lander within acceptable values of tilting angles. At the end of thesis work hooking mechanism model have been validated with fatigue analysis in order to ensure proper functioning under repeated cycles of loading.

Finally, some considerations about future work to be done have been proposed, in order to improve current work and to further develop presented preliminary analysis. A section about similar robotic mechanism has been added at the end of the thesis for sake of completeness and to show other possible applications to microspines technology.

Index

- 1 Introduction..... 1
 - 1.1 Titan brief description 1
 - 1.2 Previous missions 2
 - 1.3 Future missions..... 2
 - 1.4 Work guideline..... 2
 - 1.5 Lander different architectures..... 3
 - 1.6 Operating environment 4
- 2 Specification 7
 - 2.1 Lander generalities 7
 - 2.2 Performance requirements 7
 - 2.3 Condition to be satisfied..... 8
- 3 Load analysis..... 10
 - 3.1 Hooking systems comparison 10
 - 3.2 Model overview 11
 - 3.3 2d model..... 11
 - 3.3.1 In plane arm model 12
 - 3.3.2 Out of plane arm model..... 17
 - 3.3.3 In plane arm model cross sections 18
 - 3.3.4 Transversal hooking 22
 - 3.4 3d model..... 23
 - 3.4.1 2d/3d geometrical comparison 24
 - 3.4.2 2d/3d section comparison 26
 - 3.5 Cross section choice 29
- 4 Robotics 31
 - 4.1 Robotics generalities 31
 - 4.2 Simulation 34
 - 4.2.1 Kinematic 34
 - 4.2.2 Dynamic 37
 - 4.3 Servo motors 40

4.4 Joint angle limitations.....	41
4.5 Servo motors locking system.....	43
4.5.1 Arms joints locking system	43
5 Hooking mechanism.....	45
5.1 Solution A.....	45
5.2 Solution B.....	54
5.2.1 Hooking configuration	58
5.2.2 Results discussion	61
5.3 Solutions comparison	62
5.4 Actuation mechanism architecture	63
5.5 Final configuration.....	65
5.6 Actuation mechanism loads	66
5.7 Manufacturing generalities	69
6 Fatigue verification.....	71
6.1 Model description.....	71
6.2 Critical components analysis	72
6.2.1 Interface.....	72
6.2.2 Toe stick	74
6.3 Conclusions.....	76
7 Lander stability.....	77
7.1 Buoyancy.....	77
7.2 Metacentre and centre of buoyancy.....	78
7.3 Barycentre	78
7.4 Barycentre displacement.....	80
7.4.1 Horizontal displacement.....	82
7.4.2 Vertical displacement	82
7.4.3 Further comments	83
7.5 Conclusions.....	84
8 Launch configuration.....	85
8.1 Arms folded configurations	85
8.2 Vibration preliminary analysis	87
9 Microspine technology review	89

9.1 State of the art.....	89
9.2 Possible future employment for space application.....	90
10 General conclusions	93
10.1 Work summary	93
10.2 Future improvement	93

1 Introduction

The purpose of this thesis work is to develop a hooking system in order to collect samples from Saturn's moon Titan shoreline. We first give a general introduction of the environment of Saturn's moon, revising previous missions and its goals. We then take a look at future mission proposal of which we will make use as starting point for our work.

1.1 Titan brief description

Titan is the largest satellite of Saturn with equatorial radius of 2575 km [2] and results to be the only moon in the Solar System with a significant atmosphere [1,2]. Titan atmospheric layer is made mostly of nitrogen (95%), the remaining 5% is made of methane (3%), hydrogen, little vapor water and other hydrocarbons [1,2]. Radar images obtained by Cassini space probe during its flybys with Titan appear to show lakes of liquid hydrocarbon (such as methane and ethane) in Titan's northern latitudes [1,2]. The chemical composition of the lakes of Titan is still not well determined [1]. The temperature at Titan's surface is about -180 degrees Celsius [2]; at this temperature, water ice is hard as rock and its physical properties resemble more ones of a rock like granite instead of ones of water ice we are familiar to on Earth [8]. We will see in the course of the report that physical properties of water ice at -180 °C will be crucial to discriminate between different possible hooking systems. Titan surface gravity acceleration is $1,35 \text{ m/s}^2$ [2]. Surface pressure results to be higher than Earth surface pressure of about 60 per cent [2], we will assume for calculations a surface pressure of 1,6 bar (0,16 Mpa). Fig. 1 shows temperature and pressure profiles with respect to altitude from Titan surface [10].

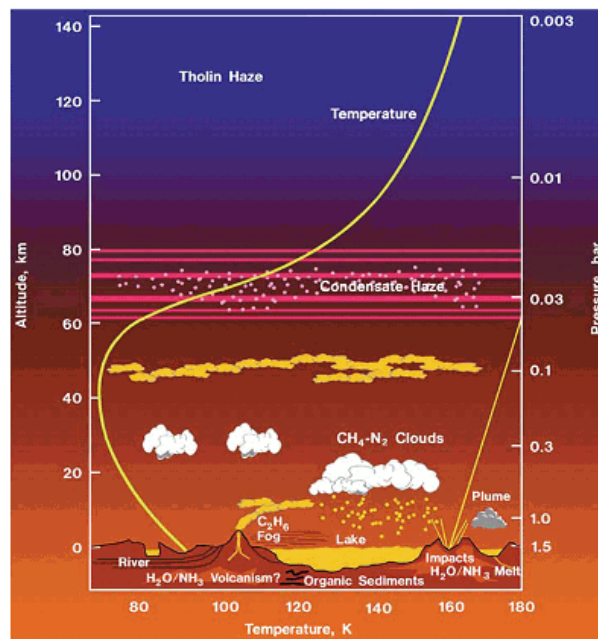


Fig. 1. Temperature profile with respect to altitude [10].

1.2 Previous missions

Pioneer 11 in 1979 was the first space probe which made close images of Saturn and Titan [3]; just a year later probe Voyager 1 made a flyby with Saturn's moon in order to obtain better quality images [4], since flyby with Titan was not scheduled at launch time, Voyager 1 was not equipped with dedicated cameras capable of penetrate Titan atmosphere and some indications about Titan's surface were obtained only after some manipulation technique [4]. First (and only) dedicated mission to Titan was Cassini-Huygens mission launched in 1997 and arrived at Titan in 2004 [5], it involved a space probe (Cassini) and a lander probe (Huygens) which landed on Titan solid surface (although it was capable of floating for a short period of time as well) and returned some surface images and atmospheric data (such as composition, temperature and wind velocity) [5].

1.3 Future missions

In the last 10 years some missions towards Saturn's moon Titan have been proposed and a major number of these [1,6] include a lander probe capable to float over Titan seas which will make measurement and take samples in order to get a better knowledge of this environment that could be similar to the one of a young Earth [2,7]. Up to now none of this mission proposal has been approved or brought to realization.

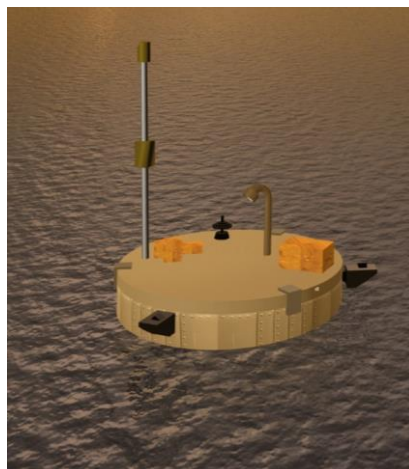


Fig. 2. Artistic representation of Titan floating lander [].

1.4 Work guideline

The mission we will make use as starting point to develop our hooking system will be Titan Saturn System Mission (TSSM) [6]. This mission includes an orbiter, a balloon which will be released from main orbiter in order to analyze wind pattern and atmospheric composition and a floating lander released as well from main orbiter to perform a splash down on Kraken mare in the northern hemisphere and from there sailing towards shoreline collecting data about liquid methane lake and possibly shoreline's rocks [6].

Since TSSM is a mission proposal, it only gives general guidelines regarding subsystem, mass, sensors and so on; we will make use of some existing guidelines as well as producing new ones where necessary.

1.5 Lander different architectures

As we said in previous sections, Titan surface temperature has been measured [2] to be around -180°. Liquid methane can exist at this extremely cold temperature, indeed Titan landscape includes numerous methane lakes [7,12]. Due to this peculiar environment, as we said before, almost all mission proposals include floating lander. Even if target lakes are different for different missions, lander concepts are based on the same idea, the lander must be able to reach lake’s shores and analyze liquid methane and possibly shoreline’s rocks. To make this possible two main working philosophies are considered, one is based on propulsion mechanism [1] that will make possible to manoeuvre floating lander while the other one is based on the concept of exploiting liquid methane drift induced by atmospheric wind circulation to reach the shore [6,11]. Clearly two concepts are really different and include different level of technology, cost, reliability and complexity to be realized.

Lander capable of autonomous motion, thus which include propulsion mechanism, is surely more complicated and then costly. Propulsion mechanism needs power to work, either batteries or propellant, and adds mass and complexity to overall lander structure, since there is the need to allocate propulsion mechanism and related subsystems. On the other hand, autonomous motion capability ensure much higher safety approach to shorelines, since it would be possible to avoid collisions with rocks and incorrect misalignment of the hooking system towards shoreline’s rocks. Moreover, during cruise phase from splash down site to shoreline it is still possible to exploit liquid methane drift as well as for not propelled lander.

Not propelled lander is much simpler and less costly compared to the propelled solution. The main advantages of this architecture is to allow to save mass and probably reliability, since the simpler the architecture the less the chance of failure of some components. On the contrary, this architecture is subjected to random and unpredictable variation either in wind or current patterns and does not allow to face unexpected events during cruise phase and shoreline approach.

Table 1 summaries pros and cons for two architectures.

Lander architecture	Pros	Cons
Propelled	Maneuverability Versatility	Mass Complexity
Not propelled	Reliability Mass	Maneuverability Versatility

Table 1. Pros and cons for propelled/not propelled lander architecture.

It is easy to realize that even if the propulsion system will not be used for cruise phase, from splash down site towards shoreline, in order to ensure a proper lander orientation during shoreline approach a propulsion system is mandatory. Propulsion system can be either designed to guarantee both cruise phase and approach phase or approach phase only. The first architecture is surely more robust, but the second one is simpler and cheaper.

Since cruise phase is not an issue of our work, we solely consider the lander will be capable of perform alignment maneuvers during costal approach. Fig.3 shows some possible propulsion architectures [1].

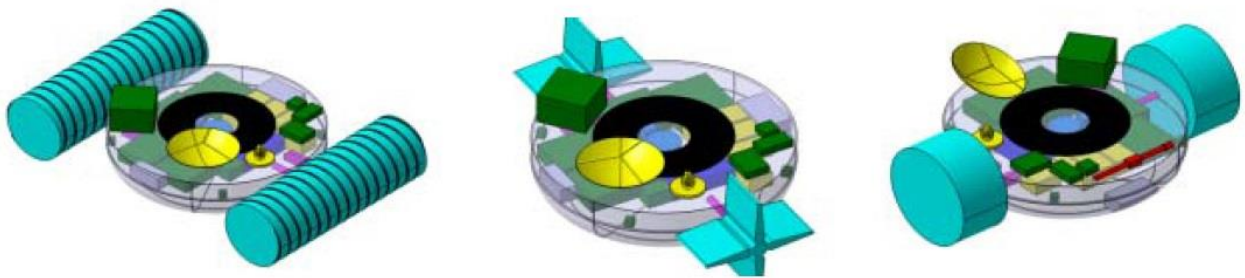


Fig. 3. Possible lander propulsion architecture [10].

1.6 Operating environment

As said in the previous section, target landing spot is located on liquid methane lake's surface. The two largest Titan lakes have been considered for splash down, respectively Kraken mare and Ligeia mare [12]. Both are located in the northern hemisphere at high latitude [13]. While Ligeia mare has been completely mapped by the Cassini radar, Kraken mare has not. Since Titan northern region is characterized by the presence of numerous lakes is possible that, for unexpected events, splash down site could be changed during the course of the mission.

As for terrestrial lakes and seas, interactions between lake's liquid phase and atmosphere occur on Titan too, this interaction results in different kind of waves traveling through liquid surface. First clue of the presence of waves on lakes and seas surface on Titan is the presence of some geological features that can be related to waves mechanisms, such as costal erosion. Since is quite reasonable thinking of waves' presence on Titan surface, wave generation mechanism on Titan has been studied in analogy with waves generation on Earth [10].

Waves generation mechanism we take into consideration is based on interaction between wind and liquid surface. So, for waves to appear one key parameter to be considered is viscosity of the liquid which exchange energy with wind [10]. Intuitively, the less the viscosity the less the wind speed needed to initiate wave formation. Thus, having liquid methane lower viscosity value than see water on Earth, waves on Titan exist at less wind speed

compared to ones on Earth [10]. Considering Sverdrup–Munk model [10] to compute wave height, we can write,

$$H = 0,2 \frac{U^2}{g}$$

Where:

- H , is the wave height,
- U^2 , is wind speed,
- g , is gravity acceleration.

Detailed studies have been shown that for mission duration, Titan maximum seasonal wind is of $U = 1 \text{ m/s}$ [10]; so for $g = 1,35 \text{ m/s}^2$ that yield a wave height of $H = 0,15 \text{ m}$.

For wave length, considering Sverdrup-Munk model that results to be quite conservative [10], since predict steeper waves than the actual ones, we can write,

$$\lambda = 7H$$

That, for $H = 0,15 \text{ m}$ as determined before, we obtain wave length $\lambda = 1,05 \text{ m}$.

We can further write [10],

$$c = \sqrt{\frac{\lambda g}{2\pi}}$$

Where:

- c , is wave speed,
- λ , is wave length,
- g , is gravity acceleration

That for previous derived results, yields wave speed $c = 0,5 \text{ m/s}$.

Finally we are able to calculate wave period from well-known relation,

$$c = \frac{\lambda}{T}$$

That yields a wave period $T = 2 \text{ s}$.

As said before, Sverdrup-Munk model is quite conservative, because considers steeper waves than actual developed waves [10].

Finally, maximum wave height considered during this work is taken according to model used

in [10], which consider waves encountered during mission period to have a maximum height of $H = 0,2 \text{ m}$, period $T = 4 \text{ s}$ and wave length $\lambda = 4,5 \text{ m}$ resulting indeed less steep than ones obtained with Sverdrup-Munk model. Also, maximum wave height obtained with Sverdrup-Munk model has been augmented by 30%.

References

- [1] URDAMPILLETA, I., et al. TALISE: Titan Lake In-situ Sampling Propelled Explorer. In: *Proceedings of the European Planetary Science Congress*. 2012. p. 64.
- [2] <http://solarsystem.nasa.gov/planets/titan/indepth>. Last access on November 2015.
- [3] <http://www.nasa.gov/centers/ames/missions/archive/pioneer.html>. Last access on November 2015.
- [4] RICHARDSON, James; LORENZ, Ralph D.; MCEWEN, Alfred. Titan's surface and rotation: new results from Voyager 1 images. *Icarus*, 2004, 170.1: 113-124.
- [5] MATSON, Dennis L.; SPILKER, Linda J.; LEBRETON, Jean-Pierre. The Cassini/Huygens mission to the Saturnian system. In: *The Cassini-Huygens Mission*. Springer Netherlands, 2003. p. 1-58.
- [6] LEMENTS, NITU. ESA Contribution to the Titan Saturn System Mission. 2009.
- [7] <http://www.space.com/7103-titan-world-earth.html>. Last access on November 2015.
- [8] <http://www.astrobio.net/topic/solar-system/saturn/titan/titans-rocks-of-ice/>. Last access on November 2015.
- [9] <http://attic.gsfc.nasa.gov/huygensgcms/Titan.htm>. Last access on November 2015.
- [10] LORENZ, Ralph D.; HAYES, Alexander G. The growth of wind-waves in Titan's hydrocarbon seas. *Icarus*, 2012, 219.1: 468-475.
- [11] STOFAN, Ellen, et al. TiME—The Titan Mare Explorer. In: *IEEE Aerospace Conference, Big Sky, MT*. 2013. p. 2434.
- [12] LORENZ, Ralph D.; NEWMAN, Claire; LUNINE, Jonathan I. Threshold of wave generation on Titan's lakes and seas: Effect of viscosity and implications for Cassini observations. *Icarus*, 2010, 207.2: 932-937.
- [13] STOFAN, E. R., et al. Shorelines of Ligeia Mare, Titan. In: *Lunar and Planetary Science Conference*. 2012. p. 1556.

2 Specification

In this section specification of lander and mission goals are presented. Hooking system to be developed is based on specification instructions.

2.1 Lander generalities

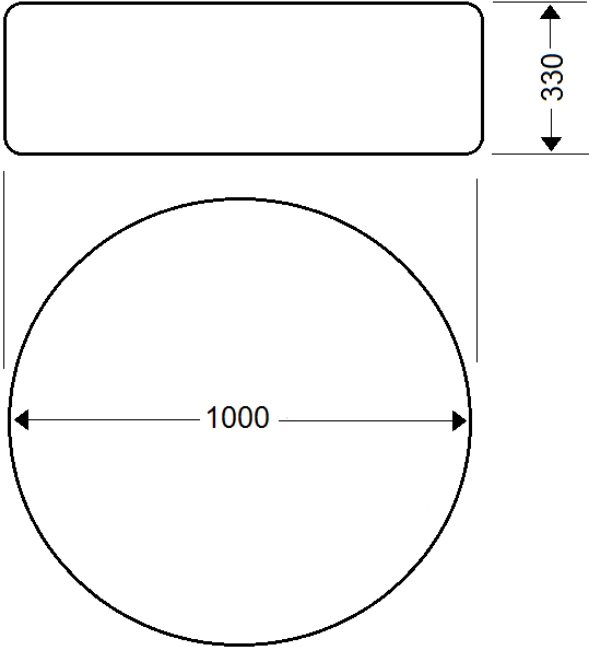
<i>Propulsion system goals</i>	Capable of perform small attitude correction manoeuvres in order to obtain proper lander orientation for hooking
<i>Lander Mass</i>	70 Kg
<i>Lander dimensions</i>	 <p>The diagram illustrates the lander's dimensions. It features a circular base with a diameter of 1000 units, indicated by a horizontal double-headed arrow. Above the circle is a rounded rectangular section with a height of 330 units, indicated by a vertical double-headed arrow on the right side.</p>

Table 2. Lander generalities.

2.2 Performance requirements

Hooking system must be developed in order to meet following requirements:

- Ensuring connection with irregular rocky surface.
- Ensuring lander stabilization during hooking in order to acquire samples from shoreline rocks.
- Capability of facing shoreline unevenness.

2.3 Condition to be satisfied

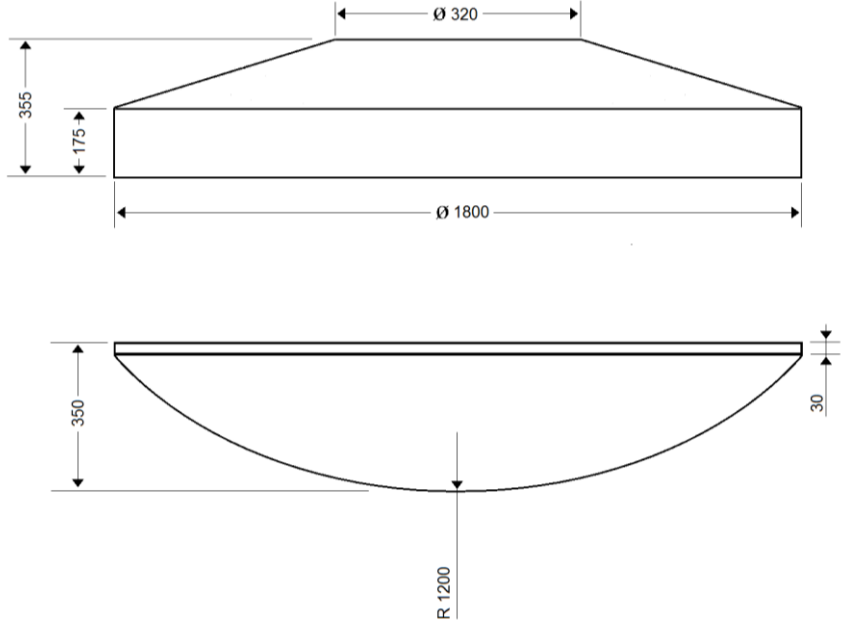

<p>Thermal shield dimensions</p>	
<p>Maximum hooking system allowable mass</p>	<p>10 kg</p>
<p>Lander sensors and instrumentations</p>	<p>Visual sensor for shoreline hooking spots identification. Autonomous hooking mechanism. Position, velocity and acceleration sensors. Inertial platform for attitude determination.</p>
<p>Operational time</p>	<p>2 hours</p>
<p>Shoreline characteristics</p>	<p>Rocky shoreline. Granite-like expected rocks [2]</p> 
<p>Maximum expected wind velocity</p>	<p>1 m/s</p>
<p>Observed waves amplitude</p>	<p>1,25 cm</p>
<p>Surface temperature</p>	<p>-180 °C</p>
<p>Atmospheric pressure at surface</p>	<p>152000 Pa</p>
<p>Design lives</p>	<p>3</p>

Table 3. Summary of hooking mechanism performance requirement and limitations.

References

[1] LEMENTS, NITU. ESA Contribution to the Titan Saturn System Mission. 2009.

[2] <http://www.astrobio.net/topic/solar-system/saturn/titan/titans-rocks-of-ice/>. Last access on November 2015.

3 Load analysis

In following section we will make a comparison between two different hooking architectures and we will choose one of these two. We will show our preliminary 2d analysis that will lead us to considerations about sections and materials to be used. At the end of the section we will discuss results and chose the best option.

3.1 Hooking systems comparison

In order to achieve lander stabilization close to liquid methane lake's shoreline, we selected two different possible solutions. First solution involves one or more harpoons to be fired in proximity of the coastline that will penetrate inside shore solid rock and then ensure the lander not to move away from working position. Second solution involves one or more robotic arms to be unfolded close to shoreline that someway grab solid rock and stabilize the lander in order to make samples acquisition. Two different architectures both present pros and cons that are summarized in Table 4.

For harpoon system pros can be evaluated as system simplicity (less moving parts) and lighter weight with respect to robotic arm. Cons are the need of a device that dissipate or balance recoil force generated from firing. Heritage from Rosetta mission has been considered as example of harpoon system [1].

For robotic arm pros are represented by large heritage from space missions [2,3] for possible materials and motor actuators and thus robust architecture. Cons have been evaluated as complexity of arm system and hooking mechanism that at this point of the analysis is still to be determined. Also higher weight has to be considered for robotic arm.

Hooking system	Pros	Cons
Harpoon	Weight Simplicity	Recoil force dissipation/balance mechanism needed
Robotic arm	Heritage Robust	Weight Hooking mechanism

Table 4. Pros and cons for harpoon/robotic arm hooking architecture.

Since mechanism needed to contrast recoil force is unfeasible with dissipation mechanism, a chemical thrust would be necessary. Chemical thrust would have to be fired simultaneously with harpoon in order to counteract the recoil force generated from harpoon shooting. This would add weight and complexity to overall architecture. Thus, robotic arm is the chosen hooking architecture. For hooking mechanism itself, mounted at the end of robotic arm, see Section 5.

3.2 Model overview

For our analysis we will consider floating lander close to lake's shore, moving with surrounding environment. Thus, in our analysis the lander follows liquid methane lake motion. For a floating object far from coastline it is possible to consider only vertical displacement, since horizontal ones result to be much smaller [4]. Lander actual environment not resemble open seas case and also waves reflected from the shore are present [4]. In our analysis we only consider regular waves and not reflected ones, as it would require computational models beyond the scope of this work. Results we obtain can be then improved in future works including in the subsequent analysis also reflected waves. In our analysis we do not directly consider reflected waves induced displacements, but we take into account their effects including safety factors to regular waves displacements and making conservative assumptions on posed problem.

As said, regular waves motion induces vertical displacement of fluid particles much higher than its horizontal displacement. Our first conservative assumption is to consider that this motion results in lander vertical displacement equal to liquid methane wave height apart from wave height and thus wave energy. Furthermore, we consider that vertical motion cannot be reduced from hooking system, so also when the lander will be physically connected to the shore we consider that its vertical displacement remains the one of not-connected conditions. Regarding waves height values, we consider for our calculations a maximum reachable height of $0,2\text{ m}$, which is the predicted maximum height for Titan conditions during mission execution, but still a safety factor of about 10 has been considered with respect to actual observed waves on Titan lakes surface [5].

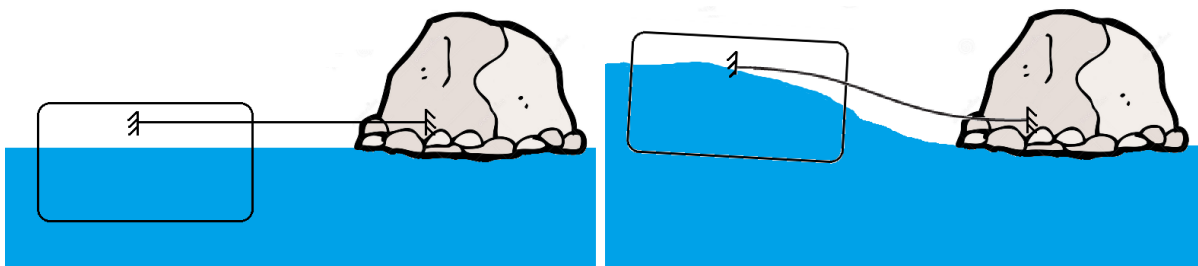


Fig. 4. Schematic representation of lander working environment.

3.3 2d model

In first approximation, we will consider our problem as a two dimensional problem for sake of simplicity.

3.3.1 In plane arm model

Model set up

Two different models are considered in the following section, comparing results validity, at the end of the section, we will choose one of them for the rest of the analysis.

First model involves a straight beam of $1,5\text{ m}$ of length, free at one end and fixed at the other end. A vertical displacement of $0,2\text{ m}$ has been applied at free end of the beam, representing wave imposed displacement. Fixed support represents interaction between robotic arm and shoreline rocks and even if actual support would not be strictly fixed, it is our aim to make actual support as close as possible to fixed one behavior. It has been applied the maximum possible displacement because, clearly, in all other situation, when the displacement is below maximum value, the problem results to be better from every points of view, rotation, stress, strain and support reactions.

In second model we take into account two beam, of different sections and material in order to make one much rigid than the other. The more rigid one, of length of $0,5\text{ m}$, represents the lander, while the more flexible one, of length of $1,5\text{ m}$ as before, represents the arm. We consider arm connected to the lander at half the hole lander length (1 m). Beam length represents a compromise between beam rigidity and dimensions. Shorter beam leads to higher fixed support reaction, so a longer beam is preferable. Of course, beam length cannot be extended beyond certain value for dimensions consideration and barycenter displacement (for barycenter analysis see Section 7). Vertical displacement of $0,2\text{ m}$ is applied to the hole lander. As before, considerations regarding maximum displacement and interactions between arm and rocks, remain the same.

Since $0,2\text{ m}$ vertical displacement over $1,5\text{ m}$ beam length cannot be considered small displacement, for our analysis has been impossible to use analytical model such as elastic line method, because of large displacement problem non-linearity. We then make use of computational program, Ansys APDL® and Ansys Workbench® in order to obtain valuable results.

We start considering a ring sections, of $1,5\text{ cm}$ of external radius and 1 mm of thickness for arm and circle sections of 2 m diameter for the lander. Lander cross section has clearly no physical meaning, but it has been chosen in order to make lander rigidity not comparable to the one of robotic arm. Applied materials are Al 720-T6 with ultimate strength of $S_u = 500\text{ Mpa}$ and yield strength of $S_y = 485\text{ Mpa}$ for arm and Ti 6Al-4V with ultimate strength of $S_u = 1100\text{ Mpa}$ and yield strength of $S_y = 950\text{ Mpa}$ [6].

Analysis statement produced with Ansys APDL® are shown below. BEAM188 element has been used for analysis.

Fig. 5 shows arm ring cross section used for preliminary calculation.

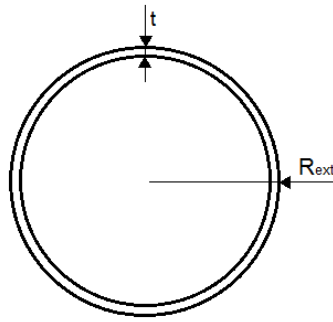


Fig. 5 Preliminary arm cross section, $R_{ext} = 1,5\text{ cm}$, $t = 1\text{ mm}$.

Fig. 6 and Fig. 7 show different models set up. We can see that fixed support condition at one end of the beam remains for both models, but vertical displacement conditions at the other end of the beam are different. In Fig. 6 vertical displacement is applied to free end point, while in Fig. 7 vertical displacement is applied to the hole line representing the lander.

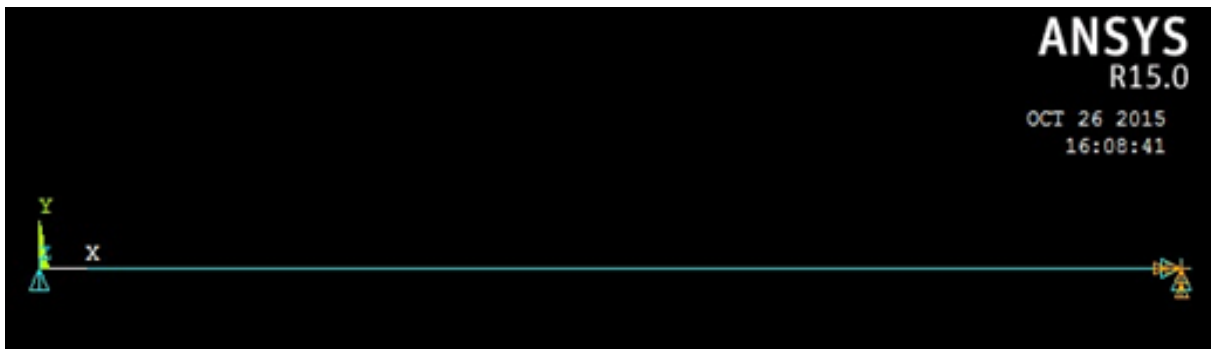


Fig. 6. Arm only, model set up

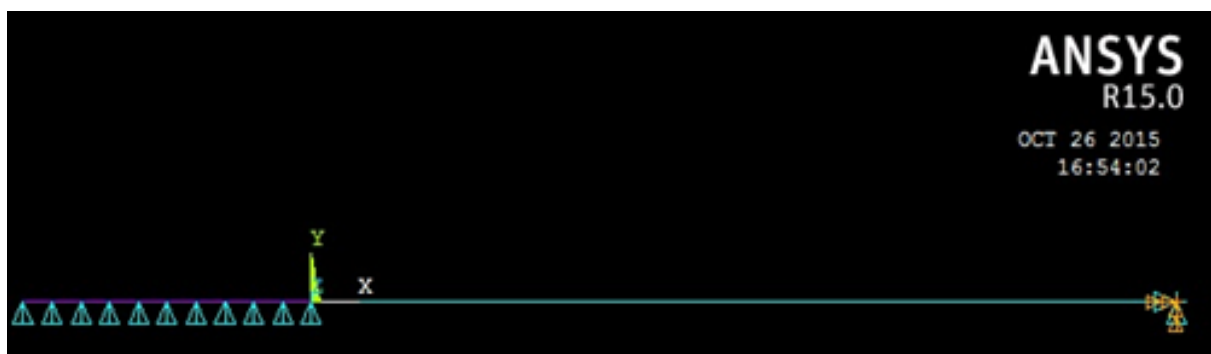


Fig. 7 Arm and lander, model set up

Results

z rotation

Fig. 8 and Fig. 9 shows results of rotation about z axis for the two different models.

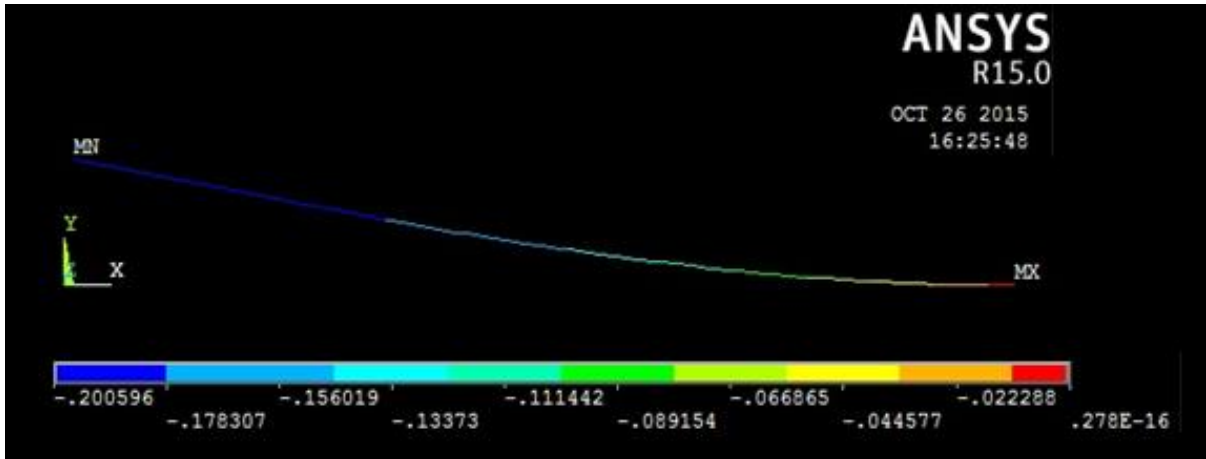


Fig. 8. Arm only, rotation about z (rad)

From Fig. 8, we see that the free end of the beam rotate of about $\alpha = 11,5 \text{ deg}$. Since, this model does not comprehend lander behavior, for this model the hole lander rotates of α about z axis. This is clearly an overestimation, because the lander is much more rigid than robotic arm and then free end beam rotation yielded in this model does not represent the actual lander rotation when the lander itself lies on the top of the wave.

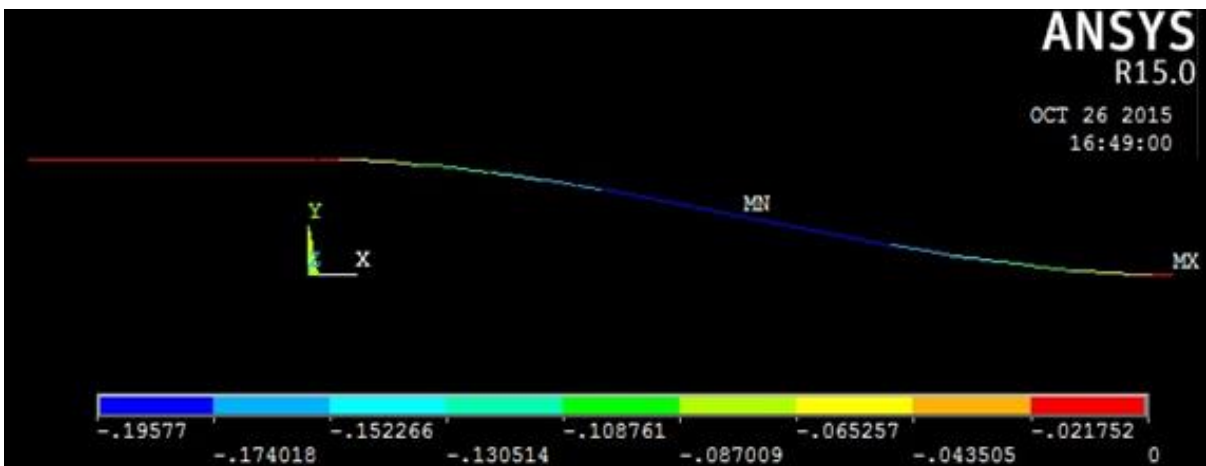


Fig. 9. Arm and lander, rotation about z axis (rad)

On the opposite, we can see from Fig. 9 that the more rigid element rotates of a maximum value of about $1,5 \text{ deg}$. The actual lander rotation will lie in between two values obtained with two different models.

x displacement

Fig. 10 and Fig. 11 show plots of x displacement. From plots we can see that maximum values of x displacement are placed for both configuration at the free end of the beam and displacement value are almost the same. Then, we can conclude that from x displacement point of view the two models are equivalent.

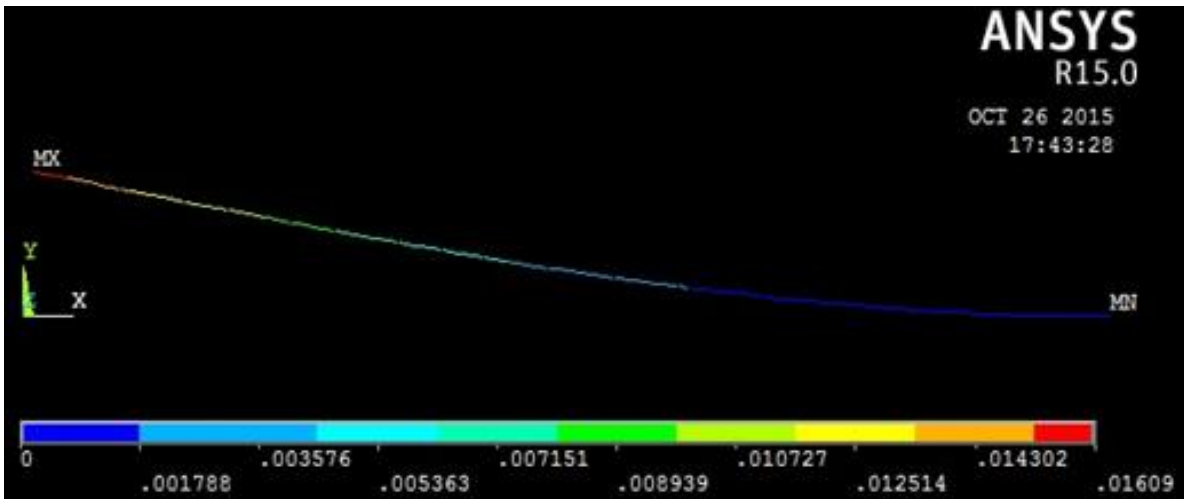


Fig. 10 Arm only, x displacement (m)

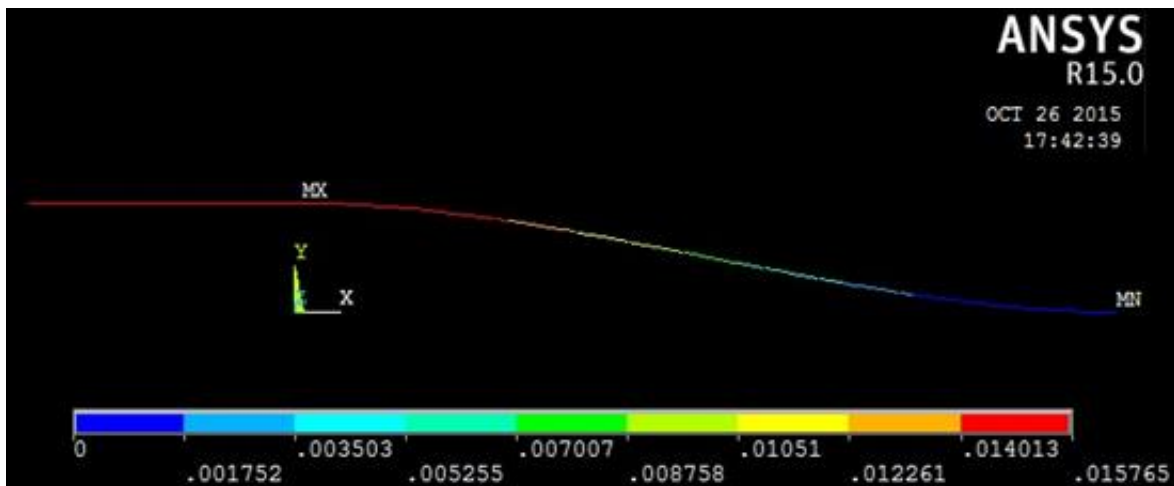


Fig. 11 Arm and lander, x displacement (m)

Bending stress

Since the problem is mainly a flexure problem, bending stress results to be of main concern with respect to other stress type (axial, torsional). In the continuation we will analyze different bending stress intensity for the two different model set up.

Regarding bending stress intensity, the two different models yield different results, as shown below in Fig. 12 and Fig. 13.

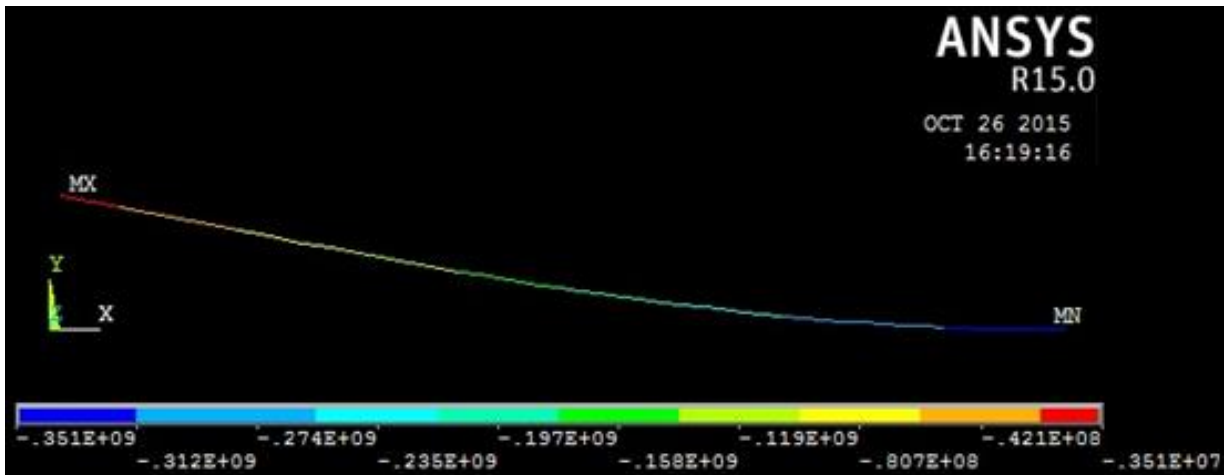


Fig. 12 Arm only, bending stress (MPa)

For free end beam, Fig. 12 shows that maximum stress is placed at fixed supported end and its intensity is below yielding stress value for this particular arm material.

For model which take into account lander rigidity, Fig. 13 shows that maximum stress intensity value is symmetrical with respect to half beam length and results to be well above material yielding stress, that results in a more conservative assumption, but also in the unfeasibility of using such material for arm realization. We will treat material choice in a dedicated section. Constant stress in lander beam representation and minimum absolute value of stress, confirm assumptions of lander rigidity much higher and not comparable to the one of arm, leading to infinite rigidity model.

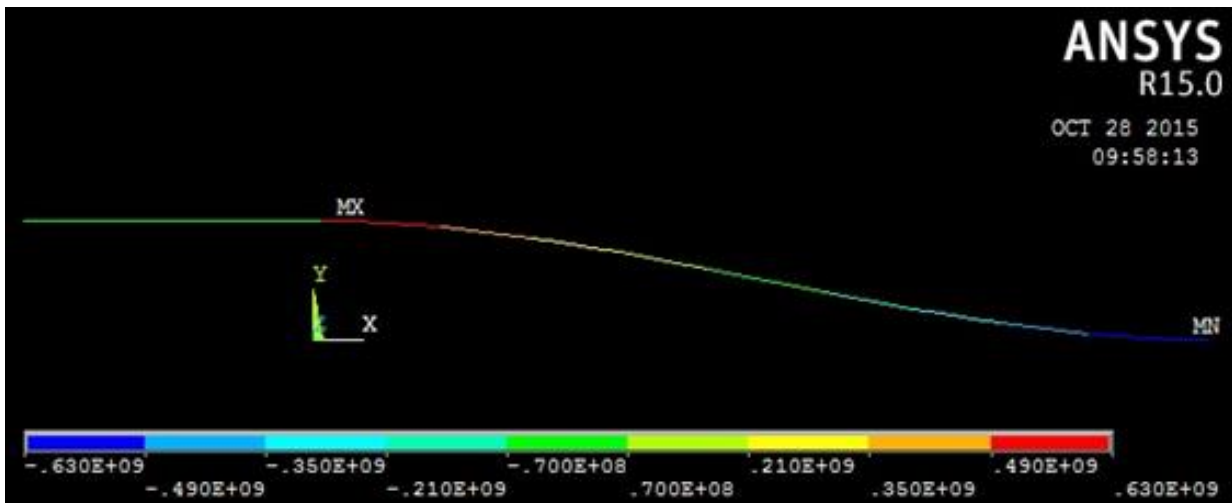


Fig. 13. Arm and lander, bending stress (MPa)

In plane arm model conclusions

From now on, since more conservative model for stress intensity resulted to be the one with lander representation, we will use this one for our following analysis. Besides, chosen model is a more precise representation of actual physical problem, since beam end connected to

lander structure will feel lander higher rigidity and thus congruence will be mandatory, leading to higher stress intensity.

Now we have chosen model of which we will make use in the continuation, in the next section we will discuss about possible benefits derived from use of second out of plane arm.

3.3.2 Out of plane arm model

To make overall hooking architecture more robust we can think about a second arm, which connects lander and shore rocks transversally and not only horizontally as we considered up to now. This results in lower x displacement and thus it would ensure a better stabilization. Thus, from x displacement point of view this architecture seems to be convenient compared to single arm architecture.

Otherwise, main indication that out of plane arm will be probably unfeasible solution is represented from buckling of upper arm shown in Fig. 14 where bending stress values are plotted.

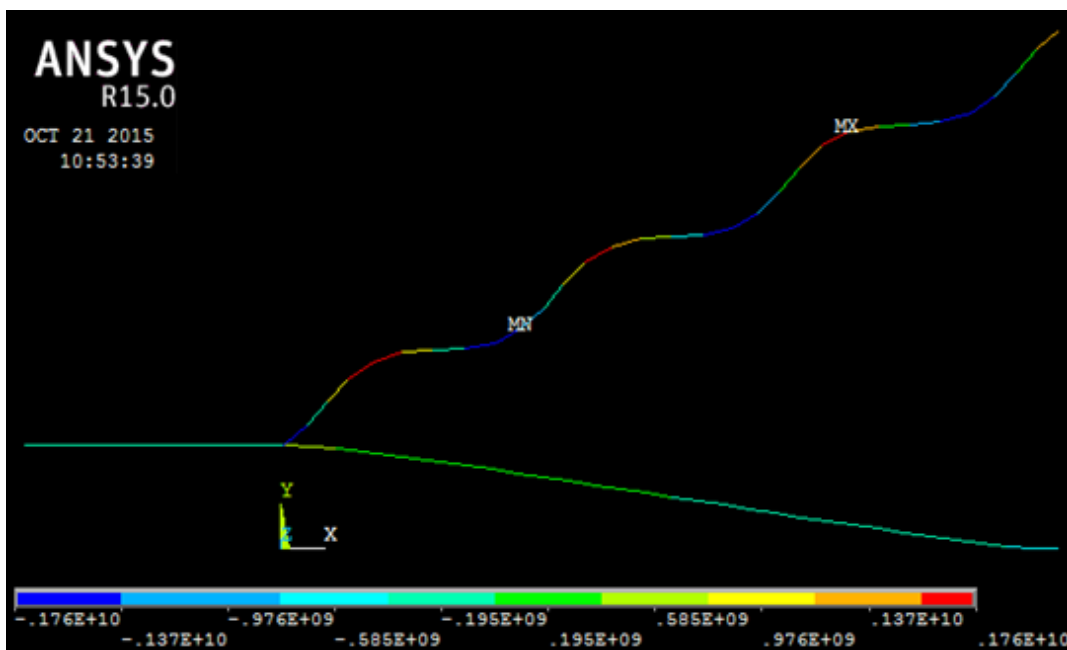


Fig. 14 Aluminum arms, bending stress (MPa).

As expected maximum stresses exceed yielding values, making Aluminum alloy out of plane arm unfeasible solution.

Further hypothesis

Material influence

One can think that using a more appropriate material, out of plane arm would become a feasible solution. Table 5 shows x -displacement and bending stress values for Ti 6Al-4V

structure, comprehensive of out of plane arm.

<i>Out of plane arm structure - Ti 6Al-4V</i>	
Lander x-displacement (m)	Maximum bending stress (MPa)
0,01	1130

Table 5. x-displacement and maximum bending stress for out of plane lander-arm structure. Imposed vertical displacement of 0,2 m.

Even if buckling of upper arm occurred to titanium alloy structure is well below the one of aluminum alloy structure, Table 5 shows that bending stress for titanium structure exceeds yielding stress as well as for aluminum structure plotted in Fig. 14.

Displacement limitations

We saw from previous results that Titanium is a better choice for this kind of problem, but there is no chance that such a structure can sustain a vertical displacement of 0,2 m.

One can think that using upper arm results in reduction of imposed vertical displacement and with displacement reduction hypothesis upper arm can sustain bending stress generated from reduced vertical displacement. We then analyzed bending stress for 10 cm and 5 cm vertical displacement.

<i>Out of plane arm structure - Ti 6Al-4V</i>	
Lander vertical displacement (m)	Maximum bending stress (MPa)
0,1	1100
0,05	1000

Table 6. Maximum bending stress for out of plane lander-arm architecture, considering vertical displacement limitations.

We can see from Table 6 that lowering vertical displacements stress intensity reduction occurs, as expected, but maximum value of stress still exceed yielding stress for imposed vertical displacement of 10 cm. For 5 cm imposed vertical displacement maximum stress results to be just below yielding value, representing still an unfeasible solution for fatigue considerations.

Out of plane arm model conclusions

We have seen from these last simulation's results that even changing material properties and lowering vertical displacement values, out of plane arm solution results unfeasible because of high bending stress generated inside the structure. Thus, from now on we solely consider single arm configuration.

3.3.3 In plane arm model cross sections

Now we had chosen the model to be used, for our subsequent analysis, we consider different section types and analyze resulting bending stress and reactions at fixed supported

end. Reactions we consider at fixed supported end are vertical reaction (F_y) and moment about z axis (M_z). These values will be used to choose proper hooking system, since it must be capable of balance yielded reactions. Normal reactions at fixed supported (F_x) will be neglected in the following analysis because much smaller compared to other two reactions mentioned above.

Material we consider for following analysis is Ti 6Al-4V, since we saw that Aluminum alloy is not capable of tolerating bending stress value yielded from chosen model.

In the following analysis we solely consider cross sections that yield significant results for our analysis, so for each section type only one section of proper dimensions will be presented.

Ring section

Fig. 15 shows cross section dimension and properties, while Table 7 shows yielded values for root shear force, bending moment about z axis and maximum bending stress.

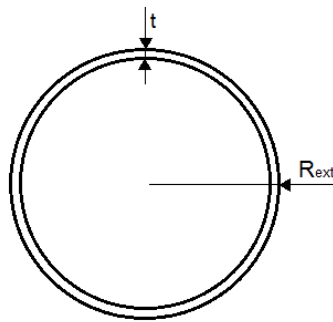


Fig. 15. Ring section, $R_{ext} = 1\text{ cm}$, $t = 1\text{ mm}$.

<i>Ring section</i>	
Shear force (N)	215
Bending moment (Nm)	155
Maximum stress (MPa)	570

Table 7. Ring section results. Imposed vertical displacement of 0,2 m.

L section

Fig. 16 shows cross section dimension and properties, while Table 8 shows yielded values for root shear force, bending moment about z axis and maximum bending stress.

<i>L section</i>	
Shear force (N)	175
Bending moment (Nm)	130
Maximum stress (MPa)	530

Table 8. L section results. Imposed vertical displacement of 0,2 m.

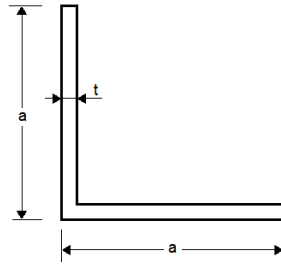


Fig. 16. L section. $a = 3 \text{ cm}$, $t = 1 \text{ mm}$.

H section

Fig. 17 shows cross section dimension and properties, while Table 9 shows yielded values for root shear force, bending moment about z axis and maximum bending stress.

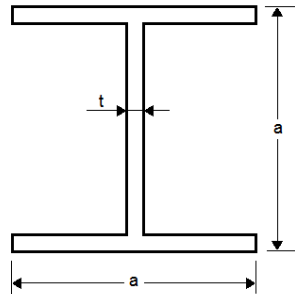


Fig. 17. H section. $a = 2 \text{ cm}$, $t = 1 \text{ mm}$.

<i>H section</i>	
Shear force (N)	106
Bending moment (Nm)	77
Maximum stress (MPa)	570

Table 9. H section results. Imposed vertical displacement of 0,2 m.

T section

Fig. 18 shows cross section dimension and properties, while Table 10 shows yielded values for root shear force, bending moment about z axis and maximum bending stress.

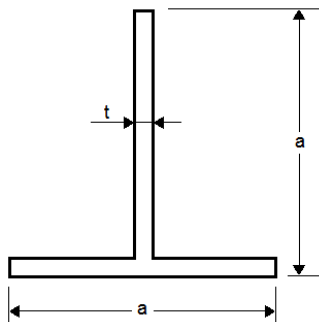


Fig. 18. T section $a = 2 \text{ cm}$, $t = 1 \text{ mm}$.

<i>T section</i>	
Shear force (N)	54
Bending moment (Nm)	38
Maximum stress (MPa)	570

Table 10. T section results. Imposed vertical displacement of 0,2 m.

Z section

Fig. 19 shows cross section dimension and properties, while Table 11 shows yielded values for root shear force, bending moment about z axis and maximum bending stress.

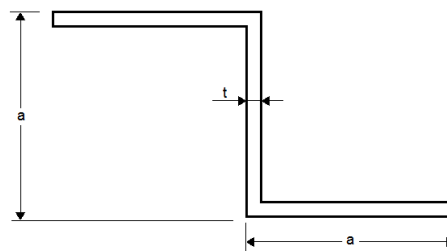


Fig. 19. $a = 2 \text{ cm}$, $t = 1 \text{ mm}$.

<i>Z section</i>	
Shear force (N)	263
Bending moment (Nm)	195
Maximum stress (MPa)	335

Table 11. Z section results. Imposed vertical displacement of 0,2 m.

Table 12 summaries yielded results for different arm cross sections. Last column gives a first estimation of mass value for robotic arm, considering a straight beam of constant cross section.

<i>Arm cross section comparison</i>					
Section type	Overall size (m^2)	Bending stress (MPa)	Fixed support vertical reaction (N)	Fixed support moment reaction (Nm)	Mass rough estimation (kg)
Ring	$3,14 \cdot 10^{-4}$	570	215	155	0,4
L	$9 \cdot 10^{-4}$	530	175	130	0,4
H	$4 \cdot 10^{-4}$	570	106	77	0,4
T	$4 \cdot 10^{-4}$	570	54	38	0,27
Z	$1,8 \cdot 10^{-3}$	335	263	195	0,6

Table 12. Comparison of section results and properties.

Cross sections results discussion

From bending stress point of view, the more convenient section resulted to be Z section, while all other sections yield almost the same value for bending stress. However, for support reactions, mass and size values, Z section is the less suitable. Ring, L and H sections are quite the same for mass value, while, out of these three, for fixed support reaction values the more suited seems to be H section. Best section regarding mass and reaction values appears to be T sections, in particular for very low reaction values compared to ones of all other sections.

Selection criterion will be considered in this section is out of plane (along z-axis) displacement. Since our goal is to make the lander as stable as possible, we aim to reduce each displacement components. Theoretically, 2d model should not involve out of plane displacement because of dimension limitations, but being BEAM188 a three dimensional elements, also under two dimensional loads conditions three dimensional behavior can occur, depending on chosen section.

Table 13 summarizes z-component of displacement for selected sections.

It is easy to see that for asymmetric sections such as Z section and L section, z-displacement is not negligible, being of the order of several centimeters.

On the other hand, for axial symmetric section such as T section, H section and ring section really small (T section) displacement occurs or negligible (ring and H section) in z-direction.

<i>Cross section z-displacement</i>	
Section type	z-displacement (m)
H	0,277E-15
L	0,056
T	0,0042
Ring	0,384E-17
Z	0,086

Table 13. z-displacement for different cross sections. Imposed vertical displacement of 0,2 m.

3.3.4 Transversal hooking

For sake of completeness we now have a quick look of arm behavior if hooking between arm and shoreline rocks is not horizontal, as considered so far, but it results to be transversal.

Simulation presented here have been yielded considering ring cross section and hooking height of 1 m.

From Table 14 we see that all numerical values of represented quantities are below respective values for horizontal case. Then, we can conclude that from reactions and stress

point of view, horizontal case comprehends transversal case as well. From now on we just refer to horizontal hooking case. Fig. 20 shows bending stress values for sake of example of transversal hooking model set up.

<i>Transversal hooking (hooking height 1 m)</i>	
Shear stress (N)	142
Bending moment (Nm)	122
Maximum stress (MPa)	450

Table 14. Results for ring cross section considering transversal hooking at height of 1 m.

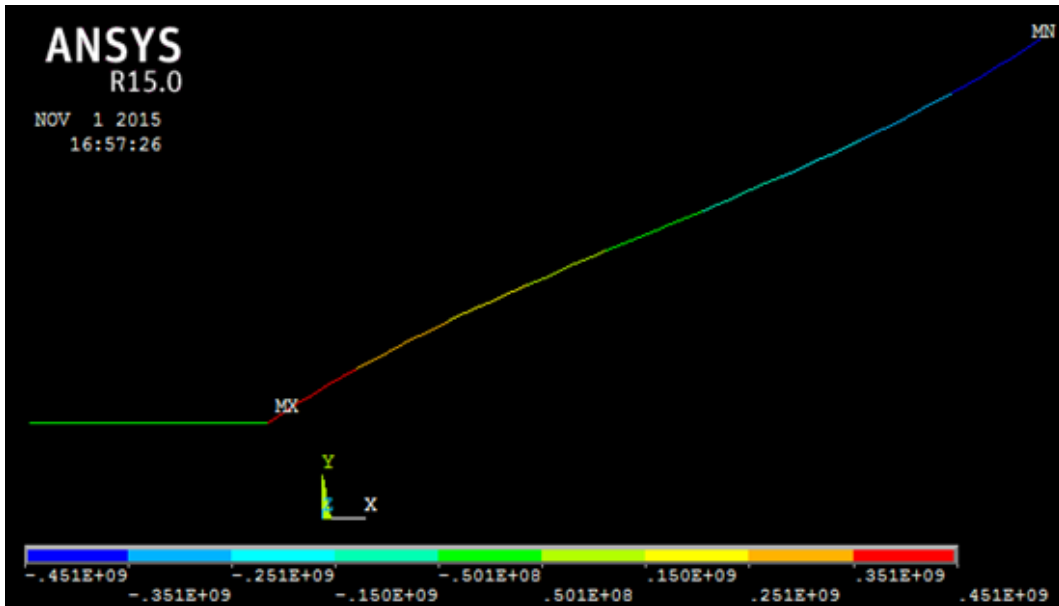


Fig. 20. Bending stress for ring section considering transversal hooking at height of 1 m.

3.4 3d model

Up to now we have presented 2d model that has been used to obtain structural results and at the end of the previous section we have singled out some possible sections to be used for robotic arm.

Now we present a 3d model in order to verify if 2d model results can be considered valid also in a three dimensional problem. If two models result to be in agreement we can validate our results and proceeding with cross section choice.

In the following section we will consider each selected arm cross sections and analyze vertical displacement problem from a three dimensional point of view. In addition, for 3d model we will make use of two robotic arms instead of one, since this configuration clearly guarantees better in-plane stabilization as well as redundancy factor.

With Ansys APDL® we set up a 3d model, using SHELL181 element in place of BEAM188 to simulate lander behavior and maintaining BEAM188 element to simulate robotic arms.

Fig. 21 shows 3d model set up. 0,2 m of vertical displacement has been applied to surface area and fixed supports have been applied to beam ends not connected to shell element.

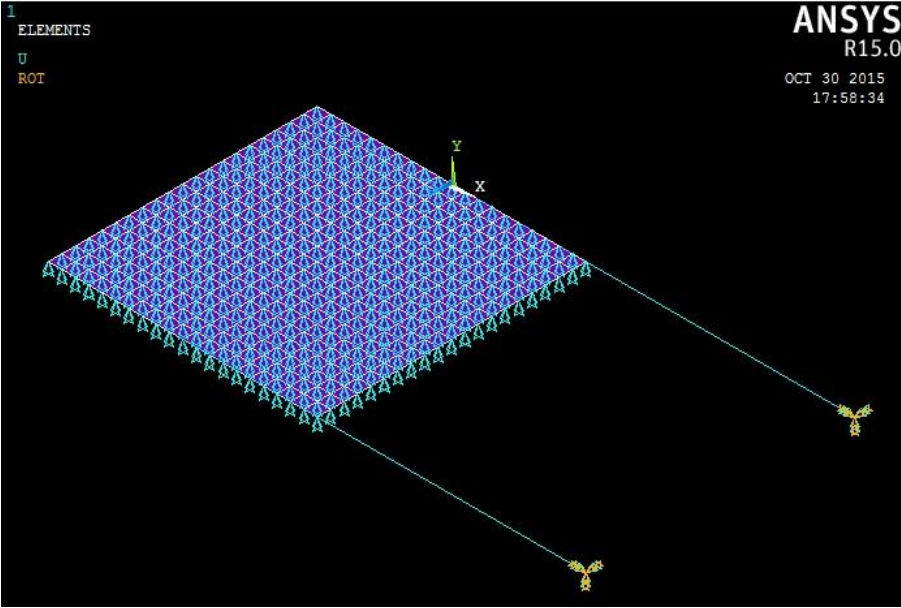


Fig. 21. 3d model set up

3.4.1 2d/3d geometrical comparison

2d model gave us some useful information about structural behavior of various sections; in order to verify our 3d model to be in agreement with 2d model results, we first checked that 2d results which did not depend from section or material selection, but only on geometrical model formulation (i.e. equal for all sections and materials selection) are the same of 3d model results. Then we see if infinite rigidity approximation used for 2d model can be approximated in three dimensional model too, using a thick plate in place of beam element.

Fig. 22 Fig. 23 show rotation about z axis and displacement along x axis respectively. Comparing with results plotted in Fig. 9 and Fig. 11 we see that both displacement and rotation values obtained with 3d model are really close to ones obtained with 2d model and so we can conclude the two models are in agreement from geometrical point of view.

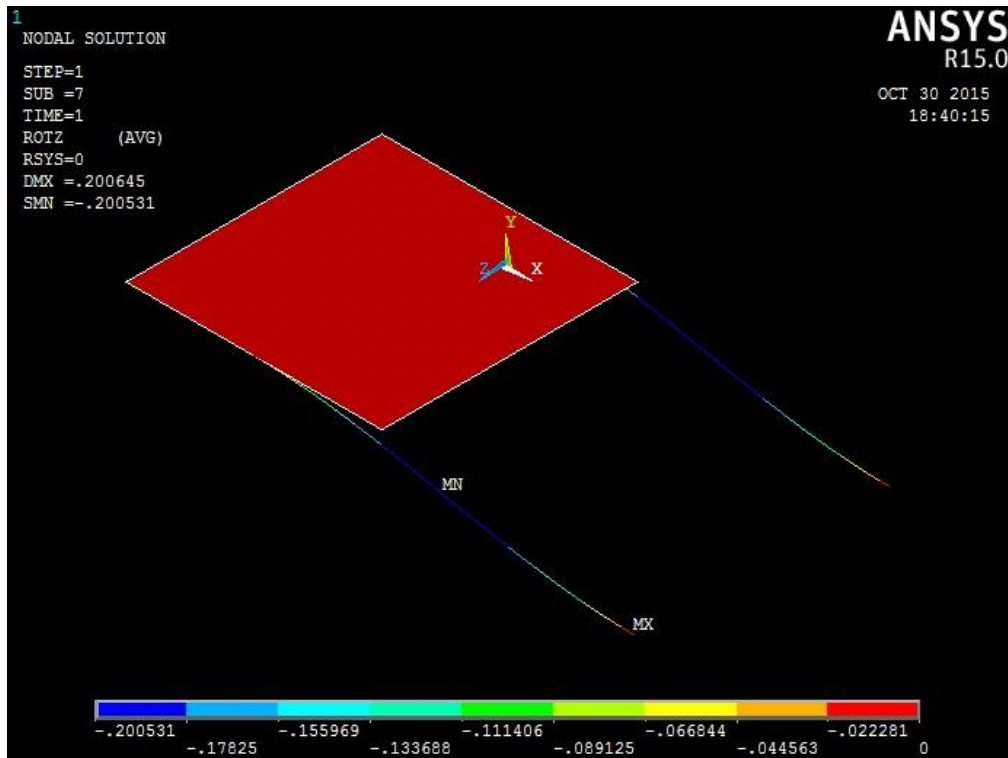


Fig. 22. Rotation about z axis (rad)

For discussion completeness, we have to specify that geometrical results have been yielded with ring cross section shown in Fig. 15. Since they only depend on geometrical problem formulation, using other possible cross section types would have yielded same results.

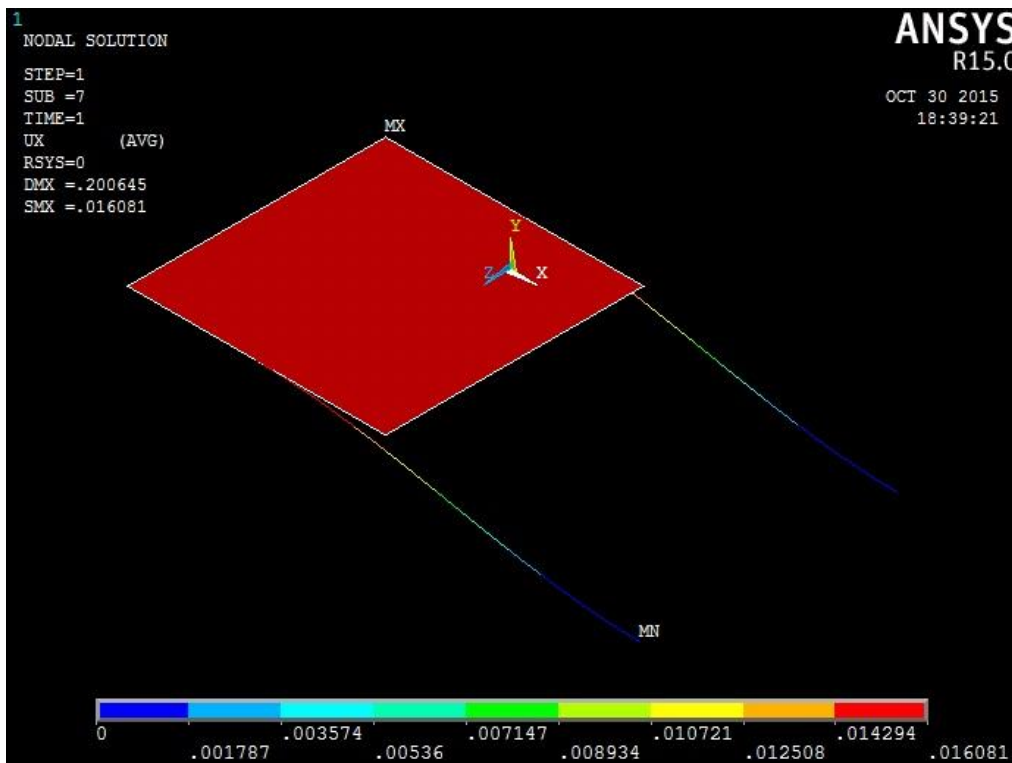


Fig. 23. x-component of displacement (m).

Now we have confirmed geometrical validity of three dimensional model, in the following section we will have a look at structural results.

We first compare two dimensional model results with three dimensional model results considering ring cross section represented in Fig. 15. Ring cross section will be treated and discussed in detail, while for H section and T section we will just have a quick look at results correspondence, before choosing best section option.

3.4.2 2d/3d section comparison

Ring section

Fig. 24 shows bending moment about z axis yielded with three dimensional model. Comparing Fig. 24 with bending moment value plotted in Table 7 we can see that maximum values are almost the same for three dimensional model and two dimensional one.

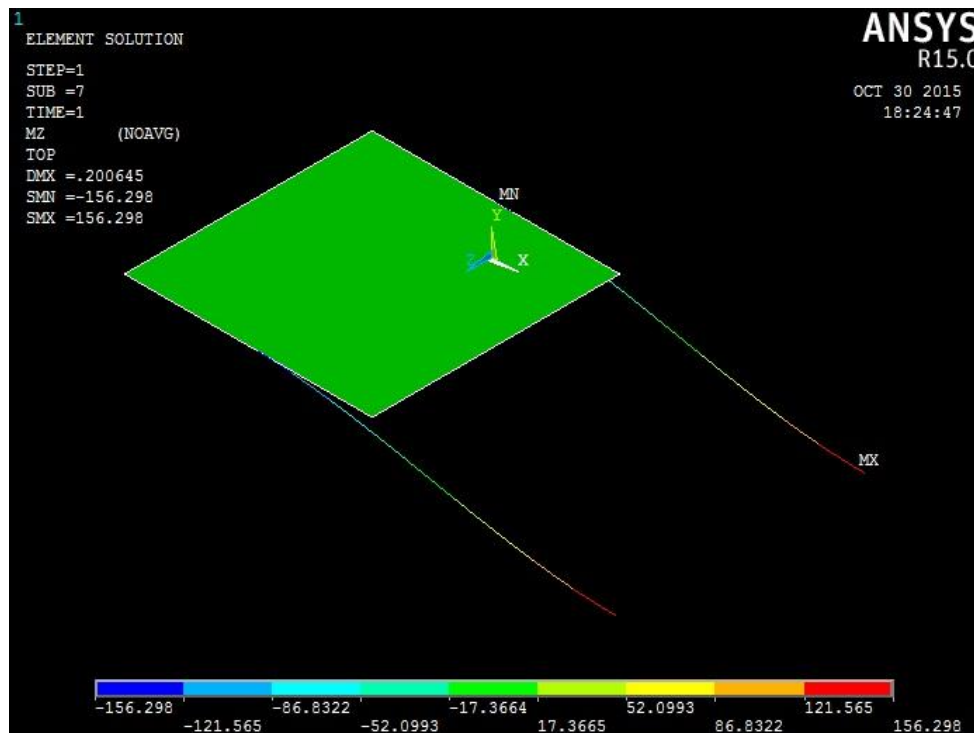


Fig. 24. Bending moment about z axis (Nm)

Fig. 25 shows vertical shear force. Squares and rectangles on shell elements are presents because of poor refinement of shell element mesh. Computational speed, because of large number of implemented simulations, has been preferred to mesh refinement. This has been possible, without losing information reliability because at this point of the work we are not interested in behavior at interface between beam and shell, but mainly we want to focus on support reactions which will be used to determine hooking system mechanism dimensions (see Section 5). We take into account arm critical behavior looking at bending stress generated by vertical displacement.

Comparing Fig. 25 with shear force value plotted in Table 7 we can suppose that fixed support reaction will be close to each other.

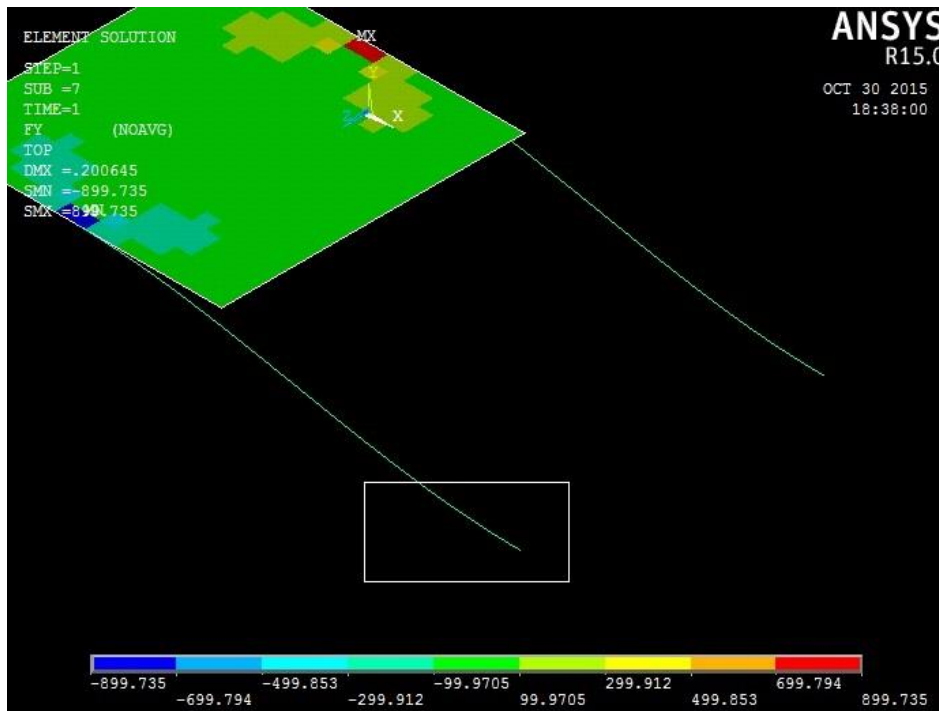


Fig. 25. Shear force along y direction (N)

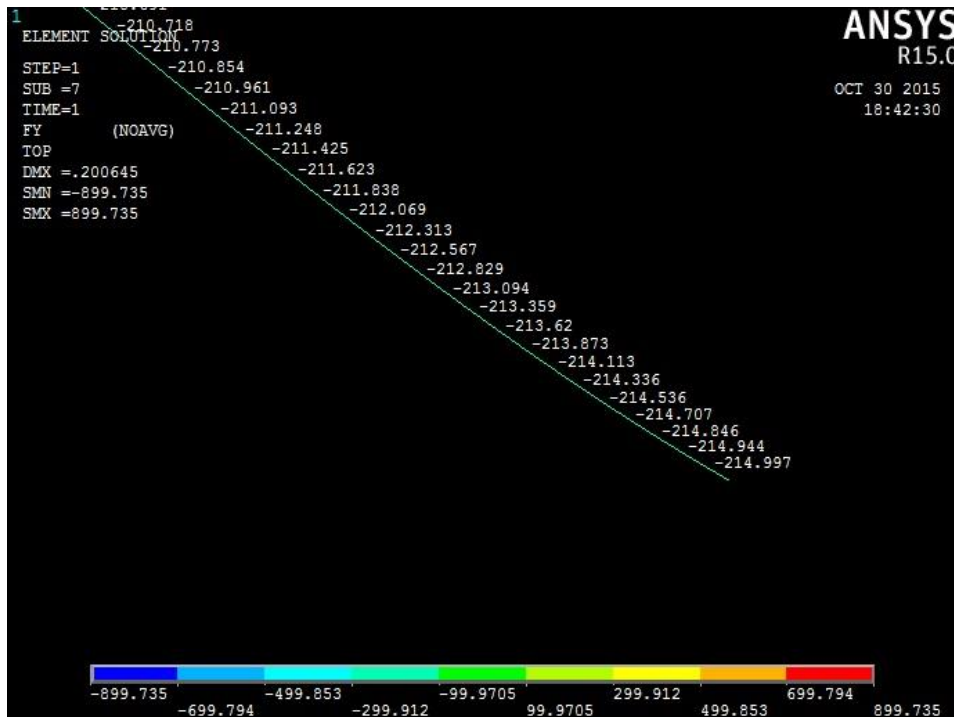


Fig. 26. Numerical value of shear force along y direction close to fixed supported beam end (N)

To confirm this first assumption we can look at Fig. 26 that shows zoom view of area surrounded by white box in Fig. 25 that shows values correspondence.



Fig. 27. Bending stress (MPa).

Fig. 27 shows bending stress produced by vertical displacement. Comparing Fig. 27 with bending stress value plotted in Table 7 we can see that stress values only differ for 8 MPa. Then we can conclude that three dimensional model is in agreement with two dimensional one.

We now proceed to have a quick look at correspondence between 2d model and 3d model also for other two selected sections, i.e. H section and T section, before choosing more suited section for displacement problem.

H section

We limit ourselves to report in Table 15 3d simulation results for H section compared to 2d model results.

<i>H section</i>		
Element	2d model	3d model
Fy (N)	106	- 107
Mz (Nm)	77	77
Bending stress (MPa)	570	579

Table 15. 2d/3d model results comparison for H section.

Table 15 shows correspondence between two dimensional and three dimensional model.

T section

As for H section, we limit ourselves to report in Table 16 3d simulation results for T section compared to 2d model results.

<i>T section</i>		
Element	2d model	3d model
Fy (N)	54	- 107
Mz (Nm)	38	77
Bending stress (MPa)	570	579

Table 16. 2d/3d model results comparison for T section.

Table 16 shows correspondence between two dimensional and three dimensional model.

3.5 Cross section choice

So now we have concluded 3d model is in agreement with 2d model also from a structural point of view we can proceed to cross section choice.

Referring to Table 12 we see that from stress, reactions and mass point of view the overall best option is represented by T section. It should also be considered that robotic arm must be capable of assuming different possible configurations, in response to external environment (for more detailed treatment of this topic see Section 4 and Section 5) and then in some configurations T section could result to be not symmetrical anymore from load point of view. As seen in previous section, not symmetrical cross sections lead to out of plane displacement for 2d model and then to torsional behavior for 3d model. Open sections are poor capable of sustaining torsional loads and for this purpose close sections should be preferred.

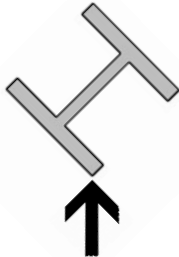


Fig. 28. Schematic representation of non-symmetrical vertical load on H section.

Same considerations made for T cross section stays for H section, lead us to cut down the choice of cross section for robotic arm to ring cross section only. Being ring cross section symmetric for any axis laying in cross sectional plane, theoretically torsion should not occur.

This assumption can clearly be done only considering robotic arm as a single straight beam as done till now. For actual robotic arm this is not true anymore, since joints, actuators, motors, and hooking mechanism are presents, leading to torsional effects also in straight arm configuration. Since, as just said, ring cross section is the more suited to face torsional effects, this results to be the best choice for robotic arm cross section.

References

- [1] THIEL, Markus, et al. The ROSETTA Lander anchoring system. In: *10th European Space Mechanisms and Tribology Symposium*. 2003. p. 239-246.
- [2] http://mars.nasa.gov/mer/mission/spacecraft_rover_arm.html. Last access on November 2015.
- [3] http://www.nasa.gov/mission_pages/station/structure/elements/mss.html. Last access on November 2015
- [4] JOURNEE, J. M. J.; PINKSTER, Jakob. Introduction in ship hydro-mechanics. *Delft University of Technology*, 2002.
- [5] LORENZ, Ralph D.; HAYES, Alexander G. The growth of wind-waves in Titan's hydrocarbon seas. *Icarus*, 2012, 219.1: 468-475.
- [6] MILITARY HANDBOOK, S. F. Metallic Materials and Elements for Aerospace Vehicle Structures. *Department of Defense, Washington DC (Nov. 1990)*, 1972, 9.16-9.20.

4 Robotics

4.1 Robotics generalities

During previous load analysis we showed preliminary sizing of robotic arm, giving arm length, cross section and material. Up to now we considered robotic arm as uniform straight beams, but clearly this assumption has been made just for preliminary sizing sake of simplicity. Actual arms should have motion capability, in order to perform different trajectories in response to shoreline irregularities and unexpected obstacles and also should be capable to assume folded configuration for launch.

We then decompose uniform straight beams in a certain number of components, that from now on we will call links. Links have different length (total length must be equal to straight beam length) and their cross sections and material are ones determined before.

Arms functioning did not need prismatic joints utilization, so we choose to use only rotational joints between links in order to lower arm complexity and weight with respect to prismatic joints utilization.

We modeled robotic arm as an anthropomorphic arm, with 6 rotational degrees of freedom along its kinematic chain [1]. It can be seen as a two links planar arm with a rotational degrees of freedom in links connection joint. Other five degrees of freedom will be located as follow, two at lander-arm connection and three at free arm end, in order to obtain a spherical wrist which ensure a high adaptability of hooking mechanism located at arm free end.

To determine direct kinematic of this open chain (i.e. there exists a single link sequence that connects arm's ends) we need to define position and orientation of consecutive links, having fixed appropriate reference system following Denavit-Hartenberg convention [1].

Link schematic representation for anthropomorphic arm and its coordinates systems are shown in Fig. 29.

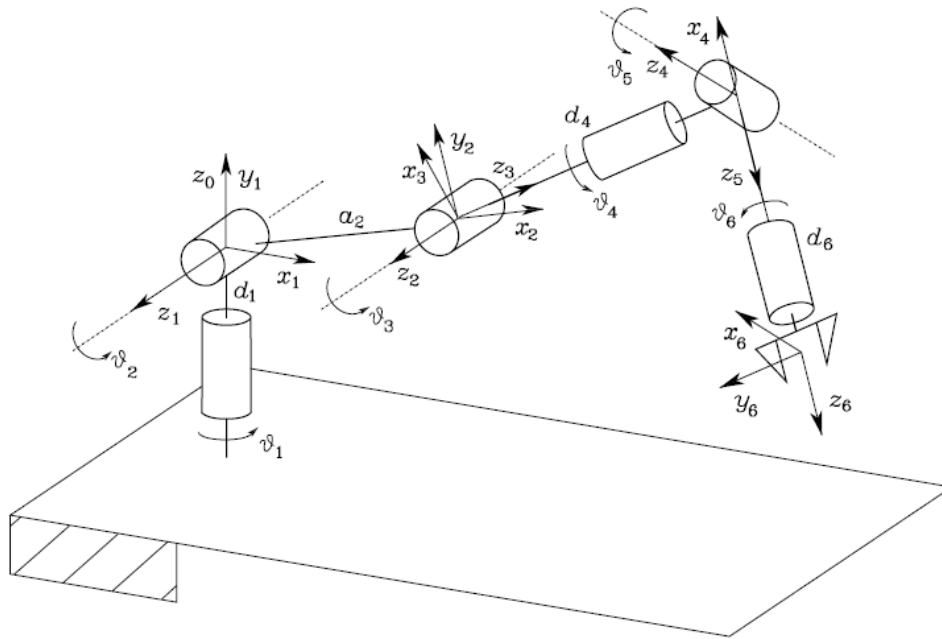


Fig. 29. Anthropomorphic arm sketch. Joints coordinate system are shown. [1]

With reference to Fig. 30 we can define [1]:

- z_i , that lies along $i+1$ axis.
- O_i , that is located at intersection between z_i axis and perpendicular line to both z_i e z_{i-1} axes.
- O'_i , that represents intersection of common perpendicular defined before with z_{i-1} axis.
- x_i , that is oriented along common perpendicular line of z_i and z_{i-1} axes, with positive direction from joint i to joint $i+1$.
- y_i , that completes a right hand reference system.

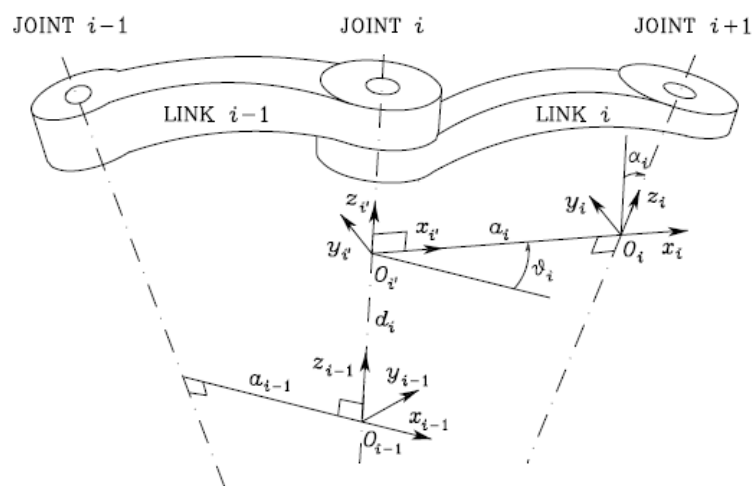


Fig. 30. Schematic representation of two subsequent joint coordinates systems. [1]

In order to define coordinates system with respect to precedent one, only four parameter need to be used, called Denavit-Hartenberg parameters [1]:

- a_i , distance between O_i and O'_i
- d_i , coordinates of O_i on z_{i-1}
- α_i , angle about x_i axis, between z_{i-1} axis and z_i axis, considered positive for anticlockwise direction
- θ_i , angle about z_{i-1} axis between x_{i-1} axis and x_i axis, considered positive for anticlockwise direction

Table 17 summarizes Denavit-Hartenberg parameters for each links of our structure.

Link	a_i	α_i	d_i	θ_i
1	0	$\pi/2$	5 cm	θ_1
2	75 cm	0	0	θ_2
3	0	$\pi/2$	0	θ_3
4	0	$-\pi/2$	75 cm	θ_4
5	0	$\pi/2$	0	θ_5
6	0	0	10 cm	θ_6

Table 17. Denavit-Hartenberg parameters

Generic expression of transformation matrix which allows to switch from generic $i-1$ reference system to i reference system can be written as [1],

$$A_i^{i-1}(q) = \begin{bmatrix} \cos(\theta_i) & -\sin(\theta_i) \cdot \cos(\alpha_i) & \sin(\theta_i) \cdot \sin(\alpha_i) & a_i \cdot \cos(\theta_i) \\ \sin(\alpha_i) & \cos(\theta_i) \cdot \cos(\alpha_i) & -\cos(\theta_i) \cdot \sin(\alpha_i) & a_i \cdot \sin(\theta_i) \\ 0 & \sin(\alpha_i) & \cos(\alpha_i) & d_i \\ 0 & 0 & 0 & 1 \end{bmatrix}$$

From there it is possible to determine i -joint position [1]. By extension, it is possible to determine position of end-effector (i.e. robotic arm free end) with respect to base reference system (i.e. robotic arm-lander connection). For anthropomorphic arm that yields [1].

$$T_e^b(q) = \begin{bmatrix} n_e^b(q) & s_e^b(q) a_e^b(q) & p_e^b(q) \\ 0 & 0 & 1 \end{bmatrix}$$

Where e stays for end-effector and b stays for base. Since for our case end effector reference system is identified by number 6 and base reference system is identified by number 0 we can write [1]

$$p_6^0 = \begin{bmatrix} d_6 s_5 \cdot (c_1 c_{23} c_4 + s_1 s_4) + c_1 c_5 s_{23} d_6 + c_1 \cdot (s_{23} d_4 + a_2 c_2) \\ d_6 s_5 \cdot (c_4 s_1 c_{23} - c_1 s_4) + d_6 s_1 s_{23} c_5 + s_1 \cdot (s_{23} d_4 + a_2 c_2) \\ d_6 c_4 s_{23} s_5 - d_6 c_{23} c_5 - c_{23} d_4 + a_2 s_2 + d_1 \end{bmatrix}$$

$$n_6^0 = \begin{bmatrix} c_6 c_5 \cdot (c_1 c_{23} c_4 + s_1 s_4) - c_6 c_1 s_{23} s_5 - s_4 c_1 c_{23} s_6 + s_1 s_6 c_4 \\ c_6 c_5 \cdot (c_4 s_1 c_{23} - c_1 s_4) - c_6 s_1 s_{23} s_5 - s_6 s_4 s_1 c_{23} - s_6 c_1 c_4 \\ c_6 c_4 s_{23} c_5 + c_6 c_{23} s_5 - s_4 s_{23} s_6 \end{bmatrix}$$

$$s_6^0 = \begin{bmatrix} -s_6 c_5 \cdot (c_1 c_{23} c_4 + s_1 s_4) + s_6 c_1 s_{23} s_5 - s_4 c_1 c_6 c_{23} + s_1 c_4 c_6 \\ -s_6 c_5 \cdot (s_1 c_{23} c_4 - c_1 s_4) + s_6 s_1 s_{23} s_5 - s_4 s_1 c_6 c_{23} - c_1 c_4 c_6 \\ -s_6 c_4 s_{23} c_5 - s_6 c_{23} s_5 - s_4 s_{23} c_6 \end{bmatrix}$$

$$a_6^0 = \begin{bmatrix} s_5 \cdot (c_1 c_{23} c_4 + s_1 s_4) + c_1 c_5 s_{23} \\ s_5 \cdot (s_1 c_{23} c_4 - c_1 s_4) + s_1 c_5 s_{23} \\ c_4 s_{23} s_5 - c_{23} c_5 \end{bmatrix}$$

Where for sake of abbreviation we used,

- $\cos(\theta_i) = c_i$
- $\sin(\theta_i) = s_i$
- $\cos(\theta_i + \theta_{i-1}) = c_{i,i-1}$
- $\sin(\theta_i + \theta_{i-1}) = s_{i,i-1}$

We make use of Robotic toolbox [2] Matlab package, in order to find, once defined kinematic elements, position, velocity, acceleration for each joint for different trajectories, written as displacement from initial to final position. For direct kinematic equation we can write [2],

$$\vec{x} = k(\vec{q})$$

Where \vec{q} vector represents joints position expressed by joints' angle θ , while \vec{x} vector represents trajectory Cartesian coordinates [2]. So, once joints angle are known, it is possible to determine end-effector position.

Instead from inverse kinematic, once final trajectory position is note, it is possible to determine joints' angle [2].

4.2 Simulation

4.2.1 Kinematic

We exploited direct kinematic properties in order to perform simulation of typical arm trajectories. Fig. 31 shows an example of initial and final position of robotic arm. Initial position represents arm folded configuration while final position is reached once lander have performed unfolding manoeuvre and it is about to ensure shoreline rock connection. This trajectory is used to determine information about system position and motion.

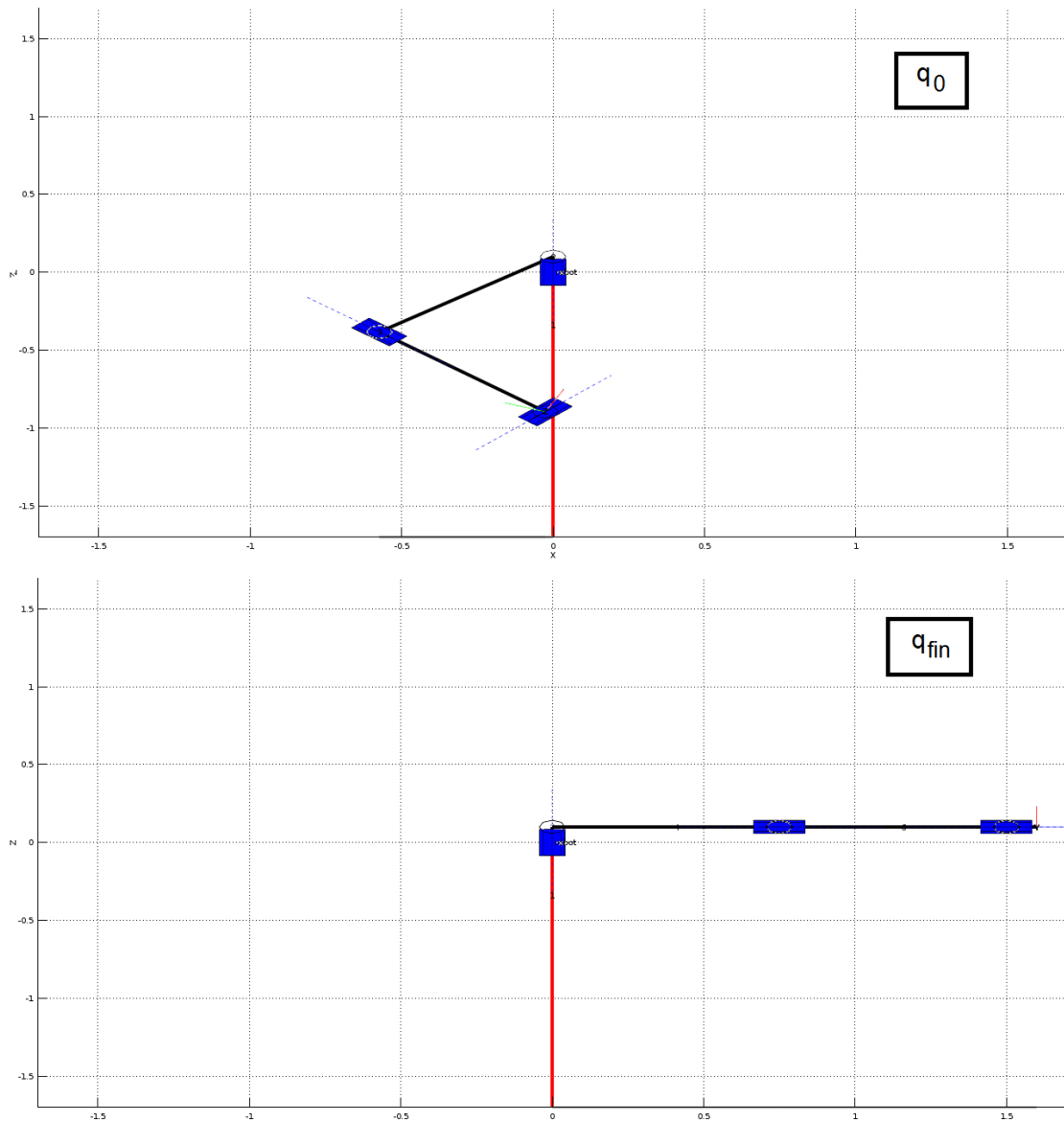


Fig. 31. Initial and final robotic arm position for considered trajectory.

Fig. 32 and Fig. 33 shows simulation results for trajectory considered above. Fig. 32 shows joints coordinates with respect to time and end effector position in Cartesian coordinates. Deployment time has been considered to be of 1 minute.

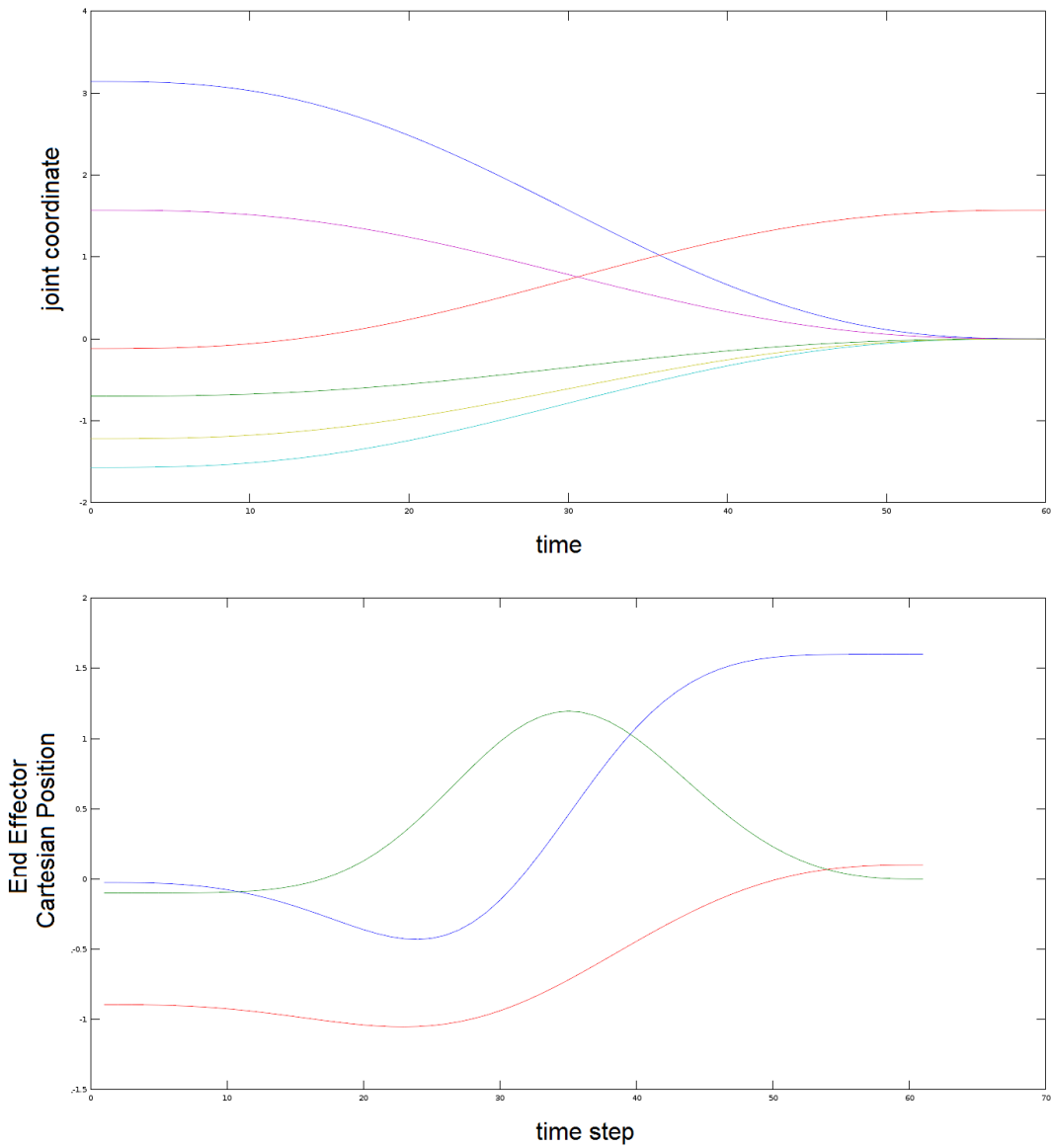


Fig. 32. Joint coordinate and end-effector Cartesian position for selected trajectory.

Fig. 33 shows angular velocity and acceleration for each joint during considered trajectory.

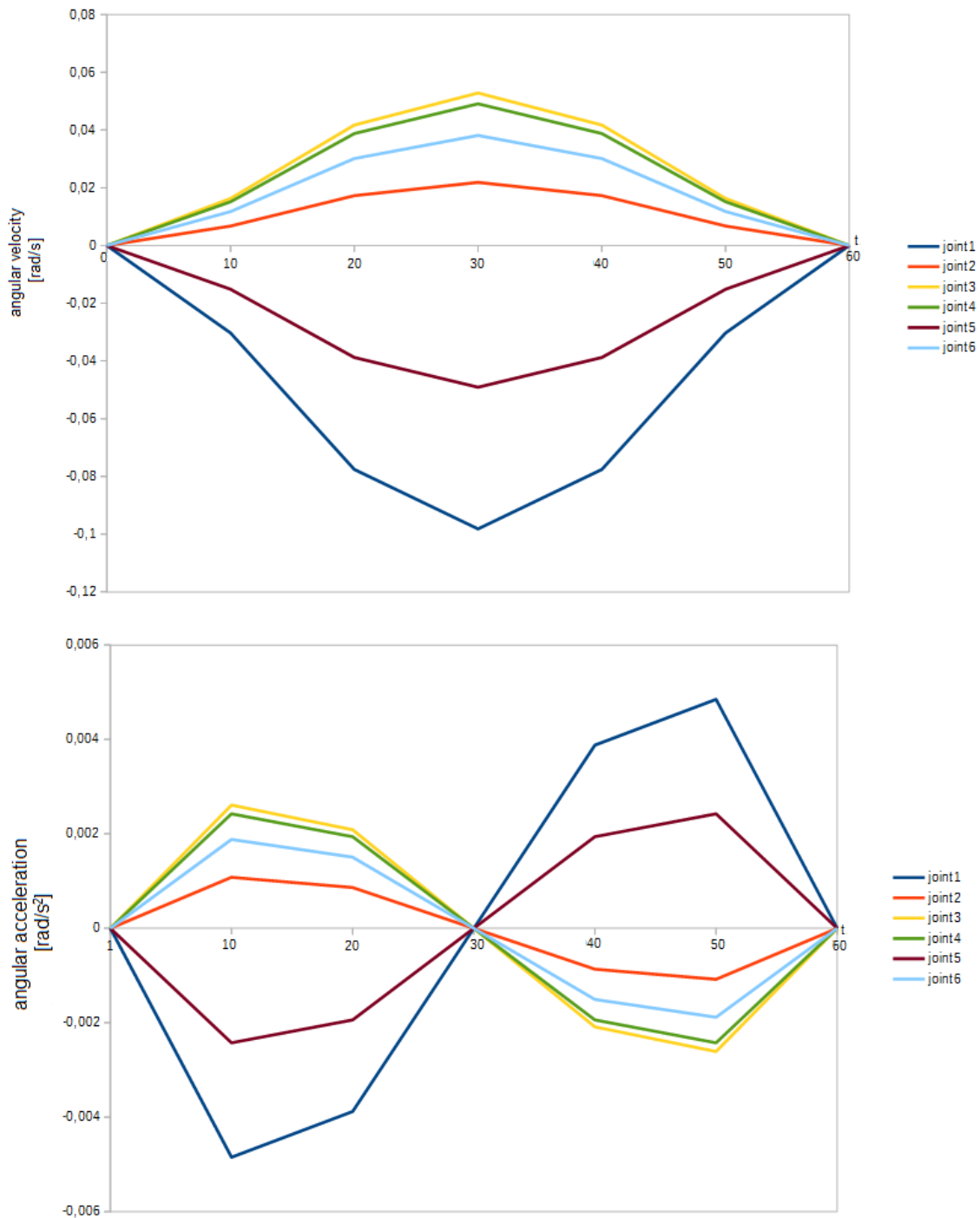


Fig. 33. Angular velocity and acceleration for each joint during considered trajectory.

4.2.2 Dynamic

What has been done up to now is a purely kinematic approximation, without considering real physical effects for links and joints. In a more accurate approximation, each link is supported by force and torque exerted by preceding link, it is subjected to its own weight

and to force and torque of subsequent link. Then we need to describe arm trajectories from a dynamic point of view in order to determine torque to be exerted during motion. We can write [2],

$$Q = M(q) \cdot \ddot{q} + C(q, \dot{q}) \cdot \dot{q} + F(\dot{q}) + G(q) + J(q)^T \cdot g$$

This equation represents a system of differential equations [2] where,

- q, \dot{q}, \ddot{q} , are joint coordinates, velocity and acceleration vector respectively.
- M , is inertial matrix
- C , is Coriolis matrix
- F , is friction force
- G , is gravitational load
- Q , is force vector of joint actuators
- J , is Jacobian matrix of end effector

Since we aim to determine joint servo motors characteristics, we exploit previous equation to give a first estimation of loads acting on joints during trajectory considered above for kinematic approximation.

Below we show some of most valuable results of simulation. We report torque values generated by gravitational load or inertial load with respect to joints coordinates. Regarding inertial loads we plotted elements on principal diagonal of inertia matrix M_{jj} that represent inertial loads felt by interested joints [2]. Out of diagonal elements of inertia matrix represent coupling between angular acceleration of joint j and torque on joint i [2].

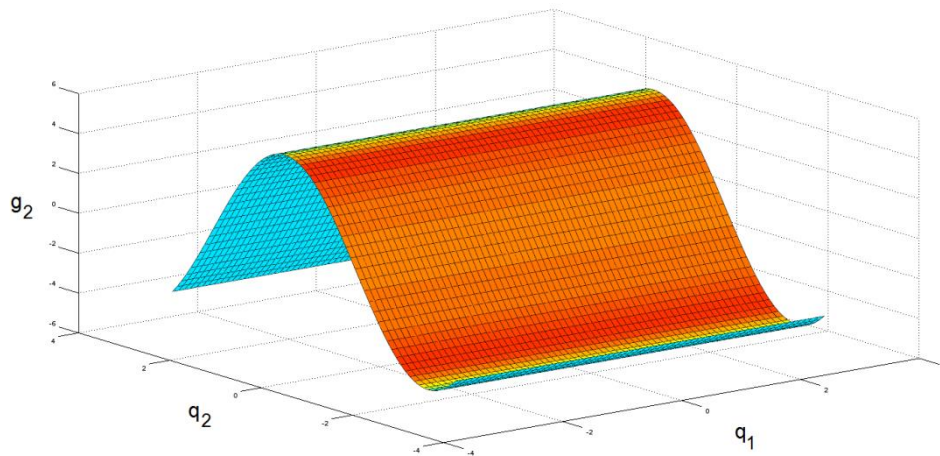


Fig. 34. Gravitational torque on joints 2.

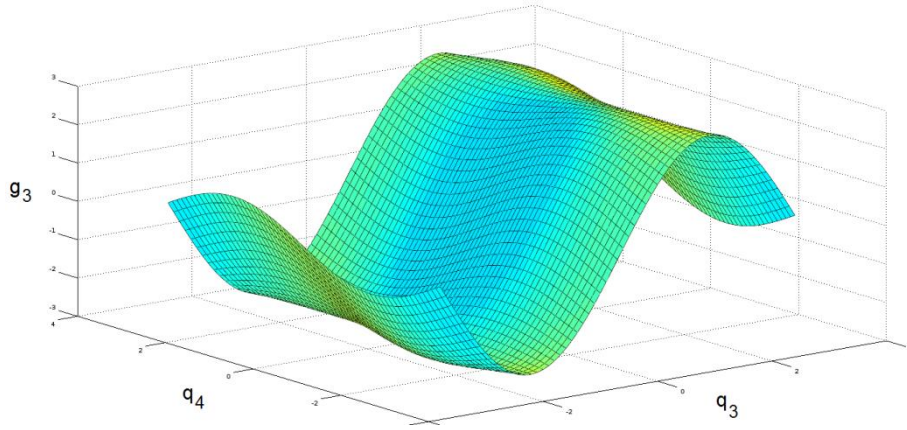


Fig. 35. Gravitational torque on joints 3.

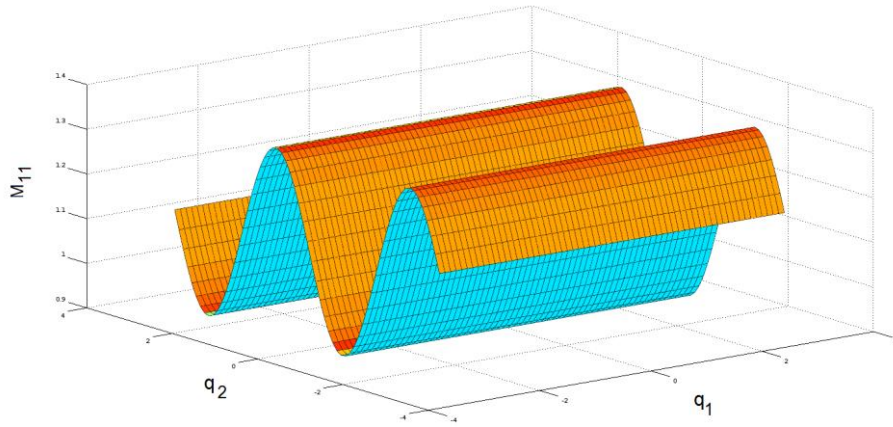


Fig. 36. First principal diagonal element of inertia torque on joints 2.

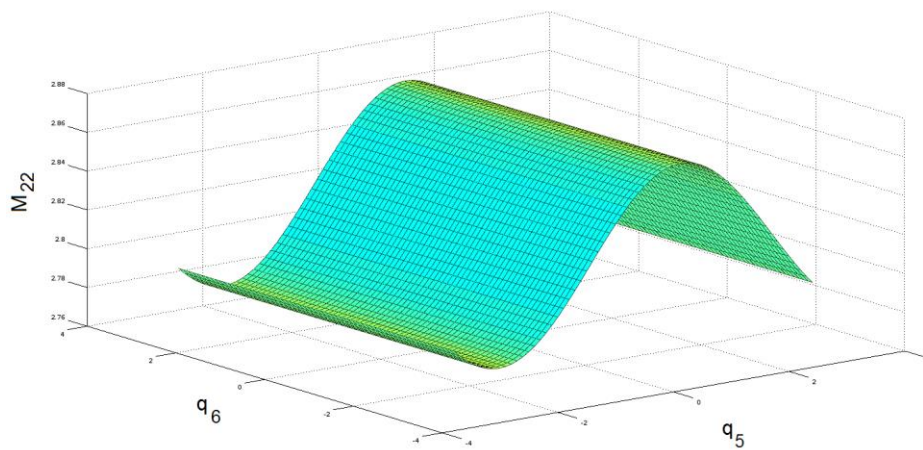


Fig. 37. Second principal diagonal element of inertia torque on joints 6.

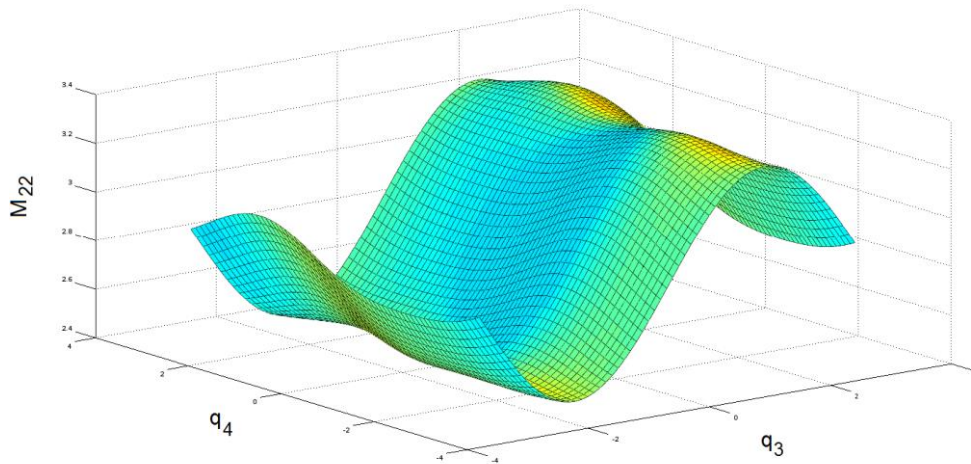


Fig. 38. Second principal diagonal element of inertia torque on joints 4.

Results shown in graph above do not take into account joints servo motors, but only links inertia and gravitational loads. Besides, Fig. 34 to 38 show results for all possible configurations between two subsequent joints, independently from trajectory [2]. Actual torque value felt by joints strongly depend also from frictional term in equation above [2]. Frictional contribution depends itself from servo motor choice, then in order to make a first estimation of joint actual torque we need to select servo motor model.

4.3 Servo motors

Fig. 39 shows conceptual sketch of revolution joint [3]. Some Servomotors and gearbox have been selected from Maxon and Harmonic Drive catalogue [3], since they have been already tested and used in space application and then can guarantee a quite high reliability. In addition to already treated selection criterions, as torque and velocity, servo motors and gearboxes have been selected in order to keep dimension and mass as low as possible.

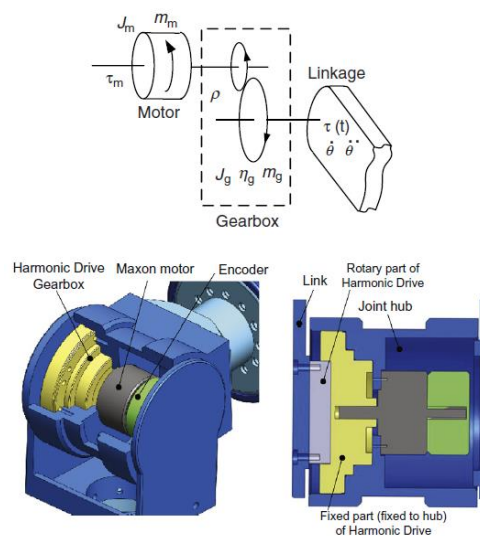


Fig. 39. Schematic representation of joints components [3]

Since it has been seen from simulations that gravitational and inertial torque values are below 5 Nm for all possible joint angles, we selected servo motors and gearboxes coupling capable of delivery output torque as high as 8 Nm. Servo motors and gearboxes selection influence frictional term in dynamic equation. Total torque founded considering servo motors and gearboxes friction could be higher with respect to previously yielded torque value. For this case joints torque are trajectory dependent [2].

Fig. 40 shows total torque values acting on each joints during selected trajectory. Total torque value has been yielded from summation of each term of dynamic equation above for chosen servo motor and gearbox.

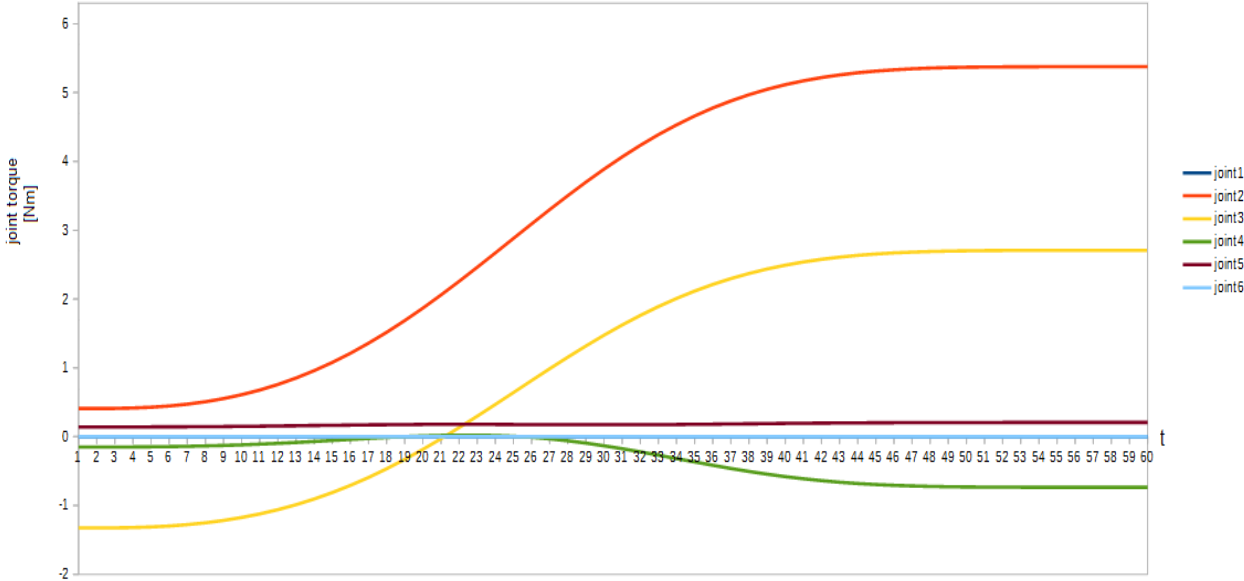


Fig. 40. Total torque on each joint for selected trajectory.

As we can see from graph above, yielded torque values for each joint are below torque value of servo motor and gearbox, hence servo motor and gearbox coupling selection can be considered an appropriate choice.

4.4 Joint angle limitations

Each joint will have of course angle limitation due to geometrical dimensions of joints themselves. Below we show calculations used to determine maximum joint allowable angle.

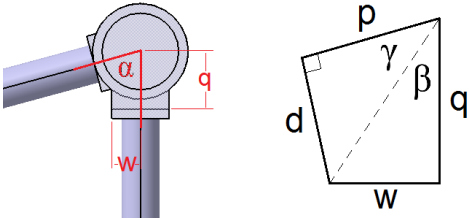


Fig. 41. Link-joint geometric relation.

With reference to Fig. 41, it is possible to determine an algebraic relation between joint dimensions and minimum allowable axial distance (d) from two subsequent links. Considering,

$$\alpha = \beta + \gamma$$

We can thus write,

$$\alpha_{min} = \arcsin\left(\frac{d_{min}}{\sqrt{w^2 + q^2}}\right) + \arctg\left(\frac{w}{q}\right)$$

We considered a reasonable value for d_{min} to be 2,5 cm. Since link radius has been determined (see Section 3) to be 1 cm, we obtain a minimum allowable distance between joints part to be 1,5 cm. This will be used to determine joints allowable angle interval.

Table 18 shows allowable angular interval for each rotational joints.

Joint 1	$0^\circ \leq \theta_1 \leq 360^\circ$
Joint 2	$-140^\circ \leq \theta_2 \leq 140^\circ$
Joint 3	$-140^\circ \leq \theta_3 \leq 140^\circ$
Joint 4	$0^\circ \leq \theta_4 \leq 360^\circ$
Joint 5	$-140^\circ \leq \theta_5 \leq 140^\circ$
Joint 6	$-130^\circ \leq \theta_6 \leq 130^\circ$

Table 18. Allowable angle interval for each robotic arm joints.

Fig. 42 shows sketch of robotic arm links and joints configuration and motion capability for each joint.

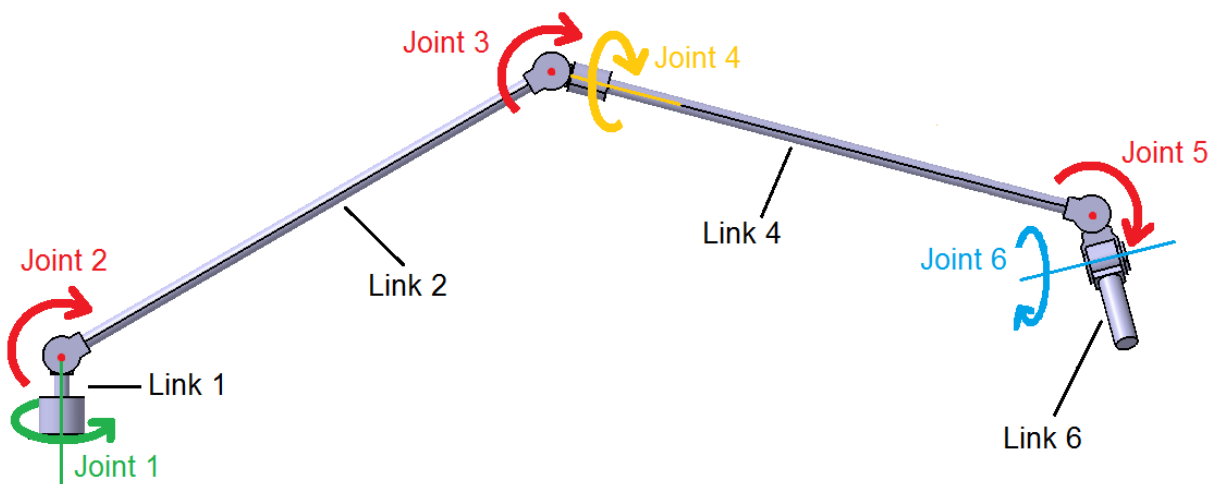


Fig. 42. Robotic arm sketch with joint motion capability.

4.5 Servo motors locking system

In this section some possible servo motors locking mechanisms will be discussed for joints motors. It must be pointed out that servo motors locking systems have not been studied in detail, in the following section some general considerations about locking system will be presented and discussed.

4.5.1 Arms joints locking system

As said in previous sections, once robotic arms have acquired proper orientation during hooking configuration, servo motors inside arms joints are supposed to lock in order to make a rigid connection between lander and shoreline rocks. Locked configuration can be obtained either with servo motors itself or with mechanical device. In the continuation, we will analyse both possibilities, showing pros and cons for each one.

First case we take into account is represented by auto locking of servo motor itself. That could be done if some particular servo motors will be used, called stepper motors. Stepper motors, differently from other servo motors, can hold their shaft in selected configuration and thus ensuring position holding [4]. With respect to other typologies of servo motors, stepper motors can exert higher value of torque [4]. Stepper motors are also indicated for robotic applications [4]. For our purpose, this resembles to be a well suited option, because there is not additional need of any other device but stepper motors, reducing system complexity. On the other hand, stepper motors need power supply to work for entire hooking configuration duration, since of course they can only maintain shaft position if switched on. Another drawback can be identified in high joint resulting mass, because of need of high performance and then heavy servo motor.

Now we take into consideration mechanical locking device. This second option would involve two mechanical parts, which can be coupled when joint desired position has been acquired. Once arm joint reach position to be fixed, servo actuator drives two pieces together, ensuring locking of entire joint. Fig. 43 show possible device solution in open configuration. This solution results to be more robust than previously presented one, because of possible higher torque sustainable. Cons for this solution can be evaluated as need of additional actuators, probably servo motors, which will increase overall system complexity, adding elements and also power supply need. Probably mechanical solution yield an overall joints mass that is below the one yielded in the case of servo motors auto locking mechanism, because two light motors can be used in this configuration, one for joint motion and one for locking system activation.

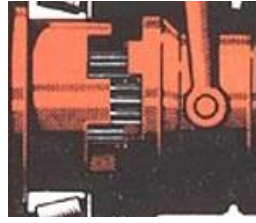


Fig. 43. Example of joints servo motor locking mechanism [6]

Table 19 summarizes pros and cons for two possible configurations.

Arm joints locking system	Pros	Cons
Auto-locking stepper motor	Simplicity	Mass Power
Mechanical	Sustainable torque Mass	Complexity

Table 19. Pros and cons for arm joint locking system. Electrical vs. mechanical.

From Section 3 we estimated maximum torque to be tolerated by robotic arms joints to be about 160 Nm , which is yielded value of bending moment close to hooking system and at lander-robotic arm interface. This clearly results to be far higher than maximum reachable torque value for light weight applications stepper motors [5], making servo motors auto locking system unfeasible. Furthermore, in arms folded configuration, i.e. launch and arrival configuration, arm joints have to be locked in order to maintain proper position that is clearly impossible to achieve with servo motors auto locking system for power supply consideration.

References

- [1] SICILIANO, Bruno, et al. *Robotics: modelling, planning and control*. Springer Science & Business Media, 2009.
- [2] CORKE, Peter. *Robotics, vision and control: fundamental algorithms in MATLAB*. Springer Science & Business Media, 2011.
- [3] ZHOU, Lelai; BAI, Shaoping; HANSEN, Michael Rygaard. Design optimization on the drive train of a light-weight robotic arm. *Mechatronics*, 2011, 21.3: 560-569.
- [4] LIPTÁK, Béla G. (ed.). *Process Control: Instrument Engineers' Handbook*. Butterworth-Heinemann, 2013.
- [5] <http://www.delta-line.com/it/hybrid-stepper-motors-C15.htm>. Last access on November 2015.
- [6] http://www.4x4abc.com/4WD101/diff_locks.html. Last access on November 2015.

5 Hooking mechanism

In this section two different hooking mechanisms will be presented for shoreline connection. As done in previous sections, sizing of hooking mechanisms has been performed considering worst displacement scenario, i.e. waves of 10 cm amplitude. Furthermore, we suppose for our preliminary calculations that rock connection takes place at wave crest or pit in order to consider maximum possible displacement of 20 cm. We split hooking configuration in two different case, frontal hooking and lateral hooking, referred to orientation of hooking spot with respect to lander.

What we want to obtain at the end of the section is preliminary sizing of chosen hooking mechanism. Hooking mechanism must ensure lander equilibrium under displacement conditions, so as a starting point we will consider fixed support reaction yielded in previous load analysis to be balanced by hooking mechanism.

To ensure shoreline connection we consider two different hooking mechanism, one is purely mechanic and exploits microspines technology while the other one is based on suction cup technology, which exploit pressure difference acting on suction cup surface to obtain connection with costal rocks. In both cases our aim is to determine minimum dimension of hooking mechanism capable of ensuring stabilization with one arm alone, in order to be able to face an unexpected failure of other robotic arm.

5.1 Solution A

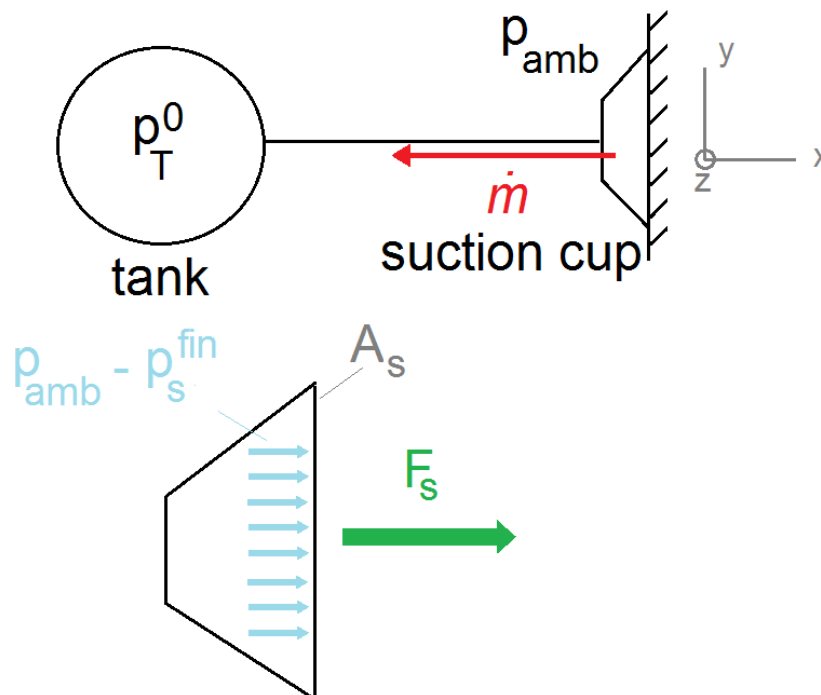


Fig. 44. Proposed suction cup hooking mechanism working principle.

Fig. 44 shows schematic representation of suction cup working principle. Proposed suction cup system to ensure shoreline hooking is constituted by a spherical tank connected by a pipe to a set of suction cups, low pressure tank ensure pressure difference which ensure surface adhesion. Suction cup number will be determined later in the section.

Set of values used for suction cup analysis has been defined in Table 20,

p_s^{in}	Initial pressure inside suction cup
p_s^{fin}	Final pressure inside suction cup
p_{eq}^{fin}	Equivalent final pressure inside suction cup
F_{eq}	Suction cup equivalent force
A_{eq}	Suction cup equivalent area
R_{eq}	Suction cup equivalent radius
p_T^0	Initial pressure inside tank
p_T^{fin}	Final pressure inside tank
N_s	Number of suction cups
V_s	Mean suction cup volume
T_s^o	Initial temperature inside suction cup
T_s^{fin}	Final temperature inside suction cup
T_T^o	Initial temperature inside tank
T_T^{fin}	Final temperature inside tank
A_p	Cross sectional area of pipe
V_T	Tank volume
R_T	Tank radius

Table 20. List of symbols used for suction cup-tank system sizing.

We set $p_s^{in} = p_{amb} = 152000 Pa$ and $T_s^o = T_T^o = -180^\circ C$, that are known values of Titan environment. In first approximation, in place of a set of suction cups, an equivalent suction cup alone has been considered. In this analysis, set of suction cups is considered to be placed inside equivalent suction cup area in order to obtain the maximum allowable density, and then smaller dimension. We assume suction cup to have base circular area. It has been found [1] that highest circles density inscribed inside a larger circle is obtained for 7 or 19.

Visualization of this assumption is shown in Fig. 45.

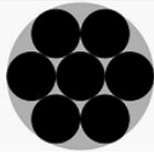
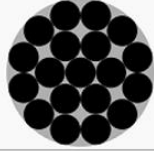
Number of unit circles	Enclosing >circle radius	Density	Optimality	Diagram
7	3	0.7778...	Trivially optimal.	
19	$1 + \sqrt{2} + \sqrt{6} \approx 4.863...$	0.8034...	Proved optimal by Fodor in 1999.	

Fig. 45. Surface circular package [1]

We then start our analysis from equivalent quantities and later we will on determine actual suction cup size.

Once suction cup get in contact with rock surface, pressure inside suction cup is equal to external pressure, since no pressure difference has been applied yet. Inside the spherical tank a generic low pressure is present. When surface contact is obtained connection between suction cup and tank is opened and part of mass inside suction cup volume will be transferred to tank, that process will lead to a pressure decrease inside suction cup and thus pressure increase inside tank. Pressure difference between outside and inside volume of the suction cup will generate a force toward the wall that can be written as,

$$F_{eq} = A_{eq} \cdot (p_{amb} - p_{eq}^{in})$$

Also, normal force toward the wall make possible to develop a frictional force dependent on wall friction coefficient.

For suction cup system sizing we consider worst hooking configuration shown in Fig. 46, where bending moment has to be balanced by frictional force and not by normal suction cup force. Suction cup frictional force is clearly lower than normal force because is obtained scaling normal force by friction coefficient.

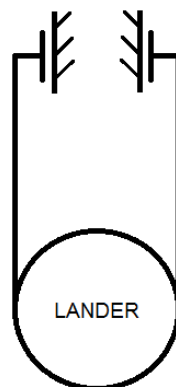


Fig. 46. Lateral hooking configuration.

Calculations we show below are referred to Fig. 47. With reference to FIG, we considered both external force and moment to be balanced by frictional force which by its definition does not have preferential direction, but it generally acts on wall surface plane. For calculations we assume suction cup centre of rotation to be located where shown in figure.

Equilibrium equations that must be satisfied here are,

$$F_y = F_x = \mu \cdot F_{eq}$$

$$M_z = 2 \cdot R_{eq} \cdot \mu \cdot F_{eq}$$

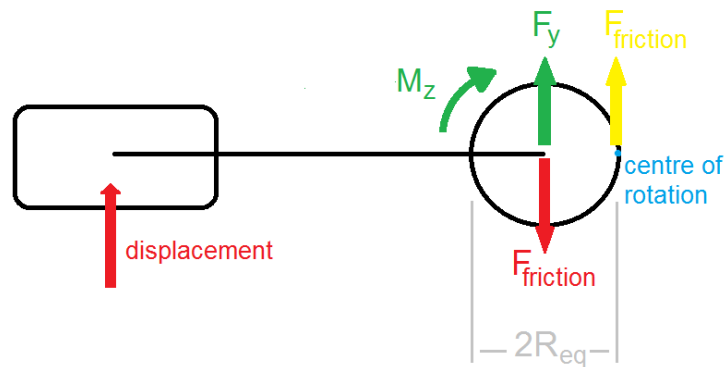


Fig. 47. Schematic representation of force and moment equilibrium for lateral hooking configuration.

Where $\mu = 0,1$ represents an estimation of friction coefficient of granite-like icy rocks on Titan [9]. Solving above expression for $M_z = 155 Nm$ and $F_y = 215 N$ (external loads founded in Section 3) we found out that the more restrictive conditions are the one imposed by bending moment. Fig. 48 shows plot of F_{eq} vs. R_{eq} for lateral hooking configuration that must balance external imposed moment. As expected from above equation a larger radius require a smaller force to balance rotational moment. It should be noted that even if a larger radius is desirable for equilibrium consideration, it raises dimension issue. We aim to find a compromise between these two design guidelines. Quantities considered are referred to equivalent suction cup as explained above.

Once equivalent suction cup quantities are known we can switch to actual suction cups quantities and then express single suction cup force (F_s) and radius (R_s) as,

$$F_s = \frac{F_{eq}}{N_s}$$

$$R_s = \frac{R_{eq}}{CR}$$

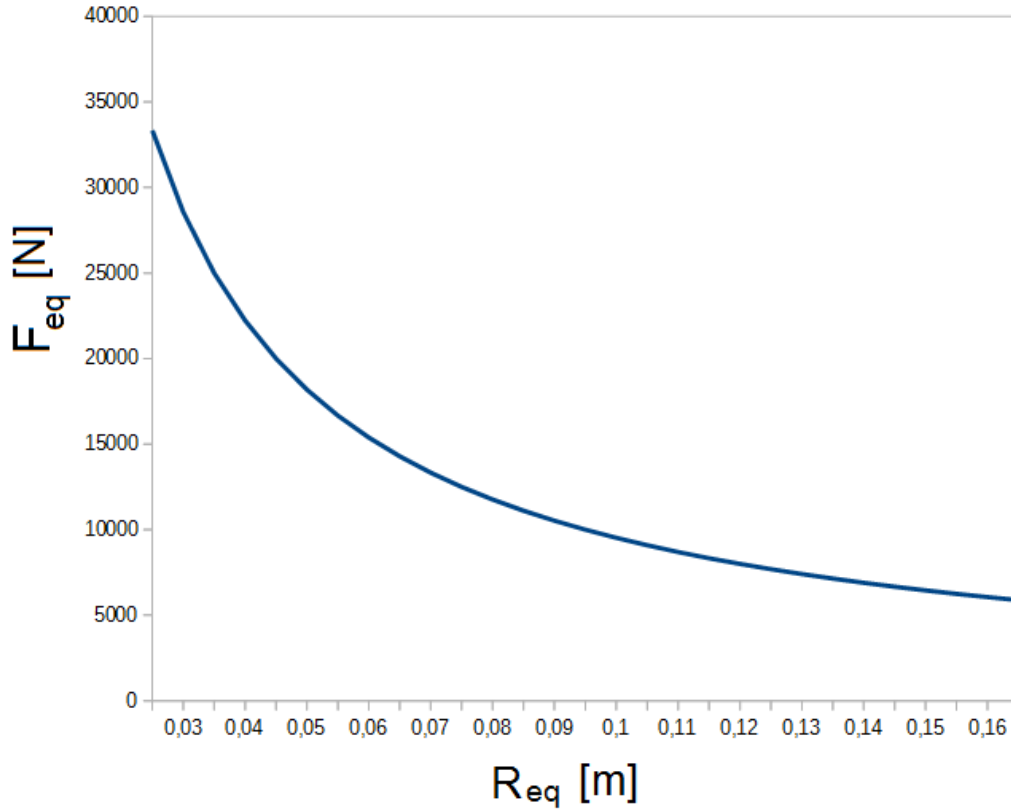


Fig. 48. F_{eq} vs R_{eq} to obtain external moment equilibrium.

Where N_s is number of suction cups placed inside equivalent area and CR is a parameter called circle radius dependent from N_s , shown in Fig. 45. It must be pointed out that not all yielded values of R_{eq} and F_{eq} produce acceptable results for F_s and R_s , because it must be verified that suction cup internal pressure at the end of mass transfer assume positive value, since negative pressure values have clearly no physical meaning. For each couple of F_s and R_s we then have to verify that,

$$p_s^{fin} = p_{amb} - \frac{F_s}{\pi \cdot R_s^2} > 0$$

Fig. 49 and 50 show yielded results for F_s . For sake of completeness we should note that also very low pressure value inside suction cup are not acceptable because of high demanding vacuum pump capabilities [10]. Making a conservative assumption on vacuum pump capability, we fixed minimum acceptable pressure value to be 10000 Pa.

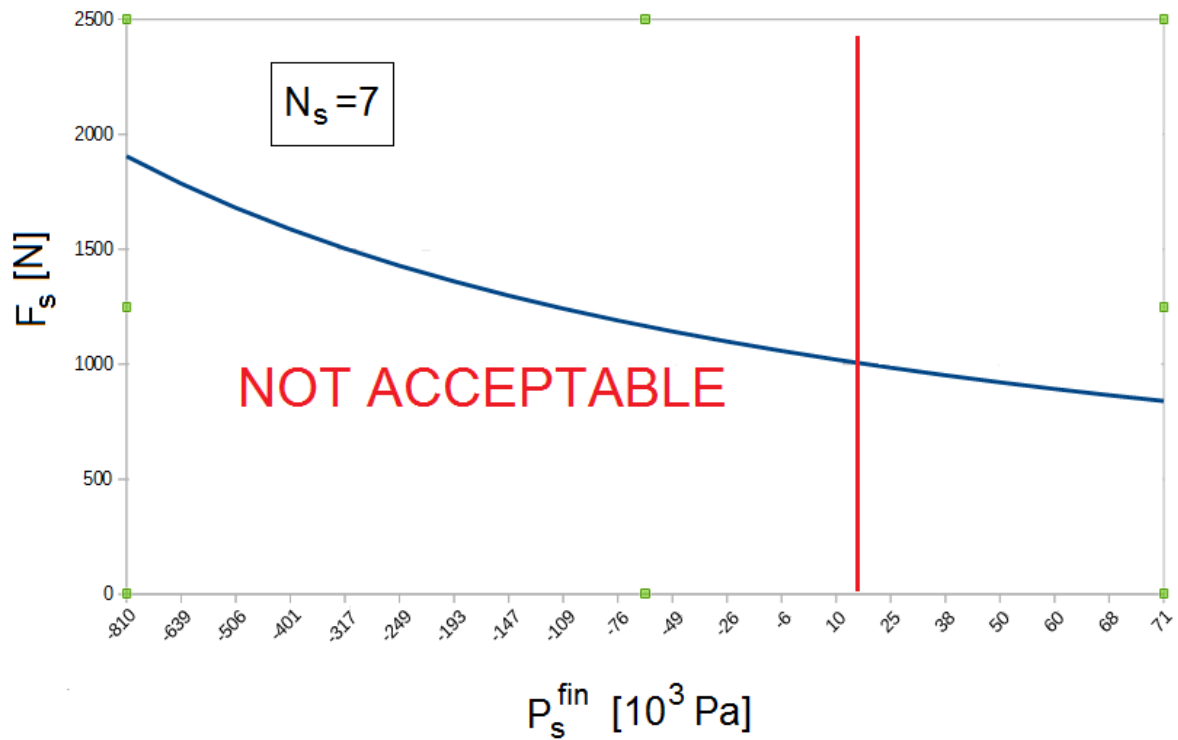


Fig. 49. Suction cup force vs suction cup final pressure plot. Plot made for 7 suction cups placed inside equivalent suction cup area. Lower pressure values correspond to higher adhesion force.

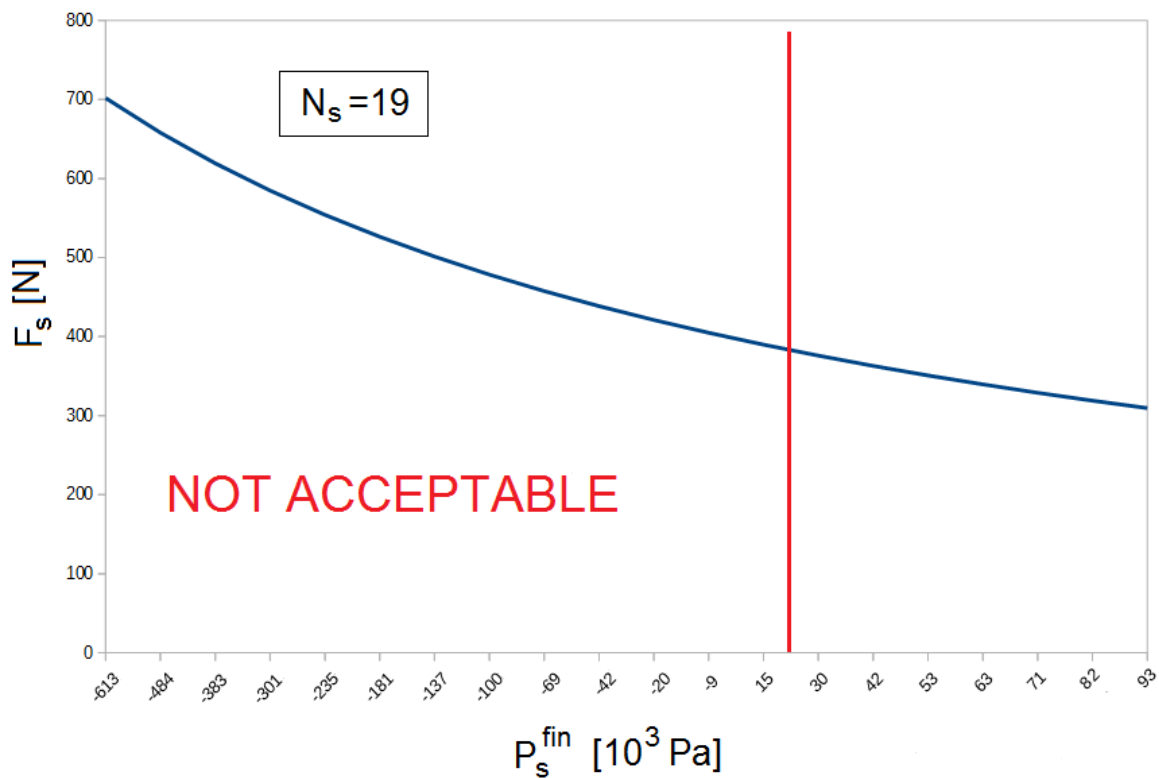


Fig. 50. Suction cup force vs suction cup final pressure plot. Plot made for 19 suction cups placed inside equivalent suction cup area. Lower pressure values correspond to higher adhesion force.

First valuable result for $N_s = 7$ results to be $p_s^{fin} \simeq 10778$ Pa and for $N_s = 19$ results to be $p_s^{fin} \simeq 15720$ Pa. From final pressure inside suction cup we can then determine lower

allowable values for suction cup equivalent radius. We found for both configuration $R_{eq} = 14 \text{ cm}$. Since circular packing is a mathematical model that does not take into account of physical properties of actual suction cup, e.g. thickness, connection mechanisms, etc., we consider yielded value of R_{eq} augmented of 20% and obtain $R_{eq} = 17 \text{ cm}$.

Table 21 summarize yielded results.

$R_{eq} = 17 \text{ cm}$	$N_s = 7$	$N_s = 19$
$R_s (\text{cm})$	4,6	2,8
$F_s (\text{N})$	1020	376
$p_s^{fin} (\text{Pa})$	10780	15720

Table 21. Values of suction cup radius, suction cup force and final pressure inside suction cup for $R_{eq} = 17 \text{ cm}$.

Clearly, Table 21 shows that the more the suction cup number the less the size of single suction cup. Smaller suction cups mean better adaptability to rocks unevenness. On the other hand, higher number of suction cups mean an increasing complexity of overall system, since there would be the need of more connections, valves and pipes, making overall system less reliable. For this reason in the continuation we consider number of suction cups to be 7 and then $R_s = 4,6 \text{ cm}$.

Now we have determined suction cups overall dimension, we can proceed with spherical tank sizing. It is important to note that tanks, one per arm, accommodate inside the lander structure and then they have to be more compact as possible.

For tank-suction cup thermodynamic analysis, we consider mass flow from suction cup to tank to be choked, condition ensured as long as ratio between pressure value inside suction cups and pressure value inside the tank is 2 or more [2]. Under choked condition we can write [2],

$$\dot{m} = \frac{p \cdot A}{\sqrt{\gamma RT}} \cdot \gamma \cdot \left(\frac{2}{\gamma + 1} \right)^{\frac{\gamma+1}{2(\gamma-1)}}$$

From mass continuity equation and considering the transformation to be isentropic, after some algebra we obtain [2],

$$t_{fin} = \left[\left(\frac{p_s^{fin}}{p_{amb}} \right)^{\frac{1-\gamma}{2\gamma}} - 1 \right] \frac{N_s \cdot V_s}{\sqrt{\gamma RT_s^0}} \frac{2}{\gamma - 1} \left(\frac{2}{\gamma + 1} \right)^{\frac{\gamma+1}{2(\gamma-1)}}$$

This relation yields the time needed to reach suction cup final pressure with respect to suction cup initial pressure and volume.

Writing mass continuity equation for tank-suction cups system, and after some algebra we

can then relate final pressure in the tank, tank volume and tank initial pressure, with respect to time,

$$p_T^{fin} = p_T^0 \cdot \left\{ \rho_s^0 N_s V_s R \frac{T_T^0}{p_T^0 V_T} \cdot \left\{ 1 - \left[1 + A_p \sqrt{\gamma \frac{RT_T^0}{N_s V_s} \frac{\gamma-1}{2} \left(\frac{2}{\gamma+1} \right)^{\frac{\gamma+1}{2(\gamma-1)}} t_{fin}} \right]^{\frac{2}{1-\gamma}} \right\} + 1 \right\}^\gamma$$

Substitution of expression for t_{fin} in above equation yields,

$$p_T^{fin} = p_T^0 \cdot \left\{ \rho_s^0 N_s V_s R \frac{T_T^0}{p_T^0 V_T} \cdot \left\{ 1 - \left\{ 1 + A_p \sqrt{\gamma \frac{RT_T^0}{N_s V_s} \frac{\gamma-1}{2} \left(\frac{2}{\gamma+1} \right)^{\frac{\gamma+1}{2(\gamma-1)}} \left[\left(\frac{p_s^{fin}}{p_{amb}} \right)^{\frac{1-\gamma}{2\gamma}} - 1 \right] \frac{N_s V_s}{\sqrt{\gamma RT_s^0} \frac{2}{\gamma+1} \left(\frac{2}{\gamma+1} \right)^{\frac{\gamma+1}{2(\gamma-1)}} \right]^{\frac{2}{1-\gamma}} \right\} + 1 \right\}^\gamma$$

That relates tank final pressure, tank initial pressure, tank volume and suction cups final pressure.

In order to proceed with sizing analysis we have to make some assumptions about suction cups volume, tank volume and connection pipe cross sectional area. We consider suction cup as a truncated cone as shown in Fig. 51.

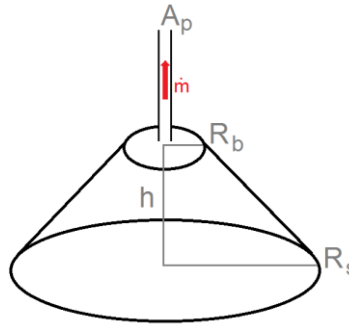


Fig. 51. Sketch of suction cup geometry.

We are able to determine suction cup volume once we fixed unknown quantities of Fig. 51. Setting $R_b = 1 \text{ cm}$ and $h = 1 \text{ cm}$ yields,

$$V_s = 2.8 \cdot 10^{-5} \text{ m}^3$$

We then assume that radius of pipe connecting suction cups and tanks is $r_p = 2.5 \text{ mm}$. That yields a cross section area $A_p = 0.0000196 \text{ m}^2$.

We now consider tank properties. We first note that tank volume value is connected to p_T^{fin} , if tank volume increase, p_T^{fin} will increase as well. It is appropriate to point out that increasing p_T^{fin} would cause p_s^{fin} to increase as well in order to maintain choked flow conditions. We then fixed R_T and p_s^{fin} to obtain reasonable value for p_T^{fin} .

Considering $p_s^{fin} = 10778 \text{ Pa}$ we found that minimum tank radius to obtain values of p_T^{fin} that ensure choked flow conditions is $R_T = 9 \text{ cm}$. It must be noted that lowering p_T^{fin} results in lowering p_T^0 that is initial tank pressure which must be reached in Earth

laboratories. In conclusion we should choose value of p_T^{fin} that ensure either choked flow condition or reasonable values of p_T^0 .

Fig. 52 shows plots of p_T^{fin} vs. p_T^0 , having fixed A_p , V_s and A_T as said before. From graph we can determine maximum value of p_T^{fin} which corresponds to higher possible p_T^0 . It has been determined $p_T^{fin} = 4650 Pa$ and $p_T^0 = 2000 Pa$. We see that, as required, flow choked condition is satisfied during the hole transformation process, since minimum ratio between suction cup pressure and tank pressure, i.e. at the end of transformation, is $\frac{p_s^{fin}}{p_T^{fin}} = 2,3$ that satisfy choked flow condition [2].

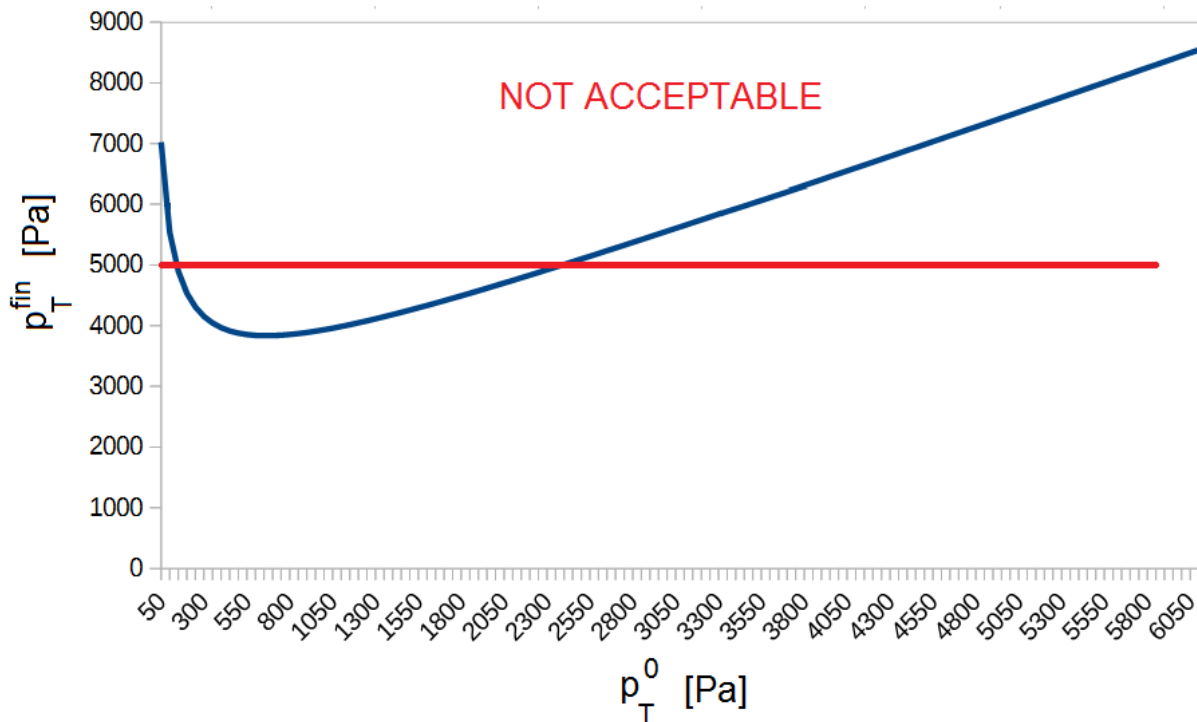


Fig. 52. p_T^{fin} vs. p_T^0 . Acceptable values for p_T^{fin} are highlighted.

From yielded values we can determine final temperature inside tank and suction cups with isentropic relation. That yields,

$$T_T^{fin} = -165^{\circ}C$$

$$T_s^{fin} = -225^{\circ}C$$

Up to now we have shown preliminary sizing of suction cup hooking mechanism, made of 7 suction cups per arm and one low pressure tank per arm. Calculations showed that suction cup mechanism overall dimension is $R_{eq} = 17cm$ and spherical tank radius is $R_T = 9cm$. Tanks have to be accommodated inside lander structure, clearly tank mass depends from thickness and material. Mechanical stress due to pressure increase inside tank structure as well as thermal stress resulted to be negligible. For preliminary mass estimation we selected a light material as aluminum and thickness of 1 mm, that yields a tank mass of 0,55 kg.

5.2 Solution B

This hooking solution is based on physical principle that allows insects to climb irregular surface. Insects indeed are able to climb vertical wall because of small (micrometer scale) spines presents under their feet, which can grip even really small asperities [3,4]. Microspines technology will be utilized for second hooking mechanism proposal.

As shown in Fig. 53 [4] microspines can be seen as curved beam of circular section which ends with a small tip radius (r_s).

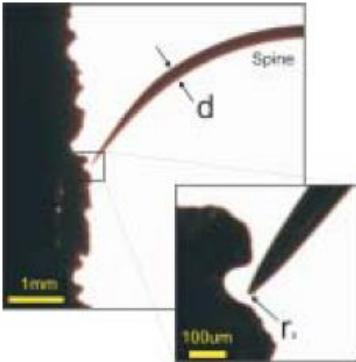


Fig. 53. Microspine geometry [4].

Accommodating microspines in a proper way at robotic arm end can ensure connection between lander and rocks [3,4]. Fig. 54 [4] shows interaction model between microspine and wall asperities on which presented hooking mechanism sizing is based.

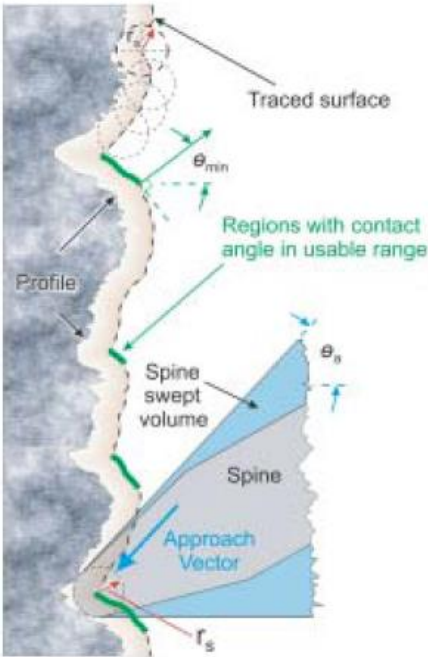


Fig. 54. Wall surface angle of attach [4].

Approach Vector shown in Fig. 54 represents the direction along which spine tip, approximated with circle of radius r_s , moves towards wall surface. *Approach Vector* is connected with angle θ_a as shown in Fig. 54. *Profiles* shown in Fig. 54 represent wall regions where angle between global horizontal vector and local surface normal vector is higher than a minimum angle θ_{min} . θ_{min} depends from spine load angle, θ_{load} (i.e. maximum angle at which spine can loaded away from the wall before it begins to slip off the asperity [4]), and wall surface friction coefficient as [4],

$$\theta_{min} = \theta_{load} + \text{arccot}(\mu)$$

Fig. 55 [4] shows evaluation of number of usable asperities per cm with respect to spine tip radius for various surface.

Surface Number	Surface	Average Roughness R_a (μm)	RMS Roughness R_q (μm)
1	cobblestone	56.9	78.1
2	machined granite	6.6	10.3
3	rough cut granite	42.7	56.1
4	polished granite	13.2	21.0
5	paving stone	73.0	92.2
6	concrete	93.0	131.9
7	cinderblock		
8	concrete 2	70.1	88.4
9	Al-oxide 80	42.1	57.0
10	Al-oxide 100	35.8	49.9
11	Al-oxide 120	20.3	26.0
12	Al-oxide 150	21.7	27.8
13	Painter's 100	30.5	38.9

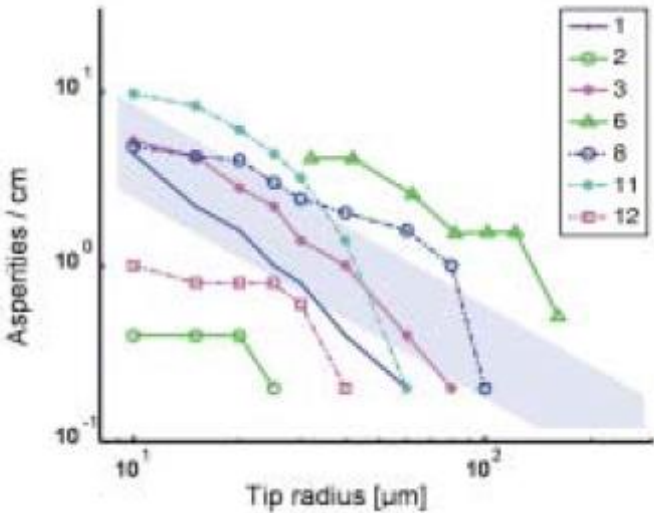


Fig. 55. Plot of usable asperities per centimeter length vs. spine tip radius for various surface material [4].

As shown in Fig. 55 number of usable asperities depends from surface roughness and exhibit a proportionality to $1/r_s$ [4]. Smaller spines tip radius likely find higher number of usable asperities with respect to larger spine tip radius, but they can sustain less load each [4].

Has been proved [4] that spines of tip radius between 15 and 20 micrometer and length of about 1,5 mm can exert a maximum spine-asperity force from 1 N to 2 N. From Fig. 55 it can be seen that spines of such dimensions are well suited for granite-like surface as expected to find on Titan.

For our hooking mechanism sizing, we based ourselves on JPL prototype microspine gripper [3]. We exploit a similar geometry to JPL grippers, but with some crucial difference mainly regarding actuation system that will be treated later in this section. Of course hooking mechanism dimensions will be adapted to our case; with respect to JPL microspine grippers our hand proposal will end up having different dimension and microspines number, quantities clearly connected to different problem nature with respect to JPL [3].

Since our aim is to have a microspine gripper capable of high adaptability to rock surface ($\propto 1/N_{toes}$) we supposed to model our gripper as a 12-toes hand ($N_{toes} = 12$), schematically shown in Fig. 56. Rectangle in Fig. 56 represents toe area filled with microspines, while central dodecagon represent arm-hooking mechanism interface. Number of toes represents a compromise between mechanism adaptability and overall dimension. Overall dimension can be reduced by lowering toes number, this results in larger toes capable of exerting higher force per toe. However, larger toe would have a lower adaptability to rock surface that represents an undesirable aspect. $N_{toes} = 12$ represent maximum allowable toes number which produce acceptable overall mechanism dimension constrained by thermal shield internal volume (for thermal shield interior arrangement see Section 8).

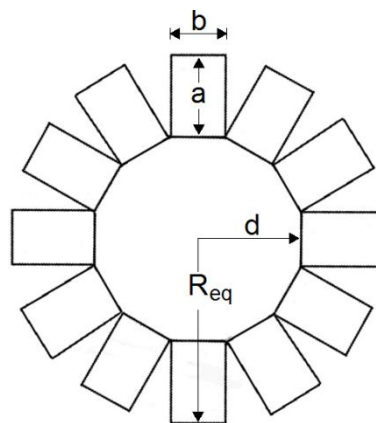


Fig. 56. Sketch of gripper geometry.

Where clearly,

$$R_{eq} = (d + a)$$

And surface of toe where microspines are present is yielded by $a \cdot b$.

For hooking mechanism sizing we considered that it is possible to break down spine-asperity force along directions of coordinate system related to toe as shown in Fig. 57.

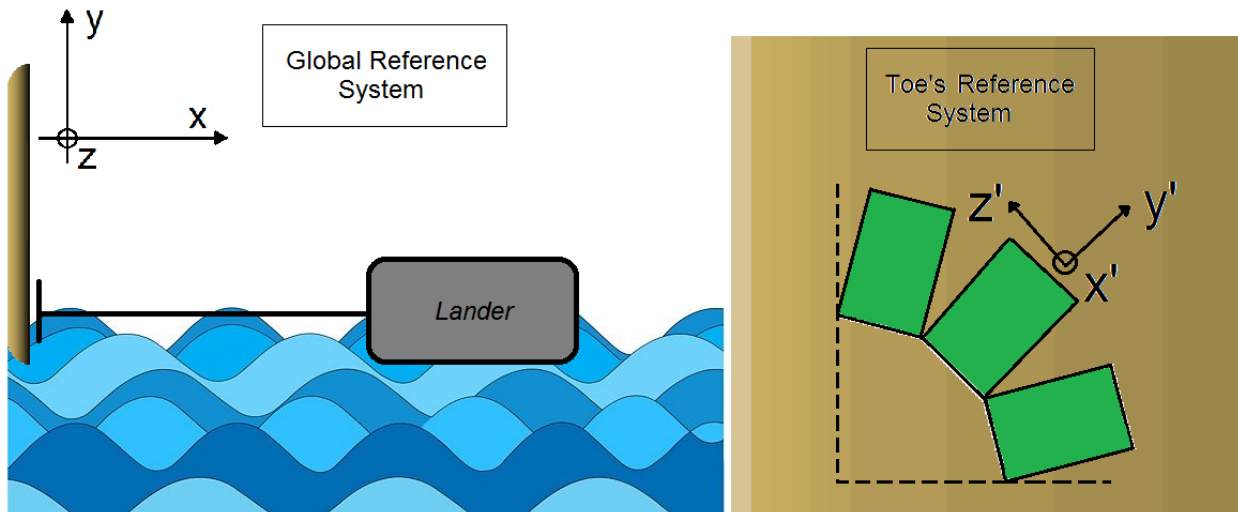


Fig. 57. Global reference system and toe's reference system.

We start from assumption that maximum spine-asperity force module is $|F_{sp}| = 1,5N$ [4]. From that we derived force components that can be exerted by spine-asperity contact. With reference to Fig. 57 we can write [3]:

$$F_{sp}^{x'} = 1N$$

$$F_{sp}^{y'} = 1,1N$$

$$F_{sp}^{z'} = 0,66N$$

That results to be a quite conservative assumption, since other works [3,4] consider microspine capable of generating omnidirectional force of 1,5 N, while for current discussion we thought about break down that force along coordinate system direction, resulting in low available force on each direction. In particular for $F_{sp}^{z'}$ we made the most sever assumption.

We can easily relate single spine-asperity force with toe force as,

$$F_{toe}^{x'} = F_{sp}^{x'} \cdot N_{sp}$$

$$F_{toe}^{y'} = F_{sp}^{y'} \cdot N_{sp}$$

$$F_{toe}^{z'} = F_{sp}^{z'} \cdot N_{sp}$$

Where N_{sp} is number of spine per foot, clearly we can then write,

$$\vec{F}_{toe} = (F_{toe}^{x'}; F_{toe}^{y'}; F_{toe}^{z'})$$

Because of irregular surface connection, it is appropriate to think [3,4] than only 30% of total toe microspine results to be engaged with rock asperities.

Quantity	Value/expression
d	8 cm
b	4,3 cm
N_{toes}	12
N_{sp}	$\frac{a \cdot b}{h^2}$
M_z^{ext}	155 Nm
F_y^{ext}	215 N
F_x^{ext}	Negligible

Table 22. List of symbols and relative value of quantities used for microspine hooking mechanism sizing.

Table 22 summarize starting point from which we prosecute our sizing analysis of microspine gripper.

Where, as considered above, N_{sp} is spines number for each foot and h is the minimum distance between spines, we set $h = 2 \text{ mm}$ in order to have a good balance between spine density, that allows toe to be smaller and spine adaptability, ensured with larger spine distance [3]. Last three quantities listed in Table 22 are ones which must be balanced by microspines hooking mechanism to ensure global equilibrium.

5.2.1 Hooking configuration

We then consider two different hooking configuration, one shown in Fig. 59 and one shown in Fig. 60, i.e. when microspine gripper is in frontal configuration of lateral configuration with respect to rocky surface. As shown below, we can separate vertical equilibrium from rotational equilibrium, since vertical equilibrium yields same results for both configurations. We present vertical equilibrium results valid for both configuration, while for rotation equilibrium we consider each case separately. All equilibrium consideration shown below has been done considering one arm connection, for sake of redundancy, as done with suction cup hooking mechanism.

Vertical equilibrium

Because of microspines shape (recall Fig. 53), we consider that only half of toes gripper are able to counteract vertical force. This results to be a conservative assumption since in [3] all toes are considered capable to participate to vertical equilibrium. Fig. 58 shows schematically what just said.

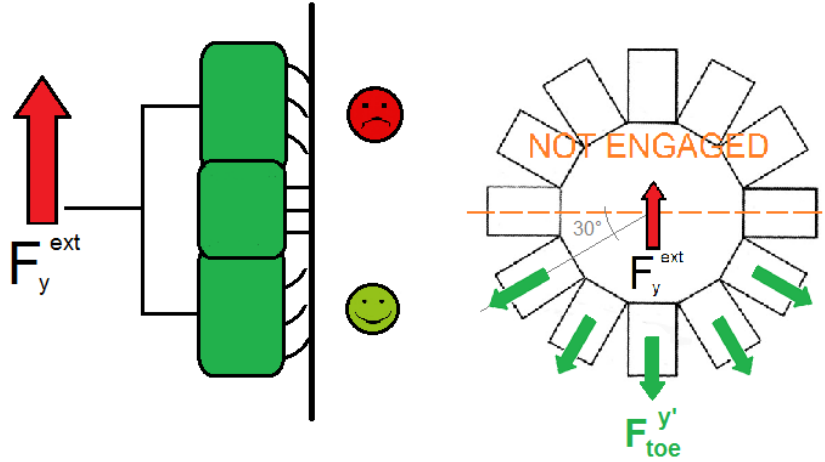


Fig. 58. Sketch of vertical equilibrium configuration. Toes exerted force to ensure equilibrium are highlighted.

From Fig. 58 we can write vertical force for each toe that participate to vertical equilibrium,

$$F_v = F_{toe}^{y'} \cdot \sin(\alpha)$$

So for configuration shown in Fig. 58 we can write vertical equilibrium equation as,

$$F_y^{ext} = F_{toe}^{y'} \cdot [1 + 2 \cdot \sin(30^\circ) + 2 \cdot \sin(60^\circ)]$$

With reference to F_y^{ext} value plotted in Table 22 we obtain,

$$F_{toe}^{y'} = 57 \text{ N}$$

And,

$$a \cong 0,005 \text{ m}$$

Rotational equilibrium

As said above rotational equilibrium will be treated separately for two different hooking configuration

Frontal hooking

Fig. 59 shows problem schematic representation. We consider that M_z^{ext} can be balanced by toe out-of-plane force (x' direction with reference to Fig. 57) applied at half of total toe length. From Fig. 59 we see that lateral toe do not participate to rotational equilibrium for this configuration. We can then write equation that must be satisfied to ensure rotational equilibrium as,

$$M_z^{ext} = 2 \cdot F_{toe}^{x'} \cdot [1 + 2 \cdot \sin(30^\circ) + 2 \cdot \sin(60^\circ)] \cdot (d + a/2)$$

Recalling above expressions for $F_{toe}^{x'}$ and N_{sp} we can write,

$$F_{toe}^{x'} = C \cdot \frac{ab}{h^2}$$

Where we set $C = 0,3$ because, as said before, only 30% of toe's spines are engaged. Substitution of above expression in rotational equilibrium expression yields a second order equation in a that can be written as,

$$a^2 + 2ad - \frac{M_z^{ext} \cdot h^2}{C \cdot b \cdot [1 + 2 \cdot \sin(30^\circ) + 2 \cdot \sin(60^\circ)]} = 0$$

That yields two value of a of which only the positive one has physical meaning for our problem. With reference to M_z^{ext} , b , d and h values plotted in Table 22 we obtain,

$$a \cong 0,045 \text{ m}$$

And,

$$F_{toe}^{x'} = 145 \text{ N}$$

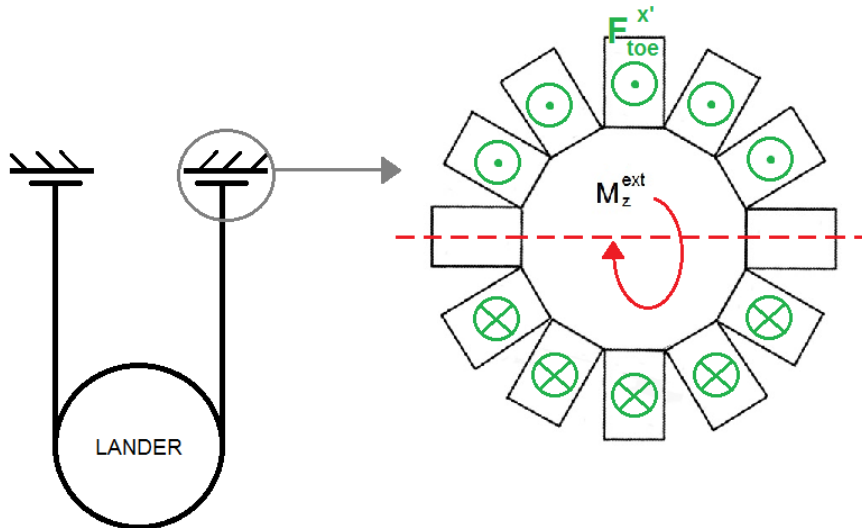


Fig. 59. Rotational equilibrium for frontal hooking configuration. Toes exerted force to ensure equilibrium are highlighted.

Lateral hooking

Fig. 60 shows problem schematic representation. We consider that M_z^{ext} can be balanced by toe force along z' direction (with reference to Fig. 57) applied at half of total toe length as before. From Fig. 60 we see that each toe does participate to rotational equilibrium for this configuration. We can then write equation that must be satisfied to ensure rotational equilibrium as,

$$M_z^{ext} = F_{toe}^{z'} \cdot N_{toe} \cdot (d + a/2)$$

As before, recalling above expressions for $F_{toe}^{z'}$ and N_{sp} we can write,

$$F_{toe}^{z'} = C \cdot 0,66 \cdot \frac{ab}{h^2}$$

Same assumption as before stays for C and again, substitution of above expression in rotational equilibrium expression yields a second order equation in a that can be written as,

$$a^2 + 2ad - \frac{2 \cdot M_z^{ext} \cdot h^2}{Cb \cdot 0,66 \cdot N_{toe}} = 0$$

That yields two value of a of which only the positive one has physical meaning for our problem. With reference to M_z^{ext} , b , d and h values plotted in Table 22 we obtain,

$$a \cong 0,045 \text{ m}$$

And,

$$F_{toe}^{z'} = 95 \text{ N}$$

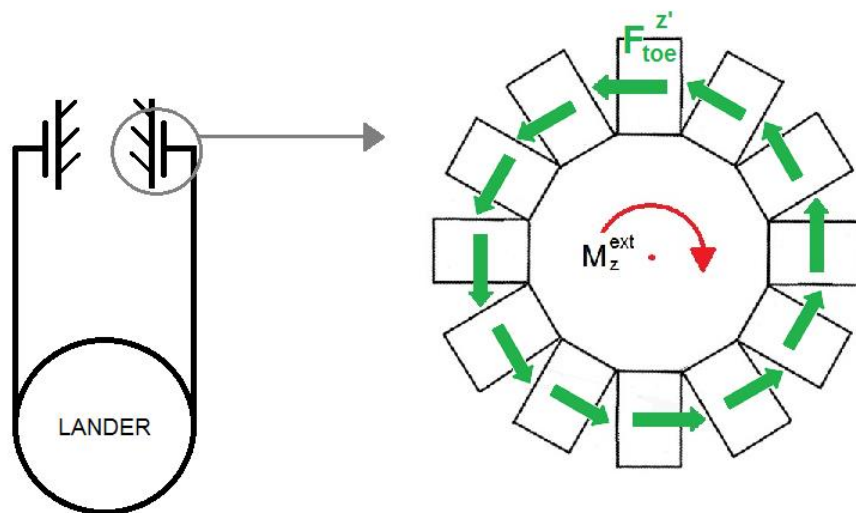


Fig. 60. Rotational equilibrium for lateral hooking configuration. Toes exerted force to ensure equilibrium are highlighted.

5.2.2 Results discussion

Table 23 shows yielded values of toe length where microspines are present found for three cases shown above.

Quantity to be balanced	Toe length (where spines are present)
F_y^{ext}	$a = 5 \text{ mm}$
M_z^{ext} (frontal hooking)	$a = 45 \text{ mm}$
M_z^{ext} (lateral hooking)	$a = 45 \text{ mm}$

Table 23. Toe length relative to each equilibrium condition.

To ensure global equilibrium in every possible hooking configuration, we have to assume worst hooking cases that yields $a = 45 \text{ mm}$ and thus, $R_{eq} = 12,5 \text{ cm}$. As done for suction cup system we augmented R_{eq} found value of 20% in order to account for actual structure not taken into consideration by mathematical model, that yields $R_{eq} = 15 \text{ cm}$.

As discussed above, directional spine force are related to each other, because they have to satisfy condition that spine force module is of 1,5 N. Then, considering worst hooking scenario we determined maximum directional force exerted by microspines foot to be,

$$F_{toe}^{x'} = 145 \text{ N}$$

$$F_{toe}^{y'} = 160 \text{ N}$$

$$F_{toe}^{z'} = 95 \text{ N}$$

From here we are able to determine number of spines per toe, considering that only 30% of spines get engaged with rock asperities. That yields,

$$N_s \cong 500$$

5.3 Solutions comparison

Now we determined preliminary dimension we can make comparison between two different hooking solutions. Table 24 summarize pros and cons for each solution. We assigned marks for most important issues about hooking mechanism. At the end of the table overall mark is shown, which allows to choose more suited solution.

	<i>Percentage weight</i>	<i>Solution A</i>	<i>Mark</i>	<i>Solution B</i>	<i>Mark</i>
<i>System components</i>	15%	Suction cups, tanks, pipes, valves	2	Microspines, toes, actuation mechanism	3
<i>Hooking mechanism dimension</i>	15%	$R_{eq} = 17 \text{ cm}$	3	$R_{eq} = 15 \text{ cm}$	5
<i>Reliability</i>	30%	Prototype, not tested	3	Existing system, tested	4
<i>Adaptability</i>	30%	Suction cups dimension not suited for uneven surface	2	Well suited for rocky surface	5
<i>Improvement margin</i>	10%	Lowering suction cups dimension	4	Spines adaptability	2
<i>Final mark</i>			2,65		4,1

Table 24. Solution trade off analysis.

From Table 24 we chose solution B.

Now that solution B has been chosen, we can proceed with description and sizing of toe actuation mechanism.

5.4 Actuation mechanism architecture

We now give a general description of toe actuation mechanism. Fig 61 shows schematic sketch of proposed mechanism for toe motion. All subsequent considerations are referred to Fig. 61.

Fig. 61 shows toe in engaged position, thus when microspines are fixed to rocky surface. As shown in figure, toe motion is ensured by worm drive-spur gear connection, where worm drive is connected to servo motor. It can be seen from figure that toe is made of two separated parts, tip part (microspines support) is the one with microspines, while other one is connected to sticks which transmit motion to entire toe. Prismatic joints between two parts are needed because they can ensure better probability of spine-asperity adhesion [4]. Elastic element 1 is needed to limit that displacement in order to prevent separation of toe's parts. Elastic element 2 is used either for helping spines engagement or for maintaining proper toe rest position (see below for details).

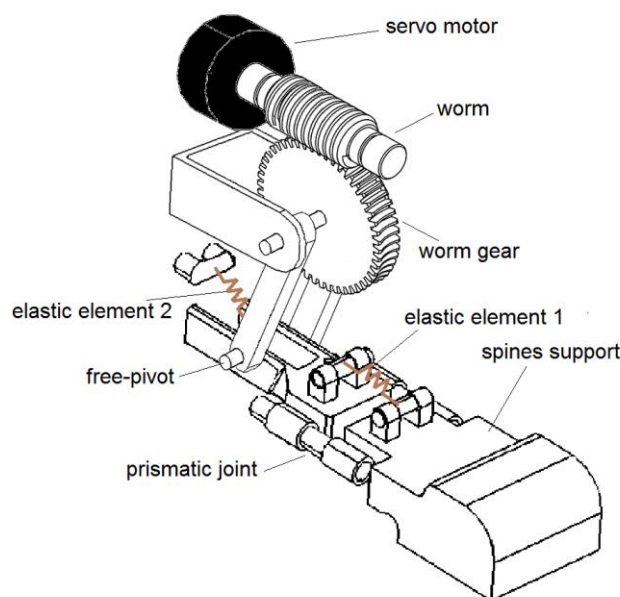


Fig. 61. Sketch of toe actuation mechanism components.

Now we gave generalities about toe mechanism, we can see in detail toe allowable motion.

Fig. 62 shows toe rest position, that also results to be rock approach position. As we can see, at rest position, elastic element tension is maximum, in order to ensure toe stability that otherwise would be able to rotate about the free pivot.

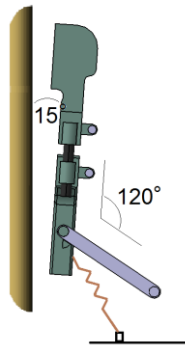


Fig. 62. Toe rest/wall approach position.

Fig. 63 shows rock engagement movement. Starting from rest position shown in Fig. 62, worm drive mechanism, activated by servo motor, impose rotation to toe-stick connection and thus to toe itself. During this rotation elastic element tension gradually decrease and became zero when engagement is obtained [4]. Elastic element help engagement of microspines because of little normal force toward rock surface applied at toe's tip [4].

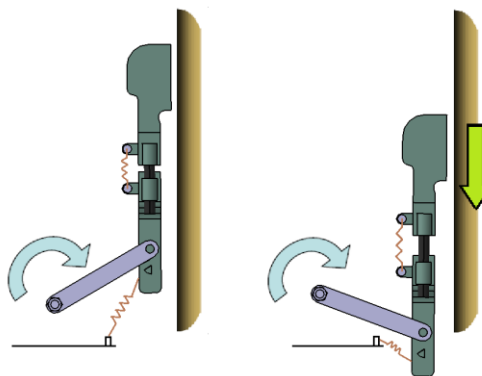


Fig. 63. Toe wall adhesion engagement movement.

In the case that first engagement attempt fails, there is the need of reacquisition of rest position in order to make a second engagement attempt. Exchanging rotational direction of servo motor makes possible to return to rest position, as shown in Fig. 64. As seen from Fig. 64, tension in elastic element increase during wall separation and ensure toe proper orientation at rest position [4].

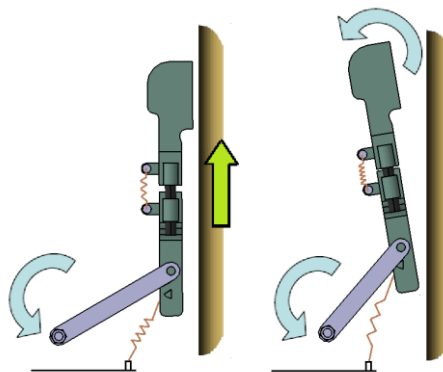


Fig. 64. Toe wall disengagement movement and return to rest position.

5.5 Final configuration

Now that preliminary sizing of microspine grippers and toe actuation mechanism have been shown, we can present final proposed configuration for microspine gripper. We present also proposal of interface that connects microspine gripper hand with spherical wrist of robotic arm. Interface design has been performed in order to ensure light weight but enough stiffness to support load conditions. Before choosing final interface configuration we tried other lighter solution, but they have been discarded because of failure occurrence under load conditions. Final configuration is show in Fig. 65.

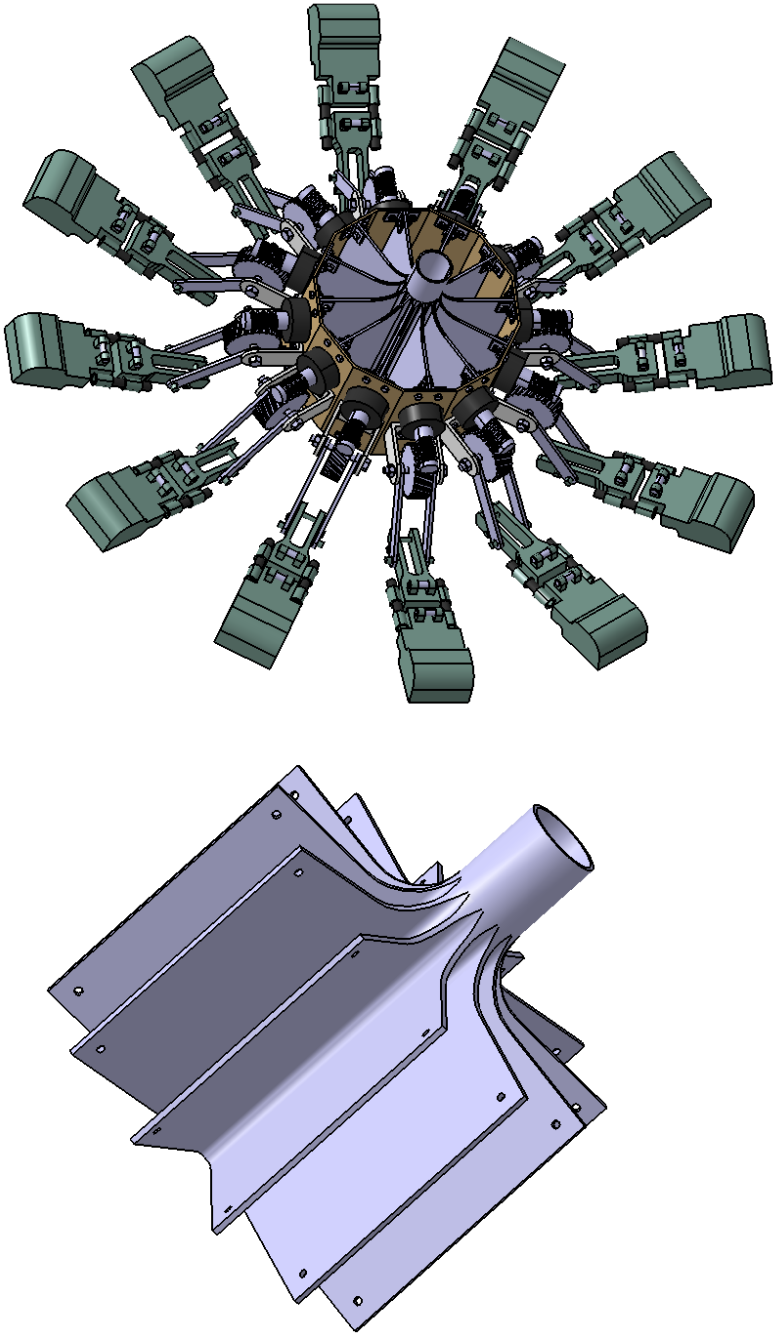


Fig. 65. Hand gripper rest position final configuration and hand gripper interface.

As we can see from Fig. 65 proposed interface is made of one piece alone and no joint structure has been added in order to make the overall system as integrated as possible.

Following this design guideline we placed servo motors directly on toes central support. As shown in Fig. 65 each toe mechanism is related to dedicated servo motor. One can think that having one servo motor per finger is not an appropriate choice, because of system complexity and also because other similar robotic tools has been done before with a single central actuator for all toes [3]. It is then appropriate to note that toe dedicated servo motor ensure toe independence from other toes and then capability of hooking disregarding of other toes rock connections. Considering single central actuator, this results to be well suited for static problem, when proper approach to surface is ensured with high precision and then it is possible for all toes to hook together with a single movement. Our problem cannot be considered as static, since waves and then disturbances are present, so it is possible that some toes acquire adhesion at first tentative, while other ones should try twice or more before getting proper connections, this clearly cannot be done with a single central actuator.

5.6 Actuation mechanism loads

With reference with exposed sizing process, we can determine loads acting on each finger and then loads acting on toe support and actuation mechanism. We split toes loads in two different cases, frontal and lateral hooking, as be done for loads determination.

Frontal hooking

Fig. 66 shows maximum loaded finger for frontal hooking configuration. Finger represented here is top finger with reference to Fig. 59. From geometric considerations, we were able to determine $\theta = 65 \text{ deg}$. Besides, $s = 0,05 \text{ m}$.

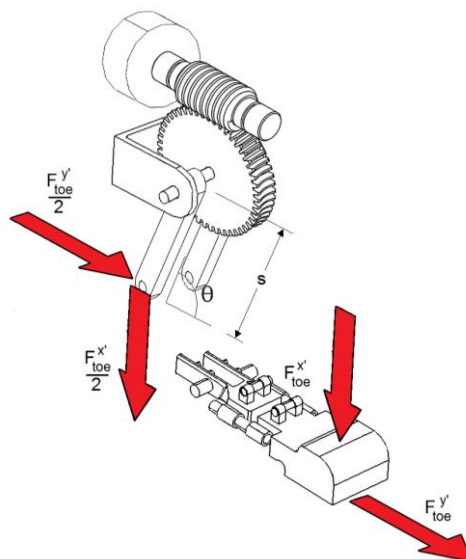


Fig. 66. Frontal hooking toe mechanism forces distribution.

From figure we can see that $F_{toe}^{x'}$ and $F_{toe}^{y'}$ act directly on connection sticks and then on top pivot-plate connection. They also generate a torque that must be balanced by worm drive connection that can be express as,

$$M = s \cdot \left[F_{toe}^{y'} \cdot \sin(\theta) + F_{toe}^{x'} \cdot \cos(\theta) \right] = 6 \text{ Nm}$$

Lateral hooking

As discussed in loads determination section, for lateral hooking configuration all fingers are equally loaded. Fig. 67 shows loads acting on finger for lateral hooking configuration.

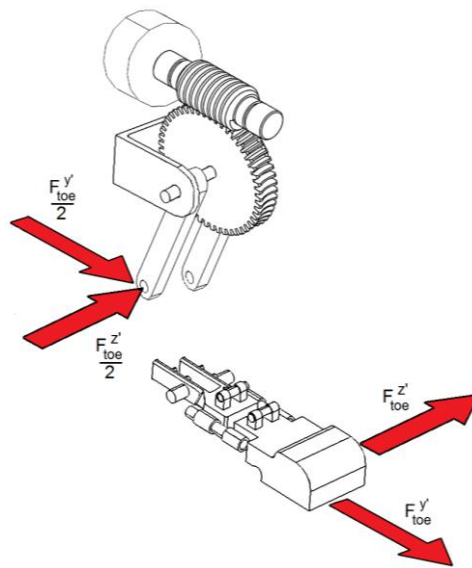


Fig. 67. Lateral hooking toe mechanism forces distribution.

Where, as before, $F_{toe}^{z'}$ and $F_{toe}^{y'}$ act directly on connection sticks and then on top pivot-plate connection. Furthermore, $F_{toe}^{y'}$ generates a torque that must be balanced by worm drive connection that can be express as,

$$M = F_{toe}^{y'} \cdot s \cdot \sin(\theta) = 7,5 \text{ Nm}$$

Since moment acting on worm drive connection results to be higher for lateral hooking configuration, last yielded value will be used for preliminary worm drive-spur gear sizing, shown below.

Spur gear-worm drive preliminary sizing

As discussed previously in this section, mechanism which transfer motion from servo motors to toe is constituted by a worm drive-worm gear coupling. Worm drive can transfer motion to worm gear, but under certain assumptions it is not possible that worm gear transfers motion to worm drive [6]. Of course this is valid until worm drive and worm gear resist under loading conditions.

In this section we will show some preliminary calculations about connection sizing. We consider for sake of simplicity spur gear to have straight teeth, that is clearly a preliminary assumption since actual spur gear will have helical teeth [6]. That preliminary sizing should be taken just as a guide line for future more precise sizing.

Since we chose that particular connection in order to ensure mechanism irreversibility, and then ensure complete locking once toes have reached desired configuration on rock surface, we start our analysis considering maximum stress we aim to obtain on spur gear single tooth once toe locking is obtained. We can write expression for bending stress acting on spur gear tooth [6],

$$\sigma = \frac{6M}{bt^2}$$

Where σ is tooth bending stress, M is bending moment acting on spur gear, b is spur gear width and t is tooth thickness. We fixed maximum allowable stress value to be 1000 MPa from fatigue consideration. We can then relate spur gear pitch diameter to known parameters. Substitution in previous equation of equivalent expression yields

$$d_g = N_g \cdot \sqrt[3]{\frac{M}{\sigma \cdot 2,25 \cdot K \cdot Y}}$$

Where d_g is spur gear pitch diameter, N_g is spur gear teeth number, M is bending moment, σ is tooth bending stress, Y is a constant related to teeth number derived from table [6] and K is a constant related to pitch diameter and teeth number [6]. For $K=10$, $N=29$ and $Y=0,35$, substitution in equation above of other known quantities of the problem yields $d = 3 \text{ cm}$. Furthermore, we consider for our analysis spur gear tooth angle to be 60 degrees and pressure angle to be 20 degrees since they are common values for these quantities [6], that yields $b = 1 \text{ cm}$ and $h = 0,2 \text{ cm}$.

Now we can proceed to worm drive sizing. We start from helical inclination angle, that for teeth pressure angle of 20 deg results to be $\lambda = 25 \text{ deg}$ [6]. We can write [5],

$$d_w = \frac{d_g}{N_g} N_w / \tan \lambda$$

Where d_w is worm drive pitch diameter, N_w is worm drive threads number. Since we aim a quite compact worm drive size, we fix $N_w = 4$. That yields $d_w = 1 \text{ cm}$ and total worm length of 1,5 cm [5].

Now we gave a preliminary size of worm drive-spur gear connection, we analyze motion transmission. Having fixed number of spur gear teeth and worm drive threads, we obtain a transmission ratio of 7,25 that is a quite low value for this connection type [6]. Since we

want to ensure irreversibility of mechanism we chose an efficiency value of 0,3 [6], from kinematic considerations we set torque to be developed by spur gear to rotate toe of 0,5 Nm. This leads to servo motor torque to be about 0,3 Nm. Setting servo motor working velocity to be about 500 rpm, we derive spur gear angular speed to be $\omega_g = 7 \text{ rad/s}$.

Spur gear angular speed results to be quite high, that is a desirable objective since motion of microspine toes should be preferable fast to ensure rapid engagement to rocky surface. It should then noticed that because of auto locking connection, servo motor works only for a small time interval, just to ensure toes engagement to rough surface. Possible future development of treated connection will be discussed in Section 10.

5.7 Manufacturing generalities

Here we spend a few words about foot manufacturing process which comprehends also spines application. Since spines are of micrometre dimensions ($d \cong 200\mu\text{m}$) process of assembling spines with other toe parts can be seen as quite complex. The process to produce microspines toe is called Shape Deposition Mechanism [3,4,7,8] and represents a Rapid Prototyping technology that can make possible hard material and soft material to be simultaneously fabricated and assembled [3,7]. Spines of micrometric dimensions are embedded directly into hard toe material (e.g. hard urethane) during SDM process [3]. For more information about SDM process see [7,8].

References

- [1] https://en.wikipedia.org/wiki/Circle_packing_in_a_circle. Last access on November 2015.
- [2] CURRIE, Iain G. *Fundamental mechanics of fluids*. CRC Press, 2012.
- [3] PARNES, Aaron. Anchoring foot mechanisms for sampling and mobility in microgravity. In: *Robotics and Automation (ICRA), 2011 IEEE International Conference on*. IEEE, 2011. p. 6596-6599.
- [4] ASBECK, Alan T., et al. Scaling hard vertical surfaces with compliant microspine arrays. *The International Journal of Robotics Research*, 2006, 25.12: 1165-1179.
- [5] <http://www.ctmeca.com/docFichesTechniques/IngranaggiDiPrecisione.pdf>. Last access November 2015
- [6] JUVINALL, Robert C.; MARSHEK, Kurt M. *Fundamentals of machine component design*. New York: John Wiley & Sons, 2006.
- [7] <http://www-cdr.stanford.edu/biomimetics/sdm.html>. Last access on November 2015.
- [8] WEISS, Lee; SCHULTZ, L.; MILLER, E. Shape deposition manufacturing. In: *Proceedings of Solid Freeform Fabrication Symposium*. Austin: The University of Texas, 1994.
- [9] http://www.engineeringtoolbox.com/friction-coefficients-d_778.html. Last access on November 2015. rotational
- [10] https://en.wikipedia.org/wiki/Vacuum_pump. Last access on November 2015.

6 Fatigue verification

6.1 Model description

With reference to external loads defined in Section 3, it has been possible to single out critical zone for fatigue verification using Ansys Workbench® software.

Table 25 summarizes some of possible hooking configurations that can be encountered during mission development. For these configuration, two critical components of microspine grippers have been identified and analyzed. With reference to Table 25, A_{wave} is wave amplitude, T_{wave} is wave period, λ_{wave} is wave wavelength and δ is lander imposed displacement. We make an estimation of percentage of total mission duration associated to each configuration and relative number of cycles. For each selected wave amplitude we consider two different possible hooking configuration, former one when hooking manoeuvre is performed at crest/pit of the wave and latter one when hooking manoeuvre is performed at zero-amplitude point.

A_{wave}	T_{wave}	λ_{wave}	% of mission	n°of cycles	Description	δ
10 cm	2,5 s	1,4 m	20%	576	Crest/pit hooking	-20 cm (+20 cm)
					Zero-amplitude hooking	± 10 cm
5 cm	1,8 s	0,7 m	40%	1600	Crest/pit hooking	-10 cm (+10 cm)
					Zero-amplitude hooking	± 5 cm
2,5 cm	1,27 s	0,35 m	40%	2300	Crest/pit hooking	-5 cm (+5 cm)
					Zero-amplitude hooking	$\pm 2,5$ cm

Table 25. Details for different hooking heights and configurations

Typical load cycles for horizontal and lateral hooking (see Section 5 for details) are shown in Table 26.

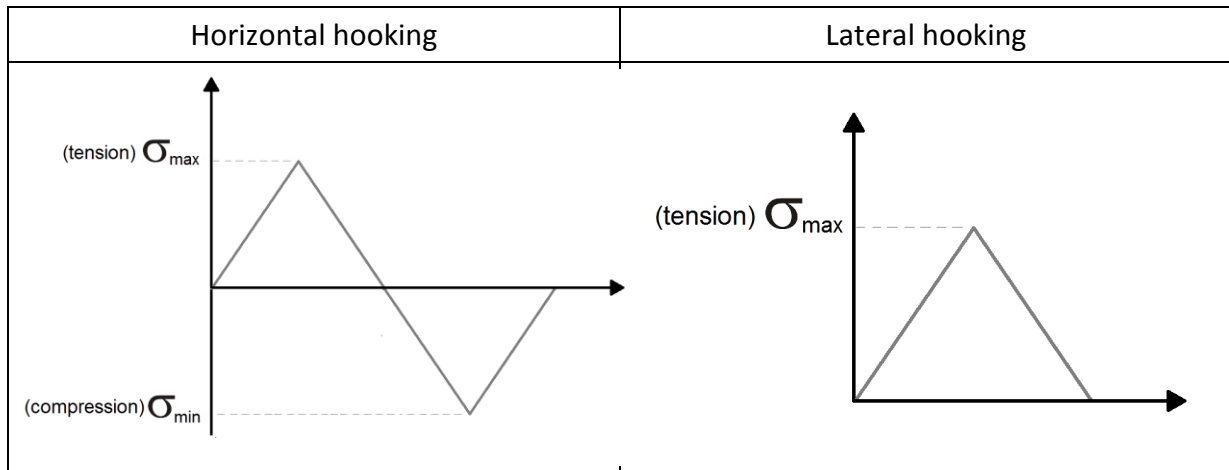


Table 26. Typical load cycles from stress point of view for different hooking configurations.

6.2 Critical components analysis

Critical components that have been analyzed under fatigue conditions are gripper/arm interface and toe connection stick (see Section 5 for details). For loads intensity and direction see Section 3 for interface loads and Section 5 for stick loads.

6.2.1 Interface

Selected material for interface is Titanium Ti-6Al-4V, see [1] for detailed properties.

Horizontal hooking

As shown in Table 25 we consider two different case for each wave amplitude, i.e. crest/pit hooking and zero-amplitude hooking.

Crest/pit hooking

Fig. 68 shows critical zone for considered component.

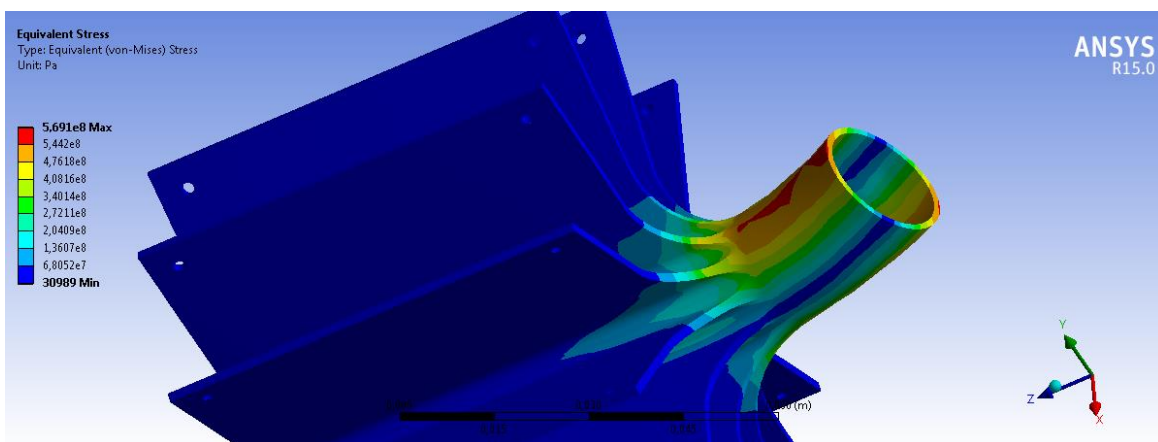


Fig. 68. Interface critical zone for horizontal hooking configuration.

Using fatigue curve of selected material [1], yielded results are summarized in Table 27.

	σ_{max} [MPa]	σ_{min} [MPa]	Damage
$\delta = 20$ cm	570	0	1 %
$\delta = 10$ cm	300	0	0 %
$\delta = 5$ cm	160	0	0 %
<i>Total damage after three lives</i>	3%		

Table 27. Interface maximum stress and total damage summary for horizontal hooking configuration. Results yielded for crest/pit hooking.

Zero-amplitude hooking

For zero-amplitude hooking we obtained a total damage of 0 %.

Lateral hooking

As done before, we consider two different case for each wave amplitude.

Crest/pit hooking

Fig. 69 shows that for this configuration two critical zones can be seen, one close to holes blade and one located on cylindrical surface.

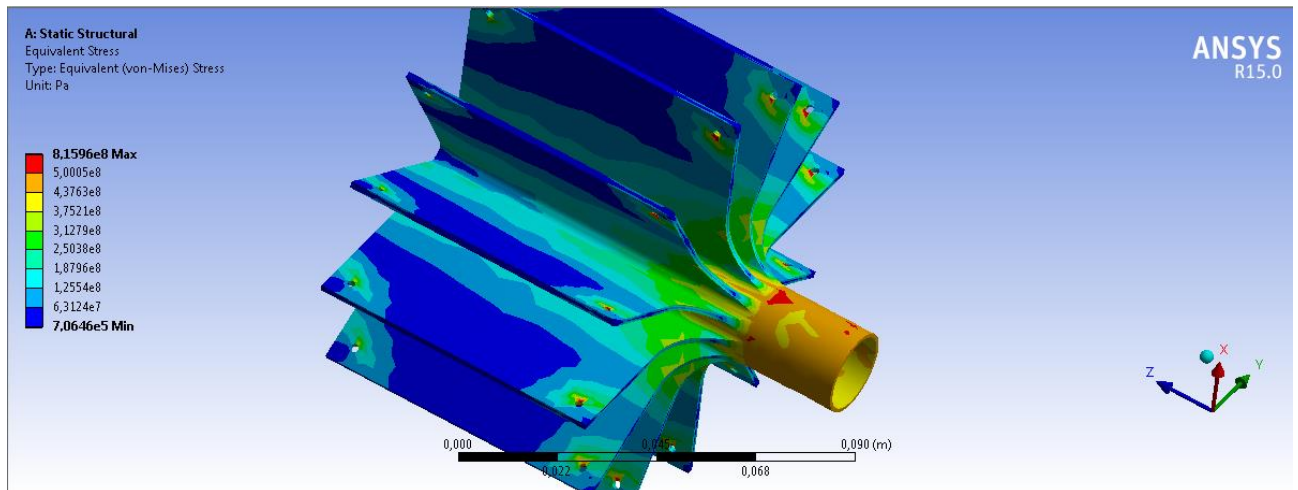


Fig. 69. Interface critical zone for lateral hooking configuration.

Blade hole

Since one critical zone is located near a hole, we applied for fatigue calculation a stress intensification factor $k_t = 2,8$, using fatigue curve of selected material [1], calculations yield results summarized in Table 28.

	σ_{max} [MPa]	σ_{min} [MPa]	Damage
$\delta= 20$ cm	815	0	26 %
$\delta= 10$ cm	485	0	3 %
$\delta= 5$ cm	300	0	0 %
Total damage after three lives	87 %		

Table 28. Blade hole maximum stress and total damage summary for lateral hooking configuration. Results yielded for crest/pit hooking.

Cylindrical surface

For cylindrical surface total damage results to be of 0 %

Zero-amplitude hooking

Blade hole

As before, we applied for fatigue calculation a stress intensification factor $k_t = 2,8$, besides, because of load pattern we apply $R = -1$ (see fatigue curve for detail). Using fatigue curve of selected material [1], calculations yield results summarized in Table 29.

	σ_{max} [MPa]	σ_{min} [MPa]	Damage
$\delta=\pm 10$ cm	485	485	18 %
$\delta=\pm 5$ cm	300	300	0 %
$\delta=\pm 2,5$ cm	185	185	0 %
Total damage after three lives	54 %		

Table 29. Blade hole maximum stress and total damage summary for lateral hooking configuration. Results yielded for zero-amplitude hooking.

Cylindrical surface

For cylindrical surface total damage results to be of 0 %

6.2.2 Toe stick

Selected material for interface is Steel 4130, see [1] for detailed properties.

Horizontal hooking

For both hooking configuration, horizontal hooking case yield a total damage of 0 %

Lateral hooking

As done before, we consider two different case for each wave amplitude.

Crest/pit hooking

Fig. 70 shows critical zone.

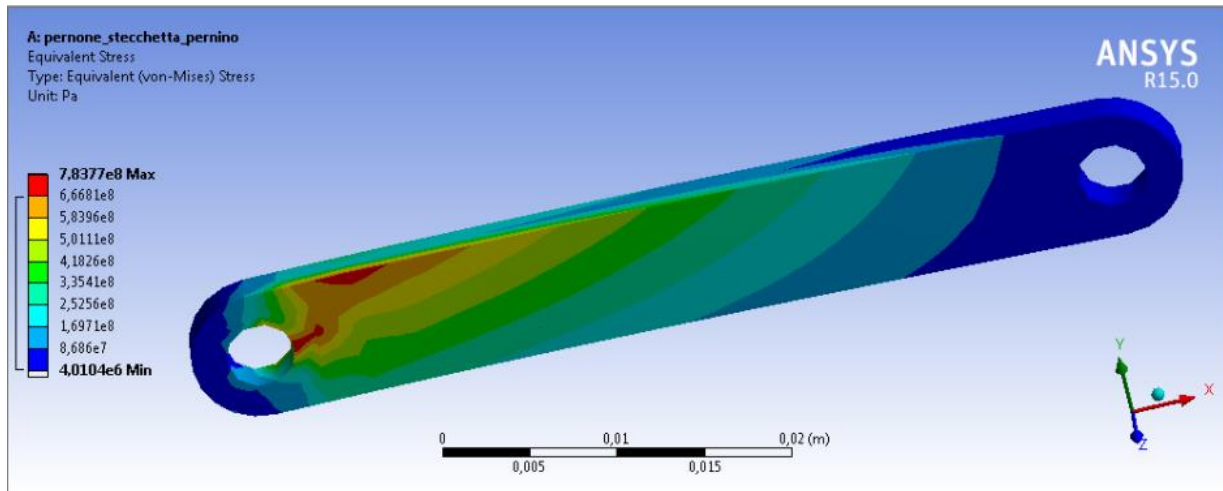


Fig. 70. Toe stick critical zone for lateral hooking configuration.

Since critical zone is located near a hole, we applied for fatigue calculation a stress intensification factor $k_t = 3$, using fatigue curve of selected material [1], calculations yield results summarized in Table 30.

	σ_{max} [MPa]	σ_{min} [MPa]	Damage
$\delta = 20$ cm	800	0	21 %
$\delta = 10$ cm	400	0	0 %
$\delta = 5$ cm	200	0	0 %
Total damage after three lives	63 %		

Table 30. Toe stick maximum stress and total damage summary for lateral hooking configuration. Results yielded for crest/pit hooking.

Zero-amplitude hooking

As before, we applied for fatigue calculation a stress intensification factor $k_t = 3$, besides, because of load pattern we apply $R = -1$ (see fatigue curve for detail). Using fatigue curve of selected material [1], calculations yield results summarized in Table 31.

	σ_{max} [MPa]	σ_{min} [MPa]	Damage
$\delta = \pm 10$ cm	400	400	4 %
$\delta = \pm 5$ cm	200	200	0 %
$\delta = \pm 2,5$ cm	100	100	0 %
Total damage after three lives	12 %		

Table 31. Toe stick maximum stress and total damage summary for lateral hooking configuration. Results yielded for zero-amplitude hooking.

6.3 Conclusions

It has then been proved that most critical components survive under fatigue conditions for three lives, as required from specification.

References

[1] HANDBOOK, Military. MIL-HDBK-5H: Metallic Materials and Elements for Aerospace Vehicle Structures. *Works of the US Department of Defense*, 1998.

7 Lander stability

Since the lander will spend its entire life operating in liquid methane environment, we had to consider perturbations induced to the lander by liquid methane motion. That problem has obviously numerous analogies with a ship sailing in liquid water and thus in the following part we make use of ships' stability theory to analyse lander response to perturbations.

7.1 Buoyancy

First of all we have to ensure buoyancy capability of the lander. Since TSSM report states [1] that proposed lander will have to be redesigned to ensure better buoyancy capability, in our calculation we determine the actual submerged volume needed to ensure buoyancy. For our calculations we consider:

- total lander mass (m_{TOT}) equal to 80 kg [1],
- liquid methane density at 90 K (ρ_{lCH_4}) equal to 450 kg/m³ [1],
- lander base radius (r) equal to 0,5 m [1],

From Archimedes' law of buoyancy we can write,

$$m_{TOT} = m_{dCH_4}$$

Where m_{dCH_4} stays for liquid methane displaced mass. That can be written as well,

$$m_{TOT} = \rho_{lCH_4} \cdot \pi \cdot r^2 \cdot t$$

Where t stays for submerged lander height. Substituting correspondent values, it yields,

$$t = \frac{m_{TOT}}{\rho_{lCH_4} \cdot \pi \cdot r^2} = \frac{80 \text{ kg}}{450 \frac{\text{kg}}{\text{m}^3} \cdot \pi \cdot (0,5 \text{ m})^2} = 0,23 \text{ m}$$

Then, considering a lander height outside liquid methane surface of 10 cm [1], that results in total lander height, $h_{TOT} = 0,33 \text{ m}$ (see Fig. 71).

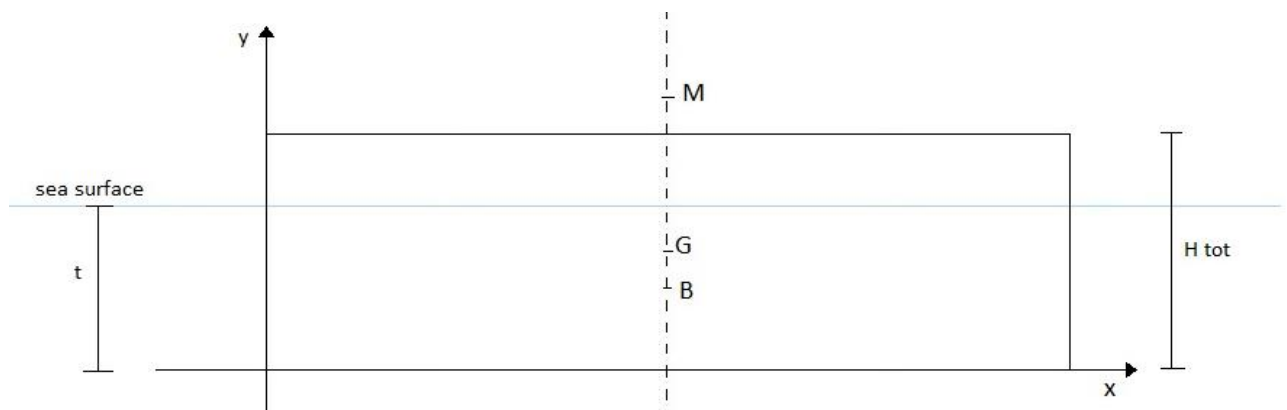


Fig. 71. Sketch of lander, with metacentric location (M), barycentre (G) and centre of buoyancy (B).

7.2 Metacentre and centre of buoyancy

In order to study lander response to perturbations, we need to determine positions of metacentre (M) and centre of buoyancy (B). Determination of B is quite straightforward since its definition is [3] the centre of mass of the fluid displaced by a floating or submerged body. Thus, centre of buoyancy depth from liquid methane surface results to be half of total submerged height, 0,115 m (see Fig. 71). Metacentre height can be determined from [3,4]

$$MB = \frac{I}{V_s}$$

Where MB is the distance from metacentre (M) to centre of buoyancy (B), I is moment of inertia of buoyancy figure with respect to its longitudinal barycentric axis and V_s is the submerged volume. Thus, we can write,

$$MB = \frac{\pi \cdot r^4}{4 \cdot \pi \cdot r^2 \cdot t} = 0,27 \text{ m}$$

Metacentre is then located 0,155 m above liquid methane surface (see Fig. 71).

7.3 Barycentre

Now that we have determined positions of buoyancy centre and metacentre, for the lander to be stable with respect to perturbations, it is necessary to ensure that lander's barycentre lies under M [1,3]. Barycentre position is important either for global stability, hence the capability to react to a perturbation in such a way that the lander returns to its initial equilibrium position, or for maximum allowable inclination angle, hence the angle beyond which the lander has its top surface partially beneath liquid methane surface. Since TSSM report states that the lander have to be redesigned [1], probably barycentre position they have determined will not match the actual barycentre position. Since it would be extremely complicated for us to determine precisely barycentre actual position, in our analysis we will follow TSSM report assumption, considering that barycentre lies at half total lander height [1]. Since our previous calculations yield a total lander height of 0,33 m we can conclude that barycentre vertical position is located 0,165 m above lander bottom surface (see Fig. 71). Besides, we think that is not incorrect to consider possible additional barycentre position lowering if necessary in subsequent mission phases.

Now we have fixed barycentre position and automatically ensured lander stability with respect to perturbations, as metacentric height results to be positive ($MG = 0,22 \text{ m}$), we can focus our attention to maximum allowable inclination angle. Since floating lander top surface is placed 10 cm above liquid methane surface [1] we will consider for our calculations maximum allowable vertical displacement of lander top surface related to rotation to be 10 cm .

From geometric considerations (Fig. 72) we can relate maximum tilting angle and maximum vertical displacement of lander upper surface. Thus, we can write

$$s_{MAX} = \frac{d}{\cos \alpha} + (r - d \cdot \tan \alpha) \cdot \sin \alpha - d$$

Where s_{MAX} is the maximum vertical displacement associated to tilting angle α , for a cylindrical lander of radius r and metacentric distance from lander top surface of d .

Solving for α yields,

$$\alpha_{1,2} = 2 \cdot \tan^{-1} \left(\frac{r \pm \sqrt{r^2 - s_{MAX}^2 - 2 \cdot d \cdot s_{MAX}}}{s_{MAX} + 2 \cdot d} \right)$$

Substituting,

- $s_{MAX} = 0,1 \text{ m}$
- $d = 0,052 \text{ m}$
- $r = 0,5 \text{ m}$

We obtain two different values of α ,

$$\alpha_1 \cong 11,7 \text{ deg}$$

$$\alpha_2 \cong 156,5 \text{ deg}$$

Where clearly only the first one (α_1) has reasonable meaning for our purpose.

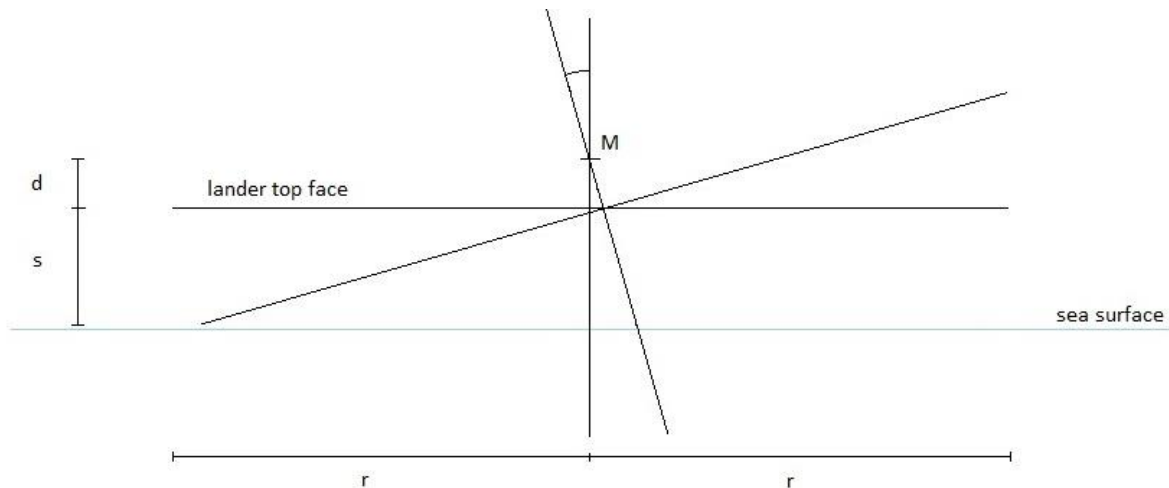


Fig. 72. Sketch of lander top face rotated of α towards sea surface. Metacentric height from lander top face is indicated with d , s stays for maximum lander top face vertical displacement and r stays for lander radius.

Metacentric theory includes two main approximations, one which consider metacentric height fixed with respect to floating object inclination angle and other one which consider metacentric height variable with floating object inclination angle, former one applies to small inclination angle while latter one applies for large inclination angle [3]. Inclination angle below 12 deg stays under constant metacentric height approximation, while for higher inclination angle it is appropriate to consider variable metacentric height [3]. Our maximum tilting angle value has been determined as α_1 and is close to boundary value which divides two metacentric approximations, but since we aim at maintaining tilting angle as low as possible, so possibly lower than α_1 , we consider constant metacentric height approximation.

7.4 Barycentre displacement

We now consider the case in which barycentre position will vary because of robotic arms deployment. Robotic arm deployment will be performed close to shoreline in order to be capable of making proper hooking manoeuvre. Arms motion will result in barycentre displacement from its original position (i.e. when both arms are folded).

Since TSSM lander was not designed to accommodate robotic arms on the top of it, simultaneous deployment of robotic arms result in high lander tilting which finally lead to capsizing. What we do in next section is to verify whether stable position is reachable considering one by one deployment. This assumption can be considered quite valid, since robotic arms have been design to be able to sustain structural load individually (see Section 5).

For subsequent calculations we consider two arm configurations, showed in Fig. 73

Fig. 73 shows a sketch of arms' folded configuration (A) and single arm deployment when in proximity of shoreline rocks (B). Configuration A is the folded configuration, i.e. at splash down and during drifting phase on lake's surface, while configuration B represents total deployment of arm 2, while arm 1 is still in folded configuration. Arms barycentre are shown in figure.

We can see that in configuration A overall arms barycentre (G) is located on lander's barycentric axis, yielding no net torque acting on lander itself and then no lander inclination occur. In configuration B we can see that arm 2 deployment results in shifting G_2 to G_2' with two displacement components, one vertical z -component and one horizontal x -component, while clearly G_1 and G_1' coincides since no movement have been performed by arm 1. G_2 displacement results in overall arms' barycentre displacement (G'), so in configuration B a net torque is acting on lander, causing inclination angle to appear. Clearly for Fig. B we can see that lander will acquire a tilting angle either about x axis or about z axis.

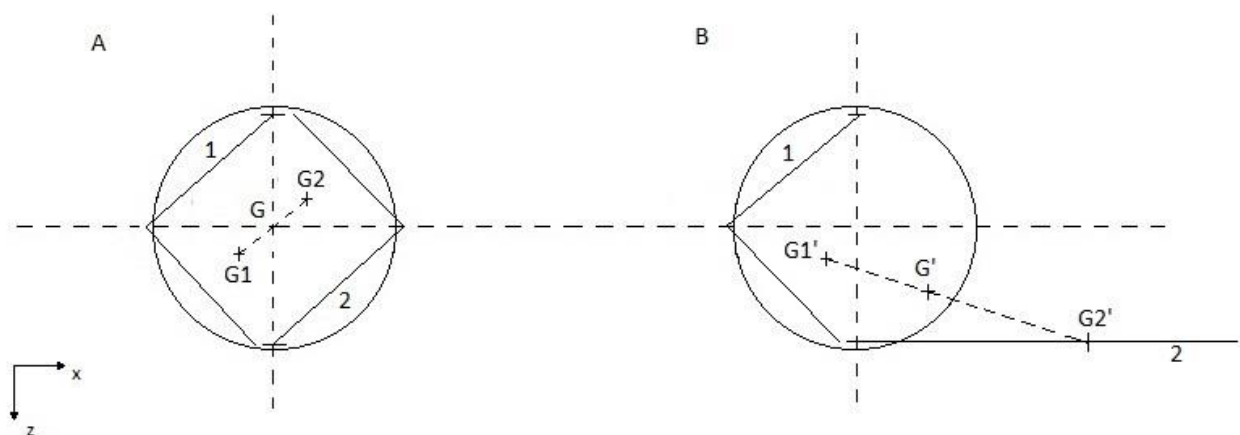


Fig. 73. Sketch of folded arms configuration (A) and total deployment of lower (B). Shoreline rocks in B are at the right of the sketch. Arms centers of mass are shown.

Before proceeding to give a first estimation of tilting angles, we determine barycentre position for two different arm's configurations. Fig. 74 shows sketch of arm 1 of Fig. 73, with schematic indication of mass distribution. For this analysis we considered masses concentrated at arm joints and connecting beams having no mass. For arm 1 folded configuration, considering $r = 0,5 m$ and $m = 4 kg$, barycentre (G) coordinates are $x = -0,125 m$ and $z = 0,125 m$, with respect to Fig. 74 x - z reference system.

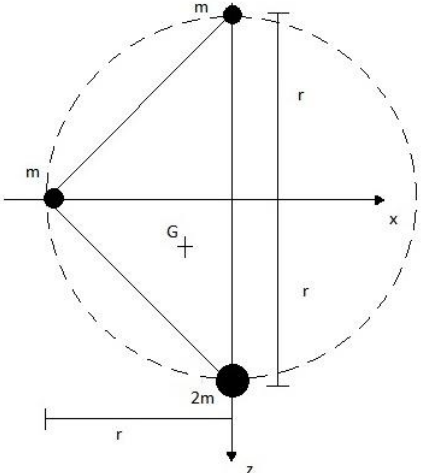


Fig. 74. Mass distribution and centre of massa position for folded arm configuration.

Fig. 75 shows arm 2 of Fig. 73 in deployed configuration. For $r = 0,5 m$ and $l = 0,75 m$, barycentre (G) coordinates results to be $x \cong 0,94 m$ and $z = 0,5 m$ with respect to Fig. 75 x - z reference system.

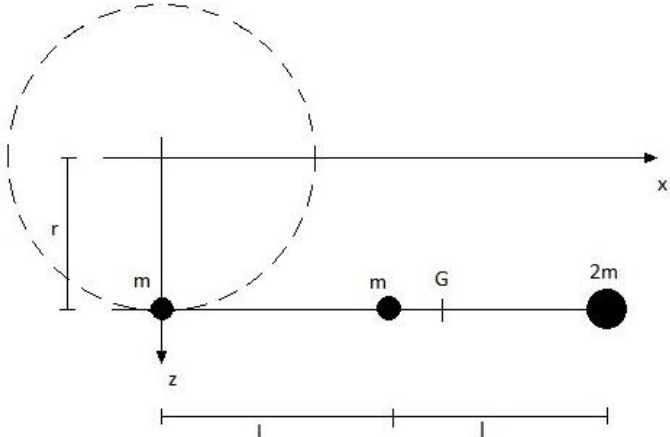


Fig. 75. . Mass distribution and centre of massa position for deployed arm configuration.

Now we are able to estimate overall arms' barycentric coordinates with reference to Fig. 73 configuration B (G'). That will result in $x = 0,4 m$ and $z \cong 0,31 m$.

We can now proceed with considerations and calculations about arms' barycentre displacement. It is appropriate to point out that arms' barycentre position can vary either in x - z plane or out of plane y -direction, former displacement changes lander tilting angle

while latter one varies metacentric height [3,5].

7.4.1 Horizontal displacement

As just said horizontal (x -direction) barycentre displacement varies lander tilting angle at which lander acquires a new stability position. We can determine such angle as [5]:

$$\beta = \tan^{-1} \left(\frac{2 \cdot x \cdot m_a}{MG \cdot m_{TOT}} \right)$$

Where:

- x , is robotic arms' barycentre displacement;
- m_a , is robotic arm mass;
- MG , is the distance between barycentre and metacentre (i.e. metacentric height);
- m_{TOT} , is the lander total mass, comprehensive of arms' mass.

We now consider initial robotic arms position to be folded position adopted for entry and descent phase towards lake surface and for cruise phase towards shoreline (Fig. 73, configuration A). Final position is the one sketched in configuration B of Fig. 73.

Thus, for, $x = 0,4 \text{ m}$, $m_a = 4 \text{ kg}$ and for MG and m_{TOT} defined in the previous part, we obtain,

$$\beta = 10 \text{ deg}$$

which results to be below maximum allowable tilting angle and then acceptable. Note also that β value is below boundary angle value which separates two approximations of metacentric theory, then constant metacentre position is an appropriate assumption.

We do not show calculations for tilting angle about x axis, since transversal (z -direction) barycentre displacement has been proved (see above) to be lower than barycentre displacement in x -direction, leading to a lower tilting angle.

7.4.2 Vertical displacement

As said before, robotic arms vertical displacement changes metacentric height (i.e. distance between metacentre and barycentre), we can determine new metacentric height as [5]:

$$MG' = \left(MB - \left(GB \pm \frac{2 \cdot m_a \cdot y}{m_{TOT}} \right) \right)$$

Where:

- MB , is the distance between metacentre and barycentre;

- GB , is the distance between barycentre and centre of buoyancy;
- m_a , is robotic arm mass;
- m_{TOT} , is the lander total mass, comprehensive arms' mass;
- y , is robotic arms barycentre vertical displacement.

The plus or minus sign in above formula stands for positive (+) negative (–) vertical displacement.

We now consider a hooking spot located at 1 m above liquid surface, we then have a robotic arms barycentre shifting of $x = 0,28\text{ m}$ and $y = 0,31\text{ m}$. Considering for m_a , m_{TOT} , MB and GB previously used values, that yields,

$$MG' = 0,19\text{ m}$$

As expected, metacentric height has decreased, leading to a less stable configuration.

We now have to verify that new metacentric height ensures equilibrium position at an angle below the critical tilting angle determined before. For $x = 0,28\text{ m}$, calculation yields,

$$\beta = 8\text{ deg}$$

That results to be below critical tilting angle value, so proper equilibrium is ensured also for transversal hooking case.

7.4.3 Further comments

Clearly, in above case, being lander tilted of about $\beta = 8\text{ deg}$, reachable hooking spot will not be at 1 m height as considered for calculations, but at the end of arm deployment reachable hooking spot will result to be lower. Anyway, our aim was to prove that lander can perform transversal hooking without incurring in capsizing.

What just said stays for horizontal case too, so for actual horizontal hooking will be necessary to impose a certain elevation angle to be sure that robotic arm tip will not get in contact with liquid methane surface, as would be if elevation angle was not imposed. As it has just been proved, also high elevation angle will not cause lander capsizing.

One can observe that for both horizontal and transversal hooking, connection is obtained in tilted position, but once connection between lander and shoreline rocks has been obtained, new equilibrium position is ensured. In new equilibrium position, lander body does not have to ensure anymore equilibrium to lander-arms system by itself, but it is helped from rocks support reaction, thus once lander will be connected to shoreline tilting will be reduced with respect to before-hooking configuration. Furthermore, one can think of other arm utilization in order to counteract arms barycentre displacement.

7.5 Conclusions

In this chapter we showed how stability of the lander is ensured either for external perturbations (i.e. waves) or for robotic arms deployment. Clearly this has been done under certain assumptions, i.e. constant metacentric height with varying tilting angle, global barycentric position placed at half total lander height, rough estimation of overall system mass and individually arm deployment. In subsequent mission and design phase, some of assumptions could not stand anymore, but for preliminary design that can be considered reasonable result.

References

- [1] LEMENTS, NITU. ESA Contribution to the Titan Saturn System Mission. 2009.
- [2] LORENZ, Ralph D.; NEWMAN, Claire; LUNINE, Jonathan I. Threshold of wave generation on Titan's lakes and seas: Effect of viscosity and implications for Cassini observations. *Icarus*, 2010, 207.2: 932-937.
- [3] RAPACCIUOLO, F. Elementi di teoria della nave. *Moderna edizioni*, 2012.
- [4] D'AGOSTINO, L. Liquid Propellant Rockets 1. *Lecture notes*, 2014.
- [5] <http://www.webalice.it/markmele/spostamento%20dei%20pesi%20prof%20MARCO%20MELE.pdf>. Last access on November 2015.

8 Launch configuration

8.1 Arms folded configurations

For launch phase lander is placed inside thermal shield which will be released during descent phase towards Titan surface. Since thermal shield has already been sized [1] robotic arms folded dimension have to remain in a well-defined volume. Besides, arms folded position has to consider instrumentation mounted on lander the top surface. Proposed folded configuration is shown in Fig. 76 to 78. Clearly, because of arm geometry, locking system along arm length has been added in order to ensure proper arms stabilization. Arm locking system will be opened when lander is close to shoreline and arms need to operate with means of pyrotechnical charges.

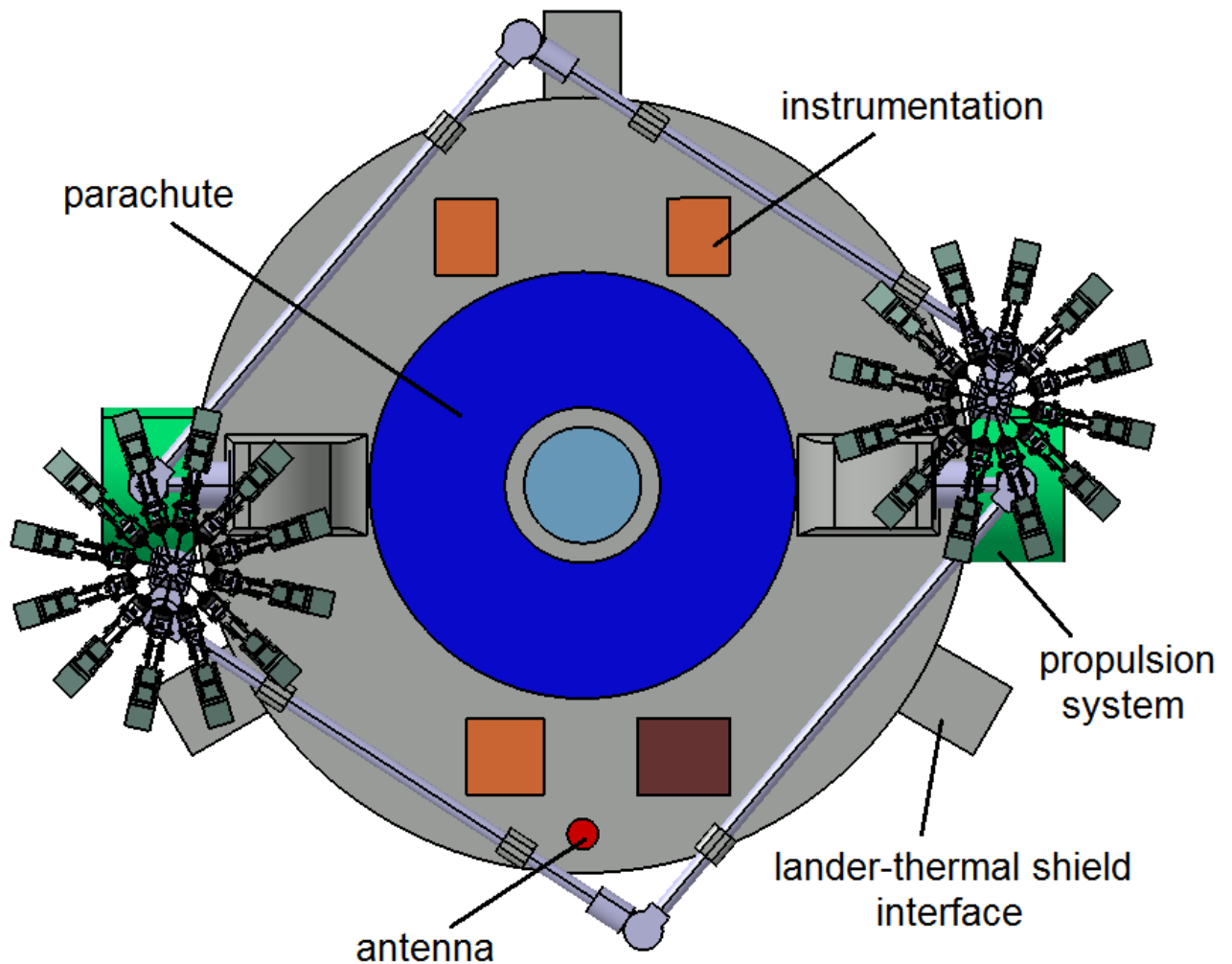


Fig. 76. Lander launch configuration. Top view

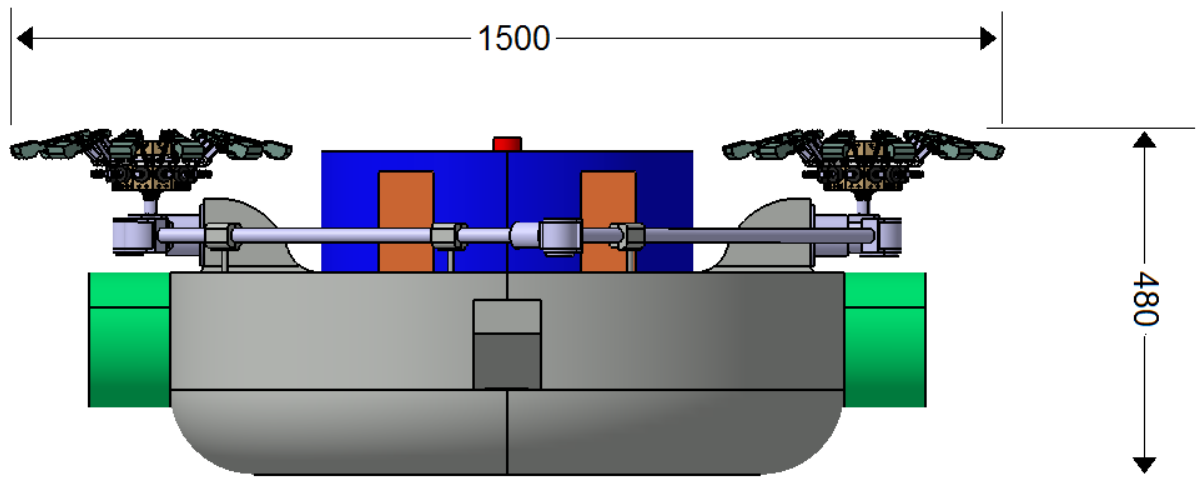


Fig. 77. Lander launch configuration. Lateral view.

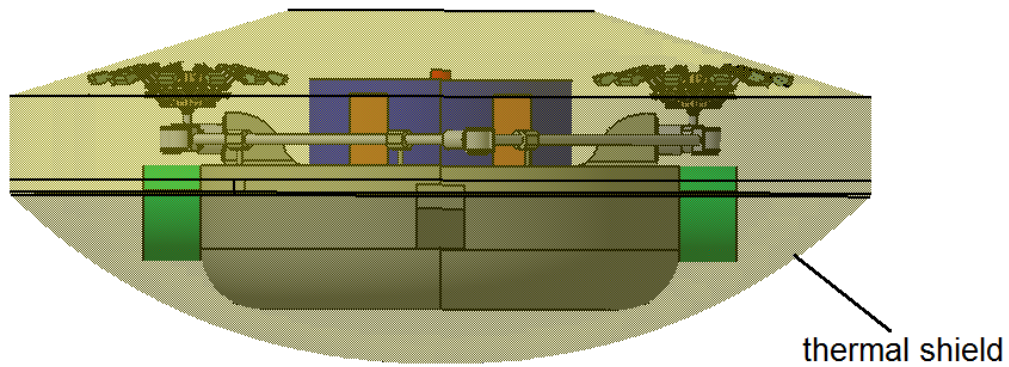


Fig. 78. Thermal shield interior accommodation. Lateral view.

Table 32 summarizes joint angles for arms folded configuration. For joint angles definition see Section 4.

θ_1	180°
θ_2	40°
θ_3	-7°
θ_4	-90°
θ_5	70°
θ_6	90°

Table 32. Joints angle for arms folded configuration.

8.2 Vibration preliminary analysis

In this section we will treat toe-dodecagon spring connection under vibrational point of view (see Section 5 for connection details). That represents a first approximation of the actual problem, but it can be taken as guide line for future development. We will treat the problem with reference to Fig. 79, where straight beam at which mass and spring are connected represents toe. For this problem we take $k = 75$, $m = 10 \text{ g}$, $r_1 = 1,5 \text{ cm}$ and $L = 11 \text{ cm}$. Stiffness constant of the spring has been selected from kinematics consideration and represents a compromise between desirable spring stiffness and actuation easiness of toe mechanism. The more the spring stiffness, the more torque is required by servo motor to overcome initial tension (see Section 5 for visual help).

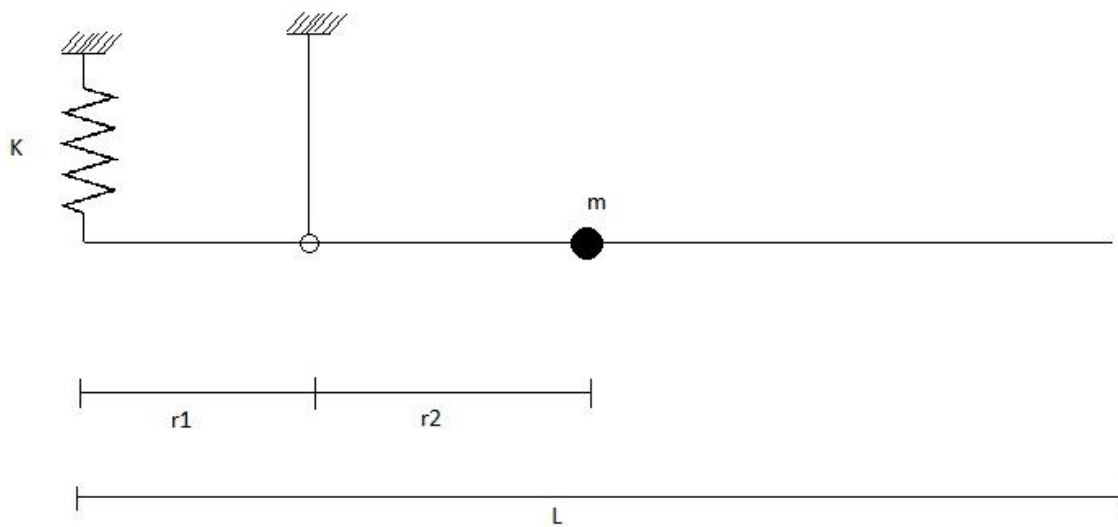


Fig. 79. Schematic representation of spring-toe connection.

We consider toe mass concentrated in its barycentre, taken as half of toe total length. That yields $r_2 = 3,5 \text{ cm}$. From geometric consideration we can write a slightly modified classic harmonic equation,

$$m\ddot{x} + k \frac{r_1}{r_2} x = 0$$

We can then determine system natural frequency as,

$$f_n = \frac{1}{2\pi} \sqrt{\frac{kr_1}{mr_2}}$$

And substitution of known values yields $f_n = 9 \text{ Hz}$.

Natural frequency of spring-toe system is quite low and then probably interact with launch system lower natural frequency [2], that is clearly unacceptable for resonance consideration.

We then present one possible locking solutions which must prevent toes from vibrating at derived natural frequency during launch. Fig. 80 and 81 shows proposed locking system, based on interference coupling between microspines toe and metal support. Ring support shown in figure is mounted at launch and deployed when necessary for toe to assume working position. Ring disengagement is obtained with means of pyrotechnical charges located where shown in figure. Ring disengagement has been thought to happen when hand gripper is turn upside down with respect to Fig. 76/77 configuration, in order to minimize risk of ring particles fall on hand mechanism.

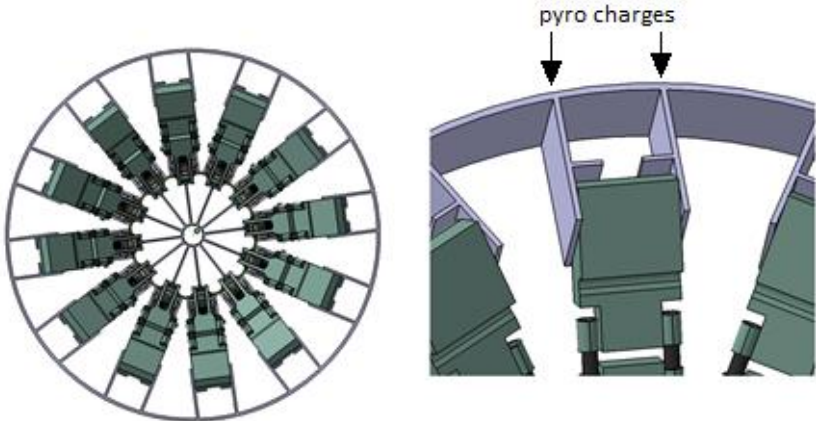


Fig. 80. Locking ring. Top view and detail.

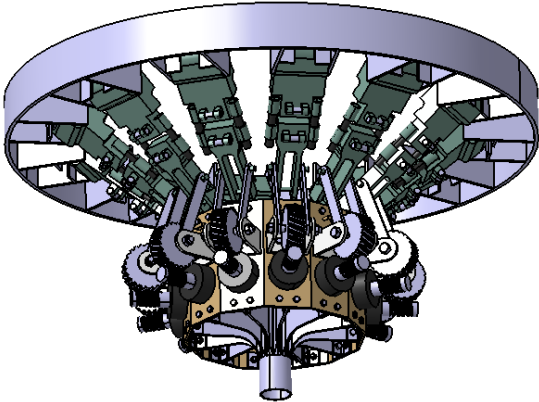


Fig. 81. Locking ring. Global view.

Of course, considering toes folded position shown in Fig. 76 to 78, changes arms launch configuration and in particular hand configuration. It has not been presented here since toes locking system is just a proposal and no information about reliability can be obtained without a more detailed study. Few words about toes locking system possible future development has been spent in Section 10.

References

[1] LEMENTS, NITU. ESA Contribution to the Titan Saturn System Mission. 2009.
 [2] SARAFIN, Thomas P.; LARSON, Wiley J. Spacecraft structures and mechanisms: from concept to launch. 1995.

9 Microspine technology review

9.1 State of the art

Microspines technology has been first developed from Stanford university [1] and then used either to perform robots climbing of vertical irregular surfaces [4] or to ensure stabilization for drilling system [1]. At first, microspines technology was used to prove possibility of climbing rough and irregular surface, as wall of different materials or trees [4,5]. All of these climbing configurations involves unidirectional motion, since these light weight robots are only capable of vertical motion and cannot reacts to multidirectional loads. In the following years Jet Propulsion Lab scientists thought about different grippers configuration in order to achieve omnidirectional stabilization [1,3]. JPL mounted this microspines technology grippers on LEMUR class robot [1] to make possible climbing on irregular surface not only in vertical configuration, but also adhering to wall of negative inclination [1,3] as well as perform drilling operation in micro gravity environments. LEMUR robots are light weight robots capable of high level of operational flexibility [2]. First moving robot mounting omnidirectional microspines technology was LEMURIIB in a particular configuration which involves capability either of climbing or drilling in order to collect samples and to be capable of overcoming mobility issues own by wheel based lander. Fig. 82 shows LEMURIIB in one-arm climbing configuration. Microspines technology has been selected for space application from JPL since it resulted to be a quite mature technology [3] and because of need of sampling and mobility operations in microgravity environment [3], e.g. asteroids.

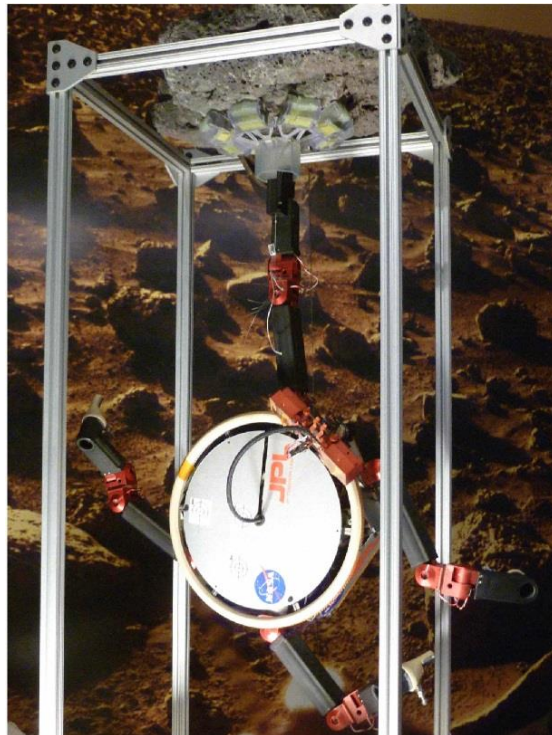


Fig. 82. JPL LemurIIB hanging vertically on rocky surface using microspine gripper [3].

9.2 Possible future employment for space application

In this thesis work we proposed an omnidirectional gripper configuration, based on JPL gripper geometry, using other actuator devices and toes configuration, more suited for our problem. We also clearly increased number of microspines per foot with respect to JPL configuration, in order to ensure proper loads support. In particular we showed how it is possible to obtain floating lander stabilization using microspines technology, making surface adhesion and then allowing sampling operation close to shoreline.

This technology can be clearly exploited in other ways. As shown by JPL [1,3] one of the most promising use for microspine technology is represented by capability of climbing on irregular surface reaching spots where wheel drive lander cannot access. While going around an obstacle, such as a highland or a pit, as done by wheel drive landers, microspine technology can allow to overcome such an obstacle, opening wide opportunities for terrain exploration. At this purpose, would be interesting to implement a new class of lander robot, capable either of wheel driving or climbing/walking. This can exploit benefits from both technologies, using wheel drive propulsion when possible, allowing faster displacements and switching to climbing/walking mechanism when necessary, e.g. rough terrain.

This flexible configuration could be obtained essentially with two different lander architectures. First one involves one lander alone, capable of switching from one motion system to the other, with folding/unfolding mechanism to select proper motion system in response to different terrains. Other conceptual architecture can exploit existing multi-robotic architecture shown in Fig. 83 [7]. As shown in Fig. 83 one can think about a wheel drive rover carrying a smaller and lighter climbing/walking robot that can be deployed when necessary. In this case smaller robot would be equipped with microspine grippers in order to reach different spots with respect to main rover. Furthermore, different robot sizes allows different mission objectives, larger robot can move faster and analyse sample or making measurements during its way, while smaller robots can reach narrow spots, as small caves or pits, as well as climbing over obstacles.

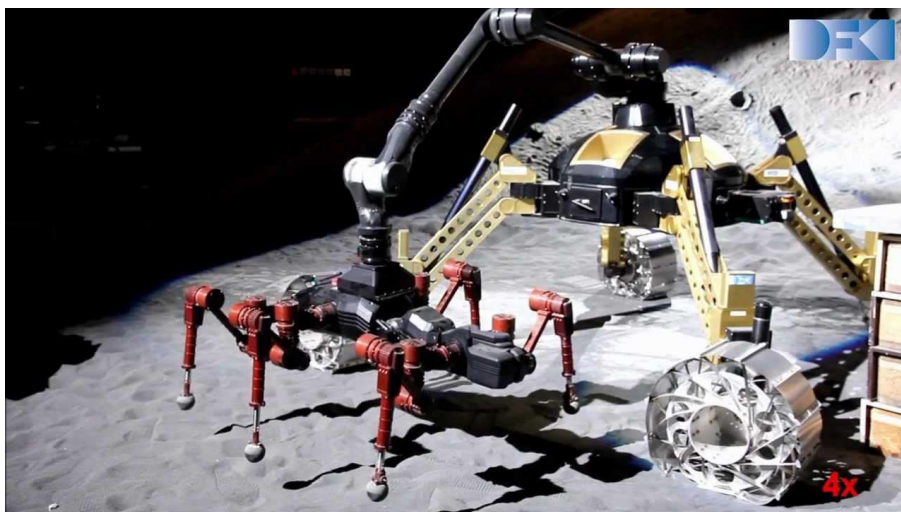


Fig. 83. RIMRES-system. Wheeled-leg yellow rover SHERPA and legged red robot CREX [7].

At last, we consider possible future employment of microspine grippers to hang to certain surface and remain there during mission development. As considered by JPL [3] microspine grippers can be useful in microgravity environments, where parking and drilling operation are quite difficult to be performed. An example of this difficulty can be represented by Rosetta mission, in which harpoon anchoring mechanism of Philae lander failed to fire and the lander probe bounced off the comet surface, before fell again on it [6]. It would be thought, just as an hypothetical scenario, that using microspine grippers would have made safer landing operation. Furthermore, once stabilization would have been acquired with microspine grippers, additional fastening operation could have been made with drilling system integrated in microspine grippers, as shown in Fig. 84 [1]. Of course in this hypothetical comparison it must be pointed out the much higher complexity of microspine gripper with respect to harpoon system.

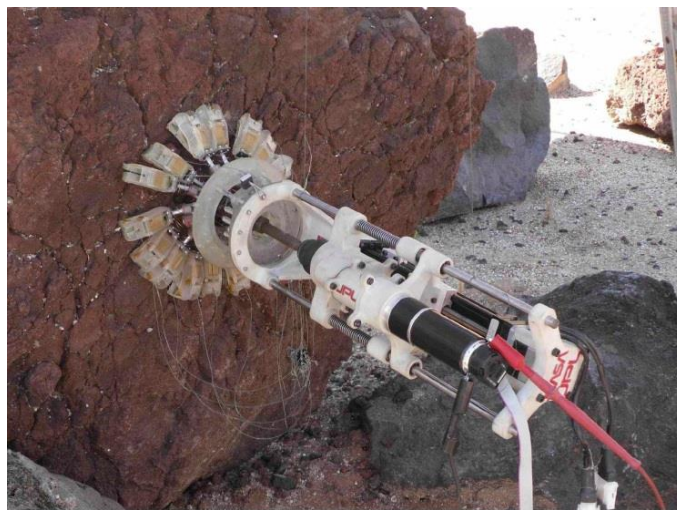


Fig. 84. Microspine gripper with integrated drilling system [1].

References

- [1] PARNES, Aaron, et al. Gravity-independent mobility and drilling on natural rock using microspines. In: *Robotics and Automation (ICRA), 2012 IEEE International Conference on*. IEEE, 2012. p. 3437-3442.
- [2] <https://www-robotics.jpl.nasa.gov/systems/system.cfm?System=5>. Last access on November 2015.
- [3] PARNES, Aaron. Anchoring foot mechanisms for sampling and mobility in microgravity. In: *Robotics and Automation (ICRA), 2011 IEEE International Conference on*. IEEE, 2011. p. 6596-6599.
- [4] ASBECK, Alan T., et al. Scaling hard vertical surfaces with compliant microspine arrays. *The International Journal of Robotics Research*, 2006, 25.12: 1165-1179.
- [5] SAUNDERS, Aaron, et al. The rise climbing robot: body and leg design. In: *Defense and Security Symposium*. International Society for Optics and Photonics, 2006. p. 623017-623017-13.
- [6] <http://txchnologist.com/post/102624788755/philae-harpoon-failure-suspect-propellant-that>. Last access on November 2015.
- [7] CORDES, Florian, et al. RIMRES: A modular reconfigurable heterogeneous multi-robot exploration system. In: *International Symposium on Artificial Intelligence, Robotics and Automation in Space (i-SAIRAS 2012), Turin. ESA. 2012*.

10 General conclusions

10.1 Work summary

In present thesis work an hooking system for floating lander stabilization has been proposed. We considered previously presented lander configuration [1] as a starting point from which we developed hooking system. Lander must be capable of perform hooking manoeuvre and then maintain hooking configuration during shoreline sampling acquisition duration. External perturbation, i.e. waves, must be taken into account for hooking system preliminary design. After trade off analysis has been made between two different hooking possibilities we end up choosing robotic arm configuration to reach shoreline rocks and ensure lander stability. Other hoking system, i.e. harpoon, has been discarded because of energy dissipation consideration. After analyze through numerical simulation waves imposed displacement problem, we chose arm section and length. Afterwards, we focused on hooking mechanism choice. As done for hooking system trade off analysis between two possible hooking mechanisms has been carried on. Microspines technology [2,3] has then been selected for hooking mechanism. A robotic hand gripper has been developed on previous similar works base [3] and microspines toe actuation mechanism has then been analyzed and discussed, giving preliminary guidelines for sizing. Besides, fatigue has been considered for some critical components. Later on, preliminary center of mass analysis has been carried out, making considerations about robotic arms deployment architecture. Finally, similar robotic systems have been revised and possible microspines technology employment has been analyzed.

10.2 Future improvement

During thesis work development, some critical issues have been sampled out as of major interest for future improvement. Of course there can be identified lots of aspects to be refined, but we just limit our treatment to three of them that we judged of major interest.

Model refinement

As said in Section 3 our model represents a first approximation of actual physical problem. Model can be improved taking into account waves reflected from shoreline and their interaction with lander body. Furthermore, a dynamic model would be appropriate to be developed in order to validate static model results.

Toes degrees of freedom

One of the issue of future interest is represented by additional toe degrees of freedom. Previous works [2] showed that adding rotational DOF along toes major length axis improves adaptability on irregular surfaces and then can guarantee a better microspines efficiency. It could be studied in detail for presented problem, how additional toe degrees of freedom influence surface

adaptability and microspines efficiency.

Worm drive connection

As explained in Section 5 single actuation mechanism for each toe has been chosen because of toes independency need for hooking problem nature. We selected worm drive connection in order to rotate axis of motion by 90 degrees. It can be study if selected mechanism results to be best choice for actuation mechanism and if so, a more precise sizing should be carried out.

Toes locking configuration

In Section 5 preliminary toe locking system for launch configuration has been proposed. It is important to note that lander was not design to allocate robotic arms structure and then passive and extremely simple locking mechanism had to be considered. Thinking of dedicated lander designed to accommodate arms components, one can develop a more suitable and reliable toes locking mechanism.

References

- [1] LEMENTS, NITU. ESA Contribution to the Titan Saturn System Mission. 2009.
- [2] PARNES, Aaron. Anchoring foot mechanisms for sampling and mobility in microgravity. In: *Robotics and Automation (ICRA), 2011 IEEE International Conference on*. IEEE, 2011. p. 6596-6599.
- [3] ASBECK, Alan T., et al. Scaling hard vertical surfaces with compliant microspine arrays. *The International Journal of Robotics Research*, 2006, 25.12: 1165-1179.